The Astronomical Journal, 123:3067–3107, 2002 June

AN *INFRARED SPACE OBSERVATORY* ATLAS OF BRIGHT SPIRAL GALAXIES[1]

George J. Bendo,[2,3,4] Robert D. Joseph,[2,3] Martyn Wells,[5] Pascal Gallais,[6] Martin Haas,[7] Ana M. Heras,[8,9] Ulrich Klaas,[7] René J. Laureijs,[8,9] Kieron Leech,[9,10] Dietrich Lemke,[7] Leo Metcalfe,[9] Michael Rowan-Robinson,[11] Bernhard Schulz,[9,12] and Charles Telesco[13]

Received 2002 January 28; accepted 2002 February 7

ABSTRACT

In this first paper in a series we present an atlas of infrared images and photometry from 1.2 to 180 μm for a sample of bright spiral galaxies. The atlas galaxies are an optically selected, magnitude-limited sample of 77 spiral and S0 galaxies chosen from the Revised Shapley-Ames Catalog (RSA). The sample is a representative sample of spiral galaxies and includes Seyfert galaxies, LINERs, interacting galaxies, and peculiar galaxies. Using the *Infrared Space Observatory* (*ISO*), we have obtained 12 μm images and photometry at 60, 100, and 180 μm for the galaxies. In addition to its imaging capabilities, *ISO* provides substantially better angular resolution than is available in the *IRAS* survey, and this permits discrimination between infrared activity in the *central* regions and global infrared emission in the disks of these galaxies. These *ISO* data have been supplemented with *JHK* imaging using ground-based telescopes. The atlas includes 2 and 12 μm images. Following an analysis of the properties of the galaxies, we have compared the mid-infrared and far-infrared *ISO* photometry with *IRAS* photometry. The systematic differences we find between the *IRAS* Faint Source Catalog and *ISO* measurements are directly related to the spatial extent of the *ISO* fluxes, and we discuss the reliability of *IRAS* Faint Source Catalog total flux densities and flux ratios for nearby galaxies. In our analysis of the 12 μm morphological features we find that most but not all galaxies have bright nuclear emission. We find 12 μm structures such as rings, spiral arm fragments, knotted spiral arms, and bright sources in the disks that are sometimes brighter than the nuclei at mid-infrared wavelengths. These features, which are presumably associated with extranuclear star formation, are common in the disks of Sb and later galaxies but are relatively unimportant in S0–Sab galaxies.

Key words: atlases — galaxies: photometry — galaxies: spiral — infrared: galaxies — surveys

1. INTRODUCTION

One of the major results from the advent of infrared astronomy is the discovery that the central regions of many spiral galaxies emit a dominant fraction of their bolometric luminosities in the infrared. The underlying energy source for this "infrared activity" in most cases is inferred to be a recent burst of star formation, with the luminosity of the massive, young stars absorbed by dust and reradiated in the infrared. Although it is now widely recognized that interactions between galaxies often play a role in triggering such infrared activity (Joseph et al. 1984), after more than two decades we still have quite incomplete understanding of the phenomenology of infrared activity in galaxies. It is not clear how such activity is triggered in noninteracting galaxies, whether it is always triggered by interactions, what the ranges of frequency and luminosity are for infrared activity in an unbiased sample of spirals, or how such activity varies along the Hubble sequence. As a result, we have no baseline understanding of infrared activity in "normal" spiral galaxies against which to compare to pathological classes such as ultraluminous infrared galaxies or galaxies at higher redshifts.

Therefore, it seems quite important to carry out a large study of an unbiased sample of spirals to see if some definitive answers to these questions can be found. This survey is necessary for determining the ranges of star formation and infrared activity, the characteristics of star formation, and the mechanisms that trigger star formation in normal spiral galaxies. We have carried out such a survey using the unprecedented angular resolution, sensitivity, and imaging capability offered by the *Infrared Space Observatory* (*ISO*) (Kessler et al. 1996).

Early ground-based surveys of unbiased samples of bright spiral galaxies at 10 μm were undertaken by Rieke & Lebofsky (1978) and Scoville et al. (1983). A shortcoming of

[1] Based on observations with the *Infrared Space Observatory* (*ISO*), an ESA project with instruments funded by ESA Member States (especially the PI countries: France, Germany, Netherlands, and United Kingdom) and with the participation of ISAS and NASA.

[2] University of Hawaii, Institute for Astronomy, 2680 Woodlawn Drive, Honolulu, HI 96822; bendo@ifa.hawaii.edu, joseph@ifa.hawaii.edu.

[3] Visiting Astronomer at the Infrared Telescope Facility, which is operated by the University of Hawaii under contract from the National Aeronautics and Space Administration.

[4] Visiting Astronomer at the UH 2.2 m Telescope at Mauna Kea Observatory, Institute for Astronomy, University of Hawaii.

[5] UK Astronomy Technology Center, Royal Observatory Edinburgh, Blackford Hill, Edinburgh EH9 3HJ, Scotland, UK; mw@roe.ac.uk.

[6] CEA/DSM/DAPNIA Service d'Astrophysique, F-91191 Gif-sur-Yvette, France; gallais@discovery.saclay.cea.fr.

[7] Max-Planck-Institut für Astronomie, Königstuhl 17, D-69117 Heidelberg, Germany; haas@mpia-hd.mpg.de, klaas@mpia-hd.mpg.de, lemke@mpia.mpg.de.

[8] Astrophysics Division, Space Science Department of ESA, ESTEC, P.O. Box 299, 2200 AG Noordwijk, Netherlands; aheras@estsa2.estec.esa.nl, rlaureij@iso.vilspa.esa.es.

[9] *ISO* Data Center, Astrophysics Division, ESA, Villafranca del Castillo, 28080 Madrid, Spain; lmetcalf@iso.vilspa.esa.es.

[10] Said Business School, Park End Street, Oxford OX1 1HP, England, UK; kieron.leech@said-business-school.oxford.ac.uk.

[11] Astrophysics Group, Imperial College, Blackett Laboratory, Prince Consort Road, London SW7 2BZ, England, UK; m.rrobinson@ic.ac.uk.

[12] Infrared Processing and Analysis Center, California Institute of Technology, MS 100-22, 770 South Wilson Avenue, Pasadena, CA 91125; bschulz@ipac.caltech.edu.

[13] Department of Astronomy, University of Florida, P.O. Box 112055, Gainesville, Florida 32611; telesco@astro.ufl.edu.

both of these surveys was that only a minor fraction of the sample was actually detected, as a result of the limited sensitivity of ground-based photometry in the thermal infrared.

The advent of the *IRAS* survey, with its detections of many thousands of infrared bright galaxies, provided material for further investigations of infrared activity in galaxies. Most of the ensuing studies of galaxy samples are based on infrared-selected samples, most commonly the *IRAS* 60 μm flux density. However, de Jong et al. (1984) chose an optically selected sample of galaxies from the Revised Shapley-Ames Catalog (RSA) and investigated the *IRAS* photometric properties. Rice et al. (1988) published a catalog of images of 85 large galaxies with blue isophotal diameters greater than 8′, with the images reconstructed from the *IRAS* scans.

ISO has the potential to provide a new perspective on infrared activity in the centers of spiral galaxies. The sky survey mission of *IRAS*, and the infrared detector technology of that era, required scanning with rather large apertures, while *ISO* was able to point and integrate using detector arrays with much smaller pixels. For example, at 12 μm, the *ISO* mid-infrared camera, ISOCAM, provided a scale of 3″ pixel^{-1}. At 60 and 100 μm, the *ISO* photometer, ISOPHOT, offered 45″ pixels over a 135″ field. This provides more sensitivity and better ability to distinguish unambiguously between nuclear emission and emission from the disks of spiral galaxies. *ISO* also offers an extended wavelength range beyond the 100 μm *IRAS* limit. Since the spectral energy distributions (SEDs) of galaxies in the *IRAS* data are generally still rising at 100 μm, the 180 μm photometry provided by *ISO* permits much better determination of the SEDs and color temperatures of spiral galaxies in the far-infrared.

Related mid-infrared surveys of spiral galaxies based on *ISO* observations include Dale et al. (2000) and Roussel et al. (2001). Both of these surveys had rather different scientific objectives and therefore employed galaxy samples that are neither unbiased, complete, nor magnitude limited, nor do they include *ISO* measurements at wavelengths longer than $\sim$15 μm.

This paper is the first of three papers dealing with this sample. It includes a thorough discussion of the sample, the observations, the data processing, a comparison of the data to *IRAS* data, and a discussion of the images and the spatial distribution of the infrared flux. The second paper will discuss star formation along the Hubble sequence, using the mid- and far-infrared fluxes normalized by the *K*-band fluxes as star formation indicators. The third paper will discuss dust temperatures as determined from the far-infrared data in this paper and additional submillimeter data.

2. THE SAMPLE

2.1. *Selection Criteria*

The galaxies observed in this study are an optically selected complete sample selected from the RSA, which contains 1246 galaxies and is complete to $B \sim 13$ (Sandage & Tammann 1987). Galaxies designated as members of the Virgo Cluster in Binggeli, Sandage, & Tammann (1985) were excluded. (Virgo Cluster galaxies were observed in a separate *ISO* program by Tuffs et al. 2002.) A list of the remaining spirals, including S0, with apparent blue magnitudes $B_T \leq 12$ was made, and then from these 323 spirals, two lists of galaxies observable at either an autumn or spring launch were identified and submitted to *ISO* Mission Planning. In the event 77 galaxies were observed before the guaranteed time in the *ISO* Central Programme for this project was exhausted. The 77 galaxies observed are representative of the total sample, as discussed below.

2.2. *Sample List*

Table 1 lists all of the galaxies in the atlas as well as additional information on galaxy morphology and activity. When classifying galaxies for morphological studies, we used the Third Reference Catalogue of Bright Galaxies (RC3; de Vaucouleurs et al. 1991). The RC3 relies purely on morphological characteristics, such as the bulge/disk ratio and the tightness of the spiral arms, to classify galaxies. The symbols used in the header for Table 1 are defined in RC3. For comparison, however, we are also including morphological information as well as apparent magnitudes from RSA.

We also present in Table 2 arm class information from Elmegreen & Elmegreen (1987), nuclear activity from Ho, Filippenko, & Sargent (1997), distances from the Nearby Galaxies Catalog (Tully 1988), and other notes on the galaxies' morphology, nuclear activity, and environment. (Note that the nuclear activity classifications are based strictly on optical line ratios.) Since this is a representative sample of spiral galaxies, the sample contains a number of Seyfert galaxies, LINERs, starburst galaxies, a few interacting galaxies, and a few galaxies that are otherwise classified as peculiar. This is not meant to be a sample of normal spiral galaxies but a representative sample of spiral galaxies that includes active and disturbed objects.

We present the range of morphological features in our sample in Table 3. In addition, we also show the distribution of Hubble types and distances in Figures 1, 2, and 3. These tables and figures show that we do have some minor biases in our sample.

Table 3 and Figure 1 show that, according to RC3 classifications, over half of the galaxies in our sample are Sbc–Scd, one-third of the galaxies are Sb or earlier, and 1/10 of the galaxies are later than Sd. This trend is actually similar to the trends in Hubble types for all galaxies in the RSA. Figure 2 shows a comparison of the Hubble types of galaxies in the sample to all galaxies in RSA using RSA classifications. The figure shows that the sample does have a slightly larger number of Sc galaxies relative to S0 and Sa galaxies than would be expected for all galaxies in RSA. The numbers of strongly barred, weakly barred, and unbarred galaxies in Table 3 demonstrate that the *ISO* atlas does have representative numbers of each type.

Except for a spike between 5 and 10 Mpc and a slight dip between 10 and 15 Mpc, the atlas galaxies have a smooth distribution of distances up to 30 Mpc as shown in Figure 3. The 5–10 Mpc spike represents eight galaxies from the same group in the Coma-Sculptor cloud (see Tully 1988). The dip seems to be simply a statistical fluctuation. These biases in distances should not affect our study of infrared activity or star formation activity in these galaxies, although it may present difficulty when generating a luminosity function from these data.

TABLE 1

RC3 AND RSA DATA FOR ATLAS GALAXIES

	RC3 DATA						RSA DATA		
GALAXY	Morphological Type	T[a]	Luminosity Class[b]	log D_{25}[c]	log R_{25}[d]	B_T[e]	Morphological Type	B_T[f]	$B_T^{0,i}$[g]
NGC 55	SB(s)m	9	5.6	2.51	0.76	8.42	Sc	8.22	7.35
NGC 289	SB(rs)bc	4	2.2	1.71	0.15	11.72	SBbc(rs)I–II	11.81	11.41
NGC 1512.....	SB(r)a	1	1.1	1.95	0.20	11.13	SBb(rs)I pec	11.38	10.77
NGC 1569.....	IBm	10	7.5	1.56	0.31	11.86	SmIV	11.90	11.08
NGC 3359.....	SB(rs)c	5	3	1.86	0.22	11.03	SBc(s)I.8 pec	10.99	10.49
NGC 3556.....	SB(s)cd	6	5.7	1.94	0.59	10.69	Sc(s)III	10.71	9.97
NGC 3898.....	SA(s)ab	2	1.9	1.64	0.23	11.6	SaI	11.7	10.96
NGC 4062.....	SA(s)c	5	4.2	1.61	0.37	11.9	Sc(s)II–III	12.0	11.43
NGC 4088.....	SAB(rs)bc	4	3.9	1.76	0.41	11.15	Sc(s)II–III/SBc	11.14	10.54
NGC 4096.....	SAB(rs)c	5	4.2	1.82	0.57	11.48	Sc(s)II–III	11.02	10.30
NGC 4100.....	PSA(rs)bc	4	2.2	1.73	0.48	11.89	Sc(s)I–II	11.62	10.96
NGC 4136.....	SAB(r)c	5	3.4	1.60	0.03	(11.6)	Sc(r)I–II	11.58	11.28
NGC 4157.....	SAB(s)b	3	3	1.83	0.70	12.15	Sbc	11.56	10.73
NGC 4203.....	SAB0	−3	...	1.53	0.03	11.8	$S0_2(1)$	11.62	11.62
NGC 4236.....	SB(s)dm	8	7.6	2.34	0.48	10.05	SBdIV	10.06	9.35
NGC 4244.....	SA(s)cd	6	7	2.22	0.94	10.88	Scd	10.60	9.73
NGC 4274.....	RSB(r)ab	2	4	1.83	0.43	11.34	Sa(s)	11.30	10.35
NGC 4314.....	SB(rs)a	1	...	1.62	0.05	11.43	SBa(rs) pec	11.35	11.35
NGC 4395.....	SA(s)m	9	7.3	2.12	0.08	10.64	SdIII–IV	10.69	10.35
NGC 4414.....	SA(rs)c	5	3.7	1.56	0.25	10.96	Sc(sr)II.2	10.95	10.48
NGC 4448.....	SB(r)ab	2	3	1.59	0.44	12	Sb(r)I–II	12.0	11.05
NGC 4559.....	SAB(rs)cd	6	4.3	2.03	0.39	10.46	Sc(s)II–III	10.36	9.79
NGC 4605.....	SB(s)c pec	5	5.7	1.76	0.42	10.89	Sc(s)III	10.96	10.35
NGC 4618.....	SB(rs)m	9	3.9	1.62	0.09	11.22	SBbc(rs)II.2 pec	11.20	10.87
NGC 4631.....	SB(s)d	7	5	2.19	0.76	9.75	Sc on edge	9.84	8.98
NGC 4710.....	SA(r)0	−1	...	1.69	0.62	11.91	$S0_3(9)$	11.85	11.85
NGC 4725.....	SAB(r)ab pec	2	2.4	2.03	0.15	10.11	Sb/SBb(r)II	9.99	9.37
NGC 4826.....	RSA(rs)ab	2	3.5	2.00	0.27	9.36	Sab(s)II	9.37	8.62
NGC 4945.....	SB(s)cd	6	6.7	2.30	0.72	9.3	Sc	9.60	8.30
NGC 4976.....	E4 pec	−5	...	1.75	0.28	11.04	$S0_1(4)$	11.17	10.13
NGC 4984.....	RSAB(rs)0	−1	...	1.44	0.10	12.25	Sa(s)	11.71	11.10
NGC 5005.....	SAB(rs)bc	4	3.3	1.76	0.32	10.61	Sb(s)II	10.64	9.81
NGC 5033.....	SA(s)c	5	2.2	2.03	0.33	10.75	Sbc(s)I–II	10.63	10.11
NGC 5054.....	SA(s)bc	4	2.3	1.71	0.24	11.67	Sb(s)I–II	11.51	10.75
NGC 5055.....	SA(rs)bc	4	3.9	2.10	0.24	9.31	Sbc(s)II–III	9.33	8.87
NGC 5068.....	SAB(rs)cd	6	4.7	1.86	0.06	10.7	SBc(s)II–III	10.53	10.15
NGC 5087.....	SA0	−3	...	1.37	0.14	12.4	$S0_3(5)$	12.0	11.93
NGC 5101.....	RSB(rs)0/a	0	...	1.73	0.07	11.63	SBa	11.58	11.48
NGC 5102.....	SA0	−3	...	1.94	0.49	10.35	$S0_1(5)$	10.64	10.47
NGC 5112.....	SB(rs)cd	6	3.3	1.60	0.15	12.6	Sc(rs)II	11.82	11.43
NGC 5161.....	SA(s)c	5	2.3	1.75	0.41	12	Sc(s)I	11.98	11.24
NGC 5170.....	SA(s)c	5	1.1	1.92	0.91	12.06	Sb:	11.88	10.49
NGC 5204.....	SA(s)m	9	7.6	1.70	0.22	11.73	SdIV	11.75	11.29
NGC 5236.....	SAB(s)c	5	2.8	2.11	0.05	8.2	SBc(s)II	8.51	8.08
NGC 5247.....	SA(s)bc	4	1.8	1.75	0.06	10.5	Sc(s)I–II	11.1	10.71
NGC 5300.....	SAB(r)c	5	3.3	1.59	0.18	(11.8)	Sc(s)II	11.93	11.51
NGC 5334.....	SB(rs)c	5	5.1	1.62	0.14	(11.6)	SB:	11.90	11.42
NGC 5364.....	SA(rs)bc pec	4	1.1	1.83	0.19	11.17	Sc(r)I	11.05	10.64
NGC 5371.....	SAB(rs)bc	4	1.2	1.64	0.10	11.32	Sb(rs)I/SBb(rs)I	11.40	10.81
NGC 5457.....	SAB(rs)cd	6	1.1	2.46	0.03	8.31	Sc(s)I	8.18	7.89
NGC 5474.....	SA(s)cd	6	8	1.68	0.05	11.28	Scd(s)IV pec	11.31	11.01
NGC 5556.....	SAB(rs)d	7	6.1	1.60	0.10	(12)	SBc(sr)II–III	11.88	11.42
NGC 5566.....	SB(r)ab	2	3.6	1.82	0.48	11.46	SBa(r)II	11.35	10.35
NGC 5584.....	SAB(rs)cd	6	2.8	1.53	0.14	(11.7)	Sc(s)I–II	11.95	11.57
NGC 5585.....	SAB(s)d	7	7.6	1.76	0.19	11.2	Sd(s)IV	11.37	10.94
NGC 5669.....	SAB(rs)cd	6	6.7	1.60	0.15	(11.8)	Sc/SBc(r)I–II	12.00	11.62
NGC 5676.....	SA(rs)bc	4	3.3	1.60	0.32	11.87	Sc(s)II	11.68	11.15
NGC 5701.....	RSB(rs)0/a	0	...	1.63	0.02	11.64	(PR)SBa	11.8	11.8
NGC 5713.....	SAB(rs)bc pec	4	...	1.44	0.05	11.84	Sbc(s) pec	12.00	11.68
NGC 5746.....	SAB(rs)b	3	4.5	1.87	0.75	11.29	Sb(s)	11.55	10.24
NGC 5792.....	SB(rs)b	3	2.1	1.84	0.60	12.08	SBb(s)I.3	11.72	10.54
NGC 5838.....	SA0	−3	...	1.62	0.45	11.92	$S0_2(5)$	11.76	11.72
NGC 5846.....	E0	−5	...	1.61	0.03	11.05	$S0_1(0)$	11.17	11.13

TABLE 1—*Continued*

	RC3 Data						RSA Data		
Galaxy	Morphological Type	T[a]	Luminosity Class[b]	log D_{25}[c]	log R_{25}[d]	B_T[e]	Morphological Type	B_T[f]	$B_T^{0,i}$[g]
NGC 5850.....	SB(r)b	3	2.9	1.63	0.06	11.54	SBb(sr)I–II	11.71	11.20
NGC 5866.....	SA0	−1	...	1.67	0.38	10.74	$S0_3(8)$	10.86	10.86
NGC 5907.....	SA(s)c	5	3	2.10	0.96	11.12	Sc (on edge)	11.15	10.28
NGC 5985.....	SAB(r)b	3	1.1	1.74	0.27	11.87	SBb(r)I	11.80	11.01
NGC 6015.....	SA(s)cd	6	3.9	1.73	0.40	11.69	Sc(s)II–III	11.73	11.06
NGC 6215.....	SA(s)c	5	4.1	1.33	0.08	12	Sc(s)II	11.89	10.83
NGC 6217.....	RSB(rs)bc	4	2.8	1.48	0.08	11.79	RSBbc(s)II	11.86	11.41
NGC 6221.....	SB(s)c	5	3.6	1.55	0.16	10.66	Sbc(s)II–III	11.52	10.47
NGC 6300.....	SB(rs)b	3	3.1	1.65	0.18	10.98	SBb(s)II pec	11.04	9.96
NGC 6340.....	SA(s)0/a	0	...	1.51	0.04	11.87	Sa(r)I	11.90	11.29
NGC 6503.....	SA(s)cd	6	5.2	1.85	0.47	10.91	Sc(s)II.8	10.93	10.15
NGC 6643.....	SA(rs)c	5	2.8	1.58	0.30	11.73	Sc(s)II	11.74	11.07
NGC 6744.....	SAB(r)bc	4	3.3	2.30	0.19	9.14	Sbc(r)II	9.24	8.63
NGC 6753.....	RSA(r)b	3	1.5	1.39	0.06	11.97	Sb(r)I	11.93	11.25

[a] The location along the Hubble sequence, as defined in RC3.
[b] As defined in RC3.
[c] The optical diameter parameter defined in RC3.
[d] The parameter describing the ratio of the major axis to the minor axis, as defined in RC3.
[e] The *B*-band apparent magnitude, as defined in RC3. Values in parentheses are magnitudes corrected for extinction and redshift.
[f] The *B*-band apparent magnitude, as defined in RSA.
[g] The *B*-band apparent magnitude with corrections for extinction, as defined in RSA.

3. OBSERVATIONS AND DATA REDUCTION

3.1. *ISO Photometry*

3.1.1. *Observations*

The sample was observed at 60, 100, and 180 μm using PHT-C far-infrared camera (Lemke et al. 1996). The C100 3×3 pixel array, with 43″.5 pixels, was used to obtain images at 60 and 100 μm, and the C200 2×2 pixel array, with 90″ pixels, was used to obtain 180 μm photometry. At 60, 100, and 180 μm, the resolution for *ISO* is 50″, 84″, and 150″, respectively. The exposure in each filter was 16 s, with equal time on-target and at a nearby sky position. The sky positions were chosen by using the *IRAS* infrared sky maps produced by the Infrared Processing and Analysis Center to find reference positions that were optimum for subtracting out infrared background from the target images.

Images at 12 μm were obtained using the *ISO* infrared camera, ISOCAM (Cesarsky et al. 1996), with the LW10 filter, which is identical to the 12 μm *IRAS* filter. An imaging scale of 3″ pixel^{-1} was selected, and the diffraction-limited

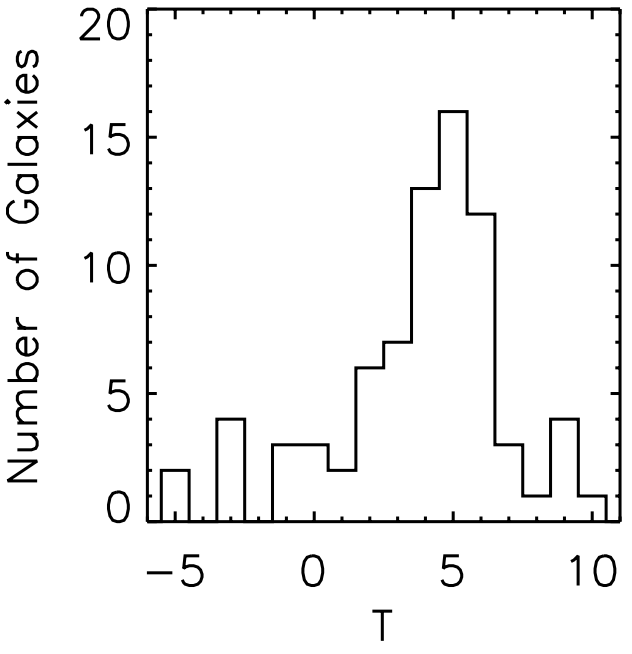

Fig. 1.—Histogram of T values (representing Hubble types) from the RC3 for the galaxies in the sample.

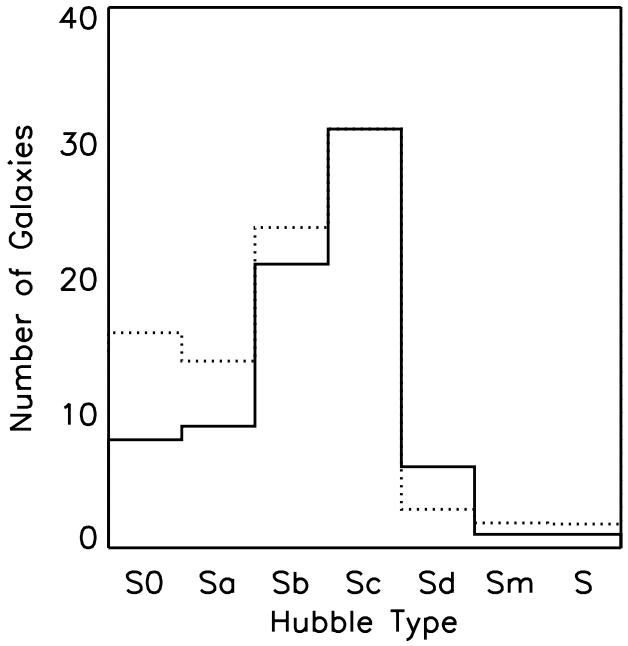

Fig. 2.—Histogram of Hubble types from the RSA for the galaxies in the sample (*solid line*) compared to the total of each Hubble type in the RSA (*dotted line*). The RSA totals have been normalized so that they match the sample totals for Sc galaxies.

TABLE 2

DATA ON MORPHOLOGY, NUCLEAR ACTIVITY, AND ENVIRONMENT FOR ATLAS GALAXIES

Galaxy	Arm Class[a]	Nuclear Activity[b]	Distance (Mpc)	Other Information	Reference
NGC 55	...	...	1.3	...	...
NGC 289	12	...	19.4	Interacting with dwarf companion	1
NGC 1512.....	6	...	9.5	Interacting with NGC 1510	2
NGC 1569.....	1	H	1.6	...	...
NGC 3359.....	5	H	19.2	...	...
NGC 3556.....	...	H	14.1	...	...
NGC 3898.....	3	T2	21.9	...	...
NGC 4062.....	3	H	9.7	...	...
NGC 4088.....	8	H	17.0	Interacting with NGC 4085	3
NGC 4096.....	...	H	8.8	...	...
NGC 4100.....	...	H	17.0	...	...
NGC 4136.....	9	H	9.7	...	...
NGC 4157.....	...	H	17.0	...	...
NGC 4203.....	...	L1.9	9.7	...	...
NGC 4236.....	...	H	2.2	...	...
NGC 4244.....	...	H	3.1	...	...
NGC 4274.....	8	H	9.7	...	...
NGC 4314.....	12	L2	9.7	Double-barred galaxy	4
NGC 4395.....	1	S1.8	3.6	...	...
NGC 4414.....	3	T2:	9.7	...	...
NGC 4448.....	...	H	9.7	...	...
NGC 4559.....	...	H	9.7	...	...
NGC 4605.....	...	H	4.0	...	...
NGC 4618.....	4	H	7.3	Interacting with NGC 4625	5
NGC 4631.....	...	H	6.9	Interacting with NGC 4656	6
NGC 4710.....	...	H	16.8	...	...
NGC 4725.....	6	S2:	12.4	Interacting with NGC 4747	7
NGC 4826.....	6	T2	4.1	Counterrotating gas disk; leading spiral arm	8, 9
NGC 4945.....	...	...	5.2	...	...
NGC 4976.....	...	...	18.6	...	...
NGC 4984.....	...	...	21.3	...	...
NGC 5005.....	3	L1.9	21.3	Interacting with NGC 5033	10
NGC 5033.....	9	S1.5	18.7	Interacting with NGC 5005	10
NGC 5054.....	5	...	27.3	...	...
NGC 5055.....	3	T2	7.2	...	...
NGC 5068.....	2	...	6.7	...	...
NGC 5087.....	...	...	27.8	...	...
NGC 5101.....	...	...	27.4	...	...
NGC 5102.....	...	...	3.5	...	...
NGC 5112.....	5	H	20.5	Interacting with NGC 5107	11
NGC 5161.....	...	...	33.5	...	...
NGC 5170.....	...	...	24.0	...	...
NGC 5204.....	1	H	4.8	...	...
NGC 5236.....	9	...	4.7	...	...
NGC 5247.....	9	...	22.2	...	...
NGC 5300.....	2	H	23.1	...	...
NGC 5334.....	2	...	24.7	...	...
NGC 5364.....	9	H	25.5	...	...
NGC 5371.....	9	L2	37.8	...	...
NGC 5457.....	9	H	5.4	Interacting with NGC 5474	12
NGC 5474.....	2	H	6.0	Interacting with NGC 5457	12
NGC 5556.....	1	...	20.9	...	...
NGC 5566.....	...	L2	26.4	Interacting with NGC 5560, NGC 5569, NGC 5577	10
NGC 5584.....	5	...	27.4	...	...
NGC 5585.....	1	H	7.0	...	...
NGC 5669.....	5	H	24.9	...	...
NGC 5676.....	3	H	34.5	...	...
NGC 5701.....	...	T2:	26.1	...	...
NGC 5713.....	4	...	30.4	...	...
NGC 5746.....	...	T2	29.4	Interacting with NGC 5740; possible bar	13, 14
NGC 5792.....	...	...	30.6	...	...
NGC 5838.....	...	T2::	28.5	...	...
NGC 5846.....	...	T2:	28.5	Interacting with NGC 5846A	13
NGC 5850.....	8	L2	28.5	Probably interacted with NGC 5846; double bar	15, 16

TABLE 2—*Continued*

Galaxy	Arm Class[a]	Nuclear Activity[b]	Distance (Mpc)	Other Information	Reference
NGC 5866.....	...	T2	15.3	Interacting with NGC 5907	13
NGC 5907.....	...	H:	14.9	Interacting with NGC 5866	13
NGC 5985.....	9	L2	39.2	...	...
NGC 6015.....	...	H	17.5	...	...
NGC 6215.....	12	...	20.5	Interacting with NGC 6221	17
NGC 6217.....	5	H	23.9	...	...
NGC 6221.....	...	...	19.4	Interacting with NGC 6215	17
NGC 6300.....	6	...	14.3	...	...
NGC 6340.....	...	L2	22.0	...	...
NGC 6503.....	...	T2/S2:	6.1	...	...
NGC 6643.....	5	H	25.5	...	...
NGC 6744.....	...	...	10.4	...	...
NGC 6753.....	8	...	...	...	...

[a] Classes defined in Elmegreen & Elmegreen 1987. Classes 1–4 indicate flocculent spiral arms, while classes 5–12 indicate grand design spiral arms.

[b] Designations as given in Ho et al. 1997. S: Seyfert; L: LINER; H: H II nucleus; T: Transitional. The number indicates the type of AGN activity. Single colons indicate uncertain classifications. Double colons indicate highly uncertain classifications. Note that the classifications are based strictly on optical line ratios and that not all galaxies have been classified.

REFERENCES.—(1) Arp 1981. (2) Hawarden et al. 1979. (3) van Moorsel 1983b. (4) Benedict et al. 1993. (5) van Moorsel 1983a. (6) Arp 1966. (7) Haynes 1979. (8) Braun et al. 1992. (9) van Driel & Buta 1993. (10) Helou, Salpeter, & Terzian 1982. (11) van Moorsel 1983a. (12) Davies, Davidson, & Johnson 1980. (13) Sandage & Bedke 1994. (14) Kuijken & Merrifield 1995. (15) Prieto et al. 1997. (16) Friedli et al. 1996. (17) Pence & Blackman 1984.

resolution in the images was $\sim 4''$. The on-target integration time was 396 s in most cases. The observations were made in a microscan raster mode. The telescope pointed at a total of 12 positions in a 6×2 pattern with raster step sizes of $15''$ and $10''$. This produced a total scanned region of 171×106 arcsec^2.

The total observing time in the *ISO* Central Programme allocated to this project was about 27 hr. In this time 74 galaxies were observed, and data for four more were obtained in the *ISO* Supplementary Time. The TDT numbers for the observations are given in Table 4.

TABLE 3
MORPHOLOGICAL AND ACTIVITY CLASSIFICATIONS

Type	Number
E	2
S0+	4
S0−	3
S0/a	3
Sa	2
Sab	6
Sb	7
Sbc	13
Sc	16
Scd	12
Sd	3
Sdm	1
Sm	4
Im	1
SA	29
SAB	22
SB	24
(Bar unclassified)	2
Seyfert	3
LINER	8
H II Nuclei	31
Transitional	10
(Nuclei unclassified)	25

3.1.2. *ISOPHOT Data Reduction*

The data were reduced using general batch processing with ISOPHOT Interactive Analysis (PIA) 8.0 (Gabriel et al. 1997; Laureijs et al. 2000).[14] Since it took the ISOPHOT

[14] See http://www.iso.vilspa.esa.es/manuals/HANDBOOK/V/pht_hb.

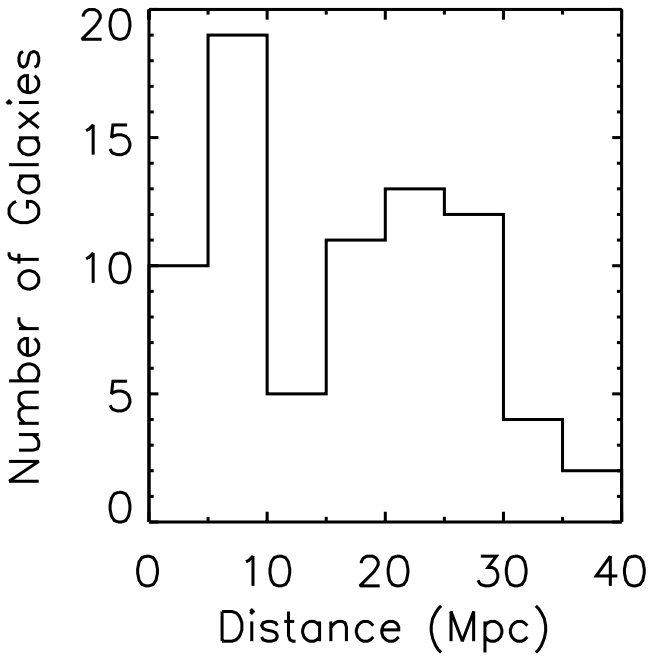

FIG. 3.—Histogram of distances in megaparsecs from Tully (1988) for the galaxies in the sample.

TABLE 4

ISO Observation Information

Galaxy	C100 TDT Number		C200 TDT Number		TDT Number for CAM01
	PHT37	PHT39	PHT37	PHT39	
NGC 55	23200413	23200414	23200415	23200416	23200417
NGC 289	23601561	23601562	23601563	23601564	23601565
NGC 1512.....	84802143	84802144	84802145	84802146	84802147
NGC 1569.....	86301513	86301514	86301515	86301516	86301517
NGC 3359.....	20600437	20600438	20600439	20600440	20600441
NGC 3556.....	20600543	20600544	20600545	20600546	20600547
NGC 3898.....	20600749	20600750	20600751	20600752	20600753
NGC 4062.....	20200655	20200656	20200657	20200658	20200659
NGC 4088.....	20600861	20600862	20600863	20600864	20600865
NGC 4096.....	20600967	20600968	20600969	20600970	20600971
NGC 4100.....	20601073	20601074	20601075	20601076	20601077
NGC 4136.....	20200799	20200780	20200781	20200782	20200783
NGC 4157.....	20601185	20601186	20601187	20601188	20601189
NGC 4203.....	22902001	22902002	22902003	22902004	22902005
NGC 4236.....	22400913	22400914	22400915	22400916	22400917
NGC 4244.....	22902319	22902320	22902321	22902322	22902323
NGC 4274.....	22901125	22901126	22901127	22901128	22901129
NGC 4314.....	22901231	22901232	22901233	22901234	22901235
NGC 4395.....	22902237	22902238	22902239	22902240	22902241
NGC 4414.....	22901743	22901744	22901745	22901746	22901747
NGC 4448.....	22900549	22900550	22900551	22900552	22900553
NGC 4559.....	22900455	22900456	22900457	22900458	22900459
NGC 4605.....	20801161	20801162	20801163	20801164	20801165
NGC 4618.....	22902667	22902668	22902669	22902670	22902671
NGC 4631.....	22901973	22901974	22901975	22901976	22901977
NGC 4710.....	21801479	21801480	21801481	21801482	21801483
NGC 4725.....	21501485	21501486	21501487	21501488	21501489
NGC 4826.....	22803201	22803202	22803203	22803204	22803205
NGC 4945.....	26802007	26802008	26802009	26802010	26802011
NGC 4976.....	28000713	28000714	28000715	28000716	28000717
NGC 4984.....	25701219	25701220	25701221	25701222	25701223
NGC 5005.....	23801225	23801226	23801227	23801228	23801229
NGC 5033.....	22101031	22101032	22101033	22101034	22101035
NGC 5054.....	25701543	25701544	25701545	25701546	25701547
NGC 5055.....	23801337	23801338	23801339	23801340	23801341
NGC 5068.....	25701849	25701850	25701851	25701852	25701853
NGC 5087.....	25701755	25701756	25701757	25701758	25701759
NGC 5101.....	25200961	25200962	25200963	25200964	25200965
NGC 5102.....	24901773	24901774	24901775	24901776	24901777
NGC 5112.....	23801167	23801168	23801169	23801170	23801171
NGC 5128.....	24901679	24901680	24901681	24901682	...
NGC 5161.....	25201085	25201086	25201087	25201088	25201089
NGC 5170.....	26001307	26001308	26001309	26001310	26001311
NGC 5204.....	20801301	20801302	20801303	20801304	20801305
NGC 5236.....	25600825	25600826	25600827	25600828	25600829
NGC 5247.....	26001137	26001138	26001139	26001140	26001141
NGC 5300.....	25402643	25402644	25402645	25402646	25402647
NGC 5334.....	24201449	24201450	24201451	24201452	24201453
NGC 5364.....	24201367	24201368	24201369	24201370	24201371
NGC 5371.....	26901355	26901356	26901357	26901358	26901359
NGC 5457.....	26902579	26902580	26902581	26902528	26902583
NGC 5474.....	26902085	26902086	26902087	26902088	26902089
NGC 5556.....	28400119	28400120	28400121	28400122	28400123
NGC 5566.....	26002413	26002414	26002415	26002416	26002417
NGC 5584.....	26002625	26002626	26002627	26002628	26002629
NGC 5585.....	20801207	20801208	20801209	20801210	20801211
NGC 5669.....	27001137	27001138	27001139	27001140	27001141
NGC 5676.....	26901843	26901844	26901845	26901846	26901847
NGC 5701.....	27001349	27001350	27001351	27001352	27001353
NGC 5713.....	28400855	28400856	28400857	28400858	28400859
NGC 5746.....	28401461	28401462	28401463	28401464	28401465
NGC 5792.....	28400767	28400768	28400769	28400770	28400771
NGC 5838.....	28401373	28401374	28401375	28401376	28401377

TABLE 4—*Continued*

Galaxy	C100 TDT Number		C200 TDT Number		TDT Number for CAM01
	PHT37	PHT39	PHT37	PHT39	
NGC 5846.....	28401179	28401180	28401181	28401182	28401183
NGC 5850.....	28401001	28401002	28401003	28401004	28401005
NGC 5866.....	26902785	26902786	26902787	26902788	26902789
NGC 5907.....	26902907	26902908	26902909	26902910	26902911
NGC 5985.....	26903219	26903220	26903221	26903222	26903223
NGC 6015.....	26903325	26903326	26903327	26903328	26903329
NGC 6215.....	27301443	27301444	27301445	27301446	27301447
NGC 6217.....	25202837	25202838	25202839	25202840	25202841
NGC 6221.....	27301549	27301550	27301551	27301552	27301553
NGC 6300.....	27301661	27301662	27301663	27301664	27301665
NGC 6340.....	25501255	25501256	25501257	25501258	25501259
NGC 6503.....	25500973	25500974	25500975	25500976	25500977
NGC 6643.....	25500679	25500680	25500681	25500682	25500683
NGC 6744.....	84700901	84700902	84700903	84700904	...
NGC 6753.....	84701007	84701008	84701009	84701010	...

detectors some time to stabilize, we discarded the first 25% of the data. We used ramp linearization and the two-threshold method for ramp deglitching. We applied the reset interval correction, subtracted the dark current, and linearized the signal. We used the Fine Calibration Source 1 responsivities in PIA to photometrically calibrate the data.

The output from PIA 8.0 was then further processed following a method similar to that used by Radovich et al. (1999). First, we subtracted the off-target flux from the on-target flux. Then, for the 60 and 100 μm data, we performed a correction so that we could separate flux densities for central sources from flux densities for extended sources. We assumed that each galaxy consisted of a point source centered on the array (f_c) and a smooth, extended source that is homogeneously distributed throughout the inner 135″ (f_e for the whole aperture). The measured flux density f_m in the central pixel will be

$$f_m(45'') = A_{45} f_c + \frac{f_e}{9} , \quad (1)$$

and the measured flux density in the entire array will be

$$f_m(135'') = A_{135} f_c + f_e, \quad (2)$$

where A_{45} and A_{135}, tabulated in Table 5, are the fractions of the point-spread function falling within the 45″ and 135″ apertures, respectively (Laureijs 1999).[15] Solving this for f_c gives

$$f_c = \frac{9 f_m(45'') - f_m(135'')}{9 A_{45} - A_{135}} . \quad (3)$$

Solving for f_e gives

$$f_e = \frac{f_m(135'') - A_{135} f_c}{9} . \quad (4)$$

These formulae can then be applied to calculating the true flux densities f_t within 45″ and 135″:

$$f_t(45'') = f_c + \frac{f_e}{9} , \quad (5)$$

$$f_t(135'') = f_c + f_e . \quad (6)$$

The only galaxy for which this analysis was not used is NGC 55, where the emission is so extended that this analysis fails. Instead, the reported flux densities assume that the source consists of only an extended component.

3.1.3. *ISOCAM Data Reduction*

ISOCAM data reduction was performed in two steps. In the first step, the data were processed with ISOCAM Interactive Analysis (CIA) 3.0 (Ott et al. 1997; Blommaert et al. 2001).[16] The data were processed with the model dark current subtraction and the "tcor" deglitching routine followed by manual glitch removal (deglitching routines other than "tcor" were used for objects that were either very faint or very bright). In a few galaxies, some pixels in individual frames had excessive hysteresis from bright mid-infrared nuclear emission. These pixels on which the bright nuclei appeared were masked in the frames following. The masks for deglitching and hysteresis correction were then saved.

After these steps, we used the CIR data processing software, an implementation of the algorithms of Starck et al. (1999) realized by P. Chanial. First the data, along with the deglitching mask from CIA, were read into the CIR environment. Then the "correct_dark_vilspa" routine was applied to correct for the dark current. This first applied the Biviano and Sauvage dark correction, then a second-order correction dependent on the detector temperature and time since activation, and finally a short drift correction. This was followed by applying the deglitching masks to remove the glitches in the maps (although in the few galaxies without any manual deglitching in CIA, the "correct_-

[15] See http://www.iso.vilspa.esa.es/users/expl_lib/PHT/c200fpsf02.ps.gz.

[16] See http://www.iso.vilspa.esa.es/manuals/HANDBOOK/III/cam_hb.

TABLE 5
POINT-SPREAD FUNCTION CORRECTIONS FOR ISOPHOT DATA

Wavelength (μm)	Aperture (arcsec)	Correction Factor
60.....	45	0.69
	135	0.8096
100.....	45	0.57
	135	0.7742

glitch_mr'' routine was applied). Next, the ''correct_transient_fs'' routine, based on the Fouks-Schubert transient correction method (Coulais & Abergel 2000), was applied to the data to remove transient effects. Then all frames from the first pointings were masked because the corrections are imperfect at the beginnings of the observations, and a 2 pixel border around each frame was masked because of poor flat-fielding for these pixels. The frames were flat-fielded using CIR's library flat field, and the images were combined to produce a final image. The final images were converted to mJy pixel^{-1} and written to fits files.

3.2. *JHK Photometry*

3.2.1. *Observations*

Most of the *JHK* observations were made with QUIRC at the f/10 focus on the UH 2.2 meter telescope on UT dates 1999 April 28, 2000 April 14, 2000 April 17, 2000 May 15–17, 2001 April 10, and 2001 May 4–5. In this configuration, we obtained 1024×1024 pixel^2 images with a plate scale of $0\farcs1866$ pixel^{-1}. Since the seeing for the observations was typically $0\farcs6$–$0\farcs7$ at *K*, this scale oversampled the point-spread function. For NGC 1512, observations were made on UT date 2000 September 17, with the imager on SPEX at the NASA Infrared Telescope Facility (IRTF). The SPEX imager produced 512×512 pixel images with a resolution of $0\farcs12$ pixel^{-1}. For NGC 289 and NGC 1569, observations were made on UT dates 1998 January 22 and 25, with NSFCAM at the IRTF. NSFCAM produced 256×256 pixel images at a plate scale of $0\farcs3$ pixel^{-1}. For all IRTF observations, the seeing was typically $0\farcs7$ at *K*.

The observing techniques used were identical for all observations. The observations consisted of a four-point dither pattern, with alternate frames taken off-source to measure sky emission. The offset between the on-target frames was $5''$. Flux standards from the UKIRT faint source standards (Hawarden et al. 2001) were observed with either a method identical to the galaxy observations or a four-point dither pattern with no offset for sky subtraction (using the four frames with the standard star removed by median filtering for subtracting sky emission). These stars were observed at air masses both near the air mass of the target and at high air masses.

3.2.2. *Data Reduction*

The off-target frames were median combined to produce a background frame that was then subtracted from each individual on-target frame. The four on-target frames were then median combined to form a final image. Regions not overlapping were removed. The data for the flux standards were processed the same way.

The flux standards were used to create conversion factors for converting counts into fluxes as a function of air mass. These conversion factors were then applied to the uncalibrated galaxy images to produce flux-calibrated images. To check the reliability of these conversion factors, a conversion factor calculated from two flux standard observations was applied to a third. The flux of the standard in the third observation was checked to make sure it did not deviate from those given by Hawarden et al. (2001). This check demonstrated that the flux calibration was good to about 0.2 mag.

4. PHOTOMETRY

4.1. *Far-Infrared Photometry*

4.1.1. *Far-Infrared Flux Densities*

Table 6 gives the 60 and 100 μm fluxes for the central and extended sources, and Table 7 gives the far-infrared flux densities measured within various apertures. The accuracy for these measurements, which is limited by the accuracy of the calibration, is 20% (Klaas et al. 2000).[17] Also included in Table 7 are total far-infrared flux densities calculated from the *ISO* data. For comparison, far-infrared flux densities and total far-infrared fluxes calculated from data in the *IRAS* Faint Source Catalog (FSC; Moshir et al. 1990) are included in Table 8.

We determined the relation between the fluxes we measured with ISOPHOT at 60, 100, and 180 μm and the total far-infrared flux by finding a linear relationship between the two sets of values. (For calculating these total fluxes, we assume that the 180 μm fluxes from within $180''$ correspond to the same sources as those producing the 60 and 100 μm fluxes within $135''$.) First, we generated blackbodies with temperatures ranging from 20 to 40 K with dust emissivities proportional to λ^{-n}, where n ranged from 0 to 2. For each blackbody, we calculated the total integrated flux between 40 and 220 μm as well as the total flux that would be measured within the three *ISO* bands that we observed. We then found a least-squares fit between the total blackbody energy and the three *ISO* bands. The equation giving the relation is

$$F_{\rm FIR} = 1.89(F_{60} + F_{100} + F_{180}) \ , \tag{7}$$

where

$$F_{60} = (1.36 \times 10^{-14}) f_{60} \ , \tag{8}$$

$$F_{100} = (0.958 \times 10^{-14}) f_{100} \ , \tag{9}$$

and

$$F_{180} = (0.439 \times 10^{-14}) f_{180} \ , \tag{10}$$

with $F_{\rm FIR}$, F_{60}, F_{100}, and F_{180} representing flux in units of W m^{-2} and f_{60}, f_{100}, and f_{180} representing flux densities in units of Jy. This analysis follows a similar process described by Fullmer & Lonsdale (1989) for calculating total far-infrared fluxes from *IRAS* data. Figure 4 demonstrates how a 30 K blackbody with varying emissivity functions is sampled by this wave band.

[17] See http://www.iso.vilspa.esa.es/users/expl_lib/PHT/calacc_v4.ps.gz.

TABLE 6
FAR-INFRARED FLUXES FOR CENTRAL AND EXTENDED COMPONENTS

Galaxy	60 μm Flux Densities (Jy)		100 μm Flux Densities (Jy)	
	Central Source	Extended Source	Central Source	Extended Source
NGC 55	0.0	5.04	0.0	14.0
NGC 289	3.10	2.89	7.10	6.87
NGC 1512.....	1.04	1.53	1.81	3.06
NGC 1569.....	20.5	16.2	...	...
NGC 3359.....	1.63	4.02	2.81	7.41
NGC 3556.....	8.47	11.8	12.1	28.3
NGC 3898.....	0.369	0.846	0.513	2.31
NGC 4062.....	0.995	1.79	2.69	6.74
NGC 4088.....	5.75	13.3	11.6	32.0
NGC 4096.....	2.14	4.15	4.62	9.75
NGC 4100.....	5.38	4.18	9.83	8.11
NGC 4136.....	0.422	1.42	0.659	4.44
NGC 4157.....	5.79	7.42	12.2	22.8
NGC 4203.....	0.749	0.508	1.10	1.53
NGC 4236.....	0.226	1.52	0.293	1.75
NGC 4244.....	0.433	1.10	0.987	3.61
NGC 4274.....	3.26	1.18	6.98	5.89
NGC 4314.....	3.04	0.805	6.06	3.27
NGC 4395.....	0.390	0.569	0.288	3.20
NGC 4414.....	13.0	9.47	29.7	29.1
NGC 4448.....	0.880	1.20	2.00	3.93
NGC 4559.....	1.77	3.38	3.47	12.6
NGC 4605.....	2.83	7.96	5.43	17.1
NGC 4618.....	0.900	2.75	1.53	7.77
NGC 4631.....	18.1	39.8	34.3	83.9
NGC 4710.....	4.78	0.229	9.61	3.50
NGC 4725.....	0.445	0.970	0.775	5.73
NGC 4826.....	22.2	7.66	45.9	26.5
NGC 4945.....	...	...	...	...
NGC 4976.....	...	...	...	...
NGC 4984.....	8.58	1.75	12.4	3.81
NGC 5005.....	...	...	...	...
NGC 5033.....	8.11	4.74	18.3	16.2
NGC 5054.....	7.19	4.49	12.8	12.2
NGC 5055.....	8.94	17.4	20.8	61.0
NGC 5068.....	...	...	...	...
NGC 5087.....	1.10	0.822	3.01	1.66
NGC 5101.....	0.859	0.593	1.67	2.44
NGC 5102.....	0.470	0.837	1.12	1.83
NGC 5112.....	0.513	1.10	1.01	3.90
NGC 5161.....	...	...	...	...
NGC 5170.....	0.226	1.42	0.754	3.39
NGC 5204.....	0.779	1.91	1.33	4.05
NGC 5236.....	112.	47.8	148.	131.
NGC 5247.....	3.11	5.86	5.91	15.4
NGC 5300.....	0.416	1.37	1.00	3.49
NGC 5334.....	0.394	0.841	1.00	3.10
NGC 5364.....	0.390	1.79	1.38	7.29
NGC 5371.....	0.417	3.89	1.31	9.80
NGC 5457.....	1.61	6.47	2.07	24.3
NGC 5474.....	0.338	2.14	0.571	2.82
NGC 5556.....	0.403	1.77	0.452	3.24
NGC 5566.....	0.929	1.13	2.59	3.66
NGC 5584.....	0.371	2.75	1.15	5.31
NGC 5585.....	0.394	2.19	0.643	2.63
NGC 5669.....	0.620	1.52	1.67	4.07
NGC 5676.....	4.94	5.75	10.1	14.5
NGC 5701.....	0.240	0.461	0.486	1.60
NGC 5713.....	17.1	4.02	27.1	11.5
NGC 5746.....	0.596	2.78	2.18	6.70
NGC 5792.....	7.04	1.85	11.2	7.55
NGC 5838.....	0.789	0.812	1.56	1.56
NGC 5846.....	0.146	0.789	0.450	1.68
NGC 5850.....	0.386	1.79	1.30	3.59
NGC 5866.....	3.79	2.01	9.85	5.00
NGC 5907.....	2.42	4.64	7.30	17.9
NGC 5985.....	0.233	2.15	0.737	4.40
NGC 6015.....	0.520	3.25	2.65	7.16
NGC 6215.....	15.3	9.67	22.2	22.4
NGC 6217.....	7.33	3.72	10.8	7.56
NGC 6221.....	24.1	13.8	37.6	36.6
NGC 6300.....	6.45	7.50	9.45	19.5
NGC 6340.....	0.298	1.79	0.854	0.936
NGC 6503.....	2.28	4.82	4.98	14.3
NGC 6643.....	6.52	4.43	12.8	11.8
NGC 6744.....	0.550	2.15	0.132	8.76
NGC 6753.....	5.97	3.44	13.6	9.62

Total *IRAS* far-infrared fluxes were calculated using the equation

$$F_{\rm FIR} = 1.26(F_{60} + F_{100}), \tag{11}$$

where

$$F_{60} = (2.58 \times 10^{-14}) f_{60} \tag{12}$$

and

$$F_{100} = (1.00 \times 10^{-14}) f_{100}, \tag{13}$$

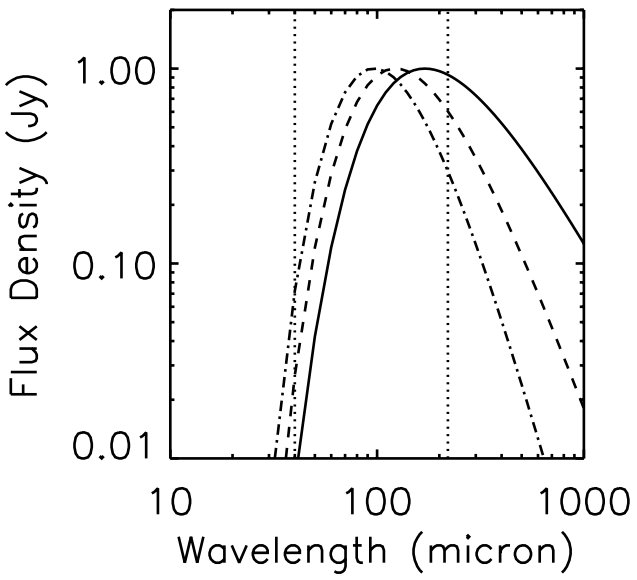

FIG. 4.—Plots of a 30 K blackbody (*solid line*), a blackbody with a λ^{-1} emissivity (*dashed line*), and a blackbody with a λ^{-2} emissivity (*dot-dashed line*). The blackbodies have been normalized so that their peaks equal 1. The dotted lines show the 40–220 μm band within which we measure fluxes. This figure demonstrates that the 40–220 μm wave band is effective in sampling the peak emission of 30 K blackbodies. Therefore, fluxes calculated for this wave band should be representative of the total emission from targets with similar dust temperatures and emissivity functions.

TABLE 7

ISO Far-Infrared Flux Data in Set Apertures

Galaxy	Flux Densities (Jy)					Total *ISO* Far-Infrared Flux ($W\ m^{-2}$)
	60 μm		100 μm		180 μm	
	(45″)	(135″)	(45″)	(135″)	(180″)	(135″)
NGC 55	0.560	5.04	1.56	14.0	32.1	6.49×10^{-13}
NGC 289	3.42	5.99	7.86	14.0	14.8	5.30×10^{-13}
NGC 1512.....	1.21	2.58	2.15	4.87	6.17	2.06×10^{-13}
NGC 1569.....	22.3	36.7	...	...	...	...
NGC 3359.....	2.07	5.65	3.63	10.2	12.2	4.32×10^{-13}
NGC 3556.....	9.78	20.3	15.2	40.4	47.1	1.64×10^{-12}
NGC 3898.....	0.463	1.21	0.769	2.82	3.25	1.09×10^{-13}
NGC 4062.....	1.19	2.78	3.44	9.44	11.6	3.38×10^{-13}
NGC 4088.....	7.22	19.0	15.1	43.6	46.2	1.66×10^{-12}
NGC 4096.....	2.60	6.28	5.70	14.4	20.2	5.89×10^{-13}
NGC 4100.....	5.85	9.56	10.7	17.9	18.6	7.25×10^{-13}
NGC 4136.....	0.580	1.85	1.15	5.10	5.60	1.86×10^{-13}
NGC 4157.....	6.61	13.2	14.8	35.0	44.2	1.34×10^{-12}
NGC 4203.....	0.806	1.26	1.27	2.63	2.64	1.02×10^{-13}
NGC 4236.....	0.395	1.75	0.487	2.04	3.78	1.13×10^{-13}
NGC 4244.....	0.556	1.54	1.39	4.60	7.20	1.83×10^{-13}
NGC 4274.....	3.39	4.44	7.63	12.9	14.9	4.71×10^{-13}
NGC 4314.....	3.13	3.85	6.42	9.33	5.43	3.13×10^{-13}
NGC 4395.....	0.454	0.959	0.643	3.49	6.16	1.39×10^{-13}
NGC 4414.....	14.1	22.5	33.0	58.8	54.5	2.10×10^{-12}
NGC 4448.....	1.01	2.08	2.43	5.93	6.11	2.12×10^{-13}
NGC 4559.....	2.15	5.15	4.87	16.1	18.8	5.80×10^{-13}
NGC 4605.....	3.71	10.8	7.33	22.5	22.2	8.70×10^{-13}
NGC 4618.....	1.20	3.65	2.39	9.29	11.4	3.56×10^{-13}
NGC 4631.....	22.6	57.9	43.6	118.	93.9	4.41×10^{-12}
NGC 4710.....	4.80	5.01	10.0	13.1	8.99	4.40×10^{-13}
NGC 4725.....	0.553	1.41	1.41	6.50	15.6	2.83×10^{-13}
NGC 4826.....	23.1	29.9	48.8	72.4	51.8	2.51×10^{-12}
NGC 4945.....	...	...	...	...	...	...
NGC 4976.....	...	...	...	...	...	...
NGC 4984.....	8.77	10.3	12.9	16.2	9.19	6.36×10^{-13}
NGC 5005.....	...	...	...	...	...	...
NGC 5033.....	8.64	12.9	20.1	34.5	37.4	1.27×10^{-12}
NGC 5054.....	7.69	11.7	14.1	25.0	26.7	9.74×10^{-13}
NGC 5055.....	10.9	26.3	27.6	81.9	103.	3.01×10^{-12}
NGC 5068.....	...	...	...	...	...	...
NGC 5087.....	1.19	1.92	3.20	4.67	1.71	1.48×10^{-13}
NGC 5101.....	0.924	1.45	1.94	4.11	5.57	1.58×10^{-13}
NGC 5102.....	0.563	1.31	1.32	2.95	4.36	1.23×10^{-13}
NGC 5112.....	0.635	1.61	1.45	4.92	5.66	1.77×10^{-13}
NGC 5161.....	...	...	...	...	...	...
NGC 5170.....	0.384	1.65	1.13	4.14	6.61	1.72×10^{-13}
NGC 5204.....	0.99	2.69	1.78	5.38	5.17	2.09×10^{-13}
NGC 5236.....	117.	160.	162.	279.	192.	1.08×10^{-11}
NGC 5247.....	3.76	8.98	7.62	21.3	29.5	8.62×10^{-13}
NGC 5300.....	0.568	1.78	1.38	4.49	5.79	1.75×10^{-13}
NGC 5334.....	0.488	1.24	1.35	4.10	5.30	1.50×10^{-13}
NGC 5364.....	0.589	2.18	2.19	8.67	15.0	3.38×10^{-13}
NGC 5371.....	0.850	4.31	2.40	11.1	20.2	4.80×10^{-13}
NGC 5457.....	2.33	8.07	4.77	26.4	44.1	1.05×10^{-12}
NGC 5474.....	0.575	2.48	0.885	3.39	5.25	1.69×10^{-13}
NGC 5556.....	0.600	2.18	0.812	3.69	4.26	1.58×10^{-13}
NGC 5566.....	1.05	2.06	3.00	6.25	7.51	2.28×10^{-13}
NGC 5584.....	0.677	3.12	1.74	6.46	6.75	2.53×10^{-13}
NGC 5585.....	0.638	2.59	0.935	3.27	4.89	1.66×10^{-13}
NGC 5669.....	0.789	2.14	2.12	5.74	6.79	2.15×10^{-13}
NGC 5676.....	5.58	10.7	11.7	24.6	25.8	9.33×10^{-13}
NGC 5701.....	0.291	0.701	0.663	2.08	1.73	7.01×10^{-14}
NGC 5713.....	17.5	21.1	28.4	38.6	22.3	1.42×10^{-12}
NGC 5746.....	0.904	3.37	2.93	8.88	14.8	3.70×10^{-13}
NGC 5792.....	7.25	8.89	12.1	18.8	15.9	7.00×10^{-13}

TABLE 7—*Continued*

Galaxy	Flux Densities (Jy) 60 μm (45″)	60 μm (135″)	100 μm (45″)	100 μm (135″)	180 μm (180″)	Total *ISO* Far-Infrared Flux ($W m^{-2}$) (135″)
NGC 5838.....	0.879	1.60	1.73	3.11	0.982	1.06×10^{-13}
NGC 5846.....	0.234	0.935	0.636	2.13	0.939	7.03×10^{-14}
NGC 5850.....	0.585	2.18	1.70	4.89	6.17	1.96×10^{-13}
NGC 5866.....	4.01	5.80	10.4	14.8	12.3	5.20×10^{-13}
NGC 5907.....	2.94	7.06	9.30	25.2	44.1	1.00×10^{-12}
NGC 5985.....	0.473	2.39	1.23	5.14	10.6	2.42×10^{-13}
NGC 6015.....	0.882	3.77	3.44	9.81	13.2	3.84×10^{-13}
NGC 6215.....	16.3	24.9	24.6	44.6	32.3	1.72×10^{-12}
NGC 6217.....	7.75	11.1	11.7	18.4	16.1	7.50×10^{-13}
NGC 6221.....	25.6	37.9	41.7	74.2	59.2	2.81×10^{-12}
NGC 6300.....	7.29	14.0	11.6	28.9	33.8	1.16×10^{-12}
NGC 6340.....	0.497	2.08	0.958	1.79	2.22	1.04×10^{-13}
NGC 6503.....	2.81	7.10	6.57	19.3	22.0	7.14×10^{-13}
NGC 6643.....	7.02	11.0	14.1	24.6	24.7	9.31×10^{-13}
NGC 6744.....	0.789	2.70	1.11	8.89	25.8	4.44×10^{-13}
NGC 6753.....	6.35	9.41	14.7	23.2	19.0	8.19×10^{-13}

with the symbols representing the same quantities as those above, except the variables are *IRAS* flux measurements rather than *ISO* flux measurements. These formulae were derived in Fullmer & Lonsdale (1989).

4.1.2. *Range of Far-Infrared Luminosities*

Figure 5 presents a histogram of the total far-infrared luminosities of the galaxies in the sample as measured by *ISO*. The atlas contains no galaxies with a total far-infrared luminosity larger than 10^{11} $L_{\odot}$ or less than 10^{7} $L_{\odot}$. The upper limit represents the rarity of nearby luminous far-infrared objects, and the lower limit represents the rarity of faint far-infrared objects. The effects of Malmquist bias are also evident in the plot.

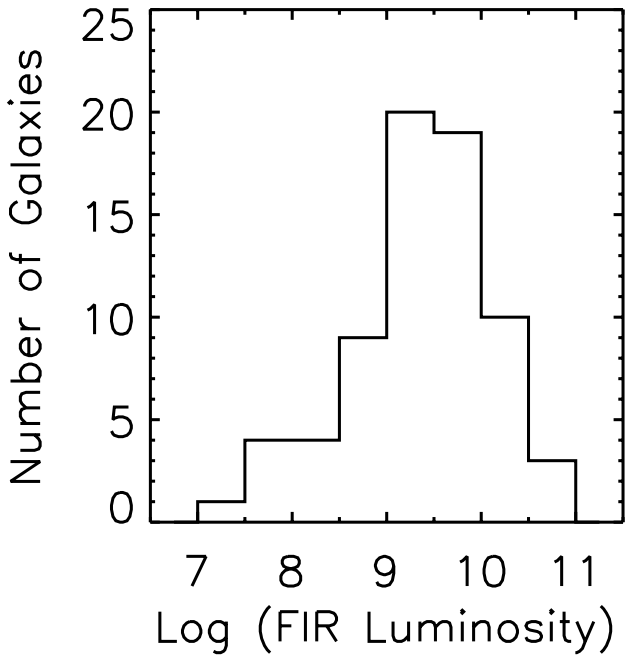

Fig. 5.—Histogram of the logarithm of far-infrared luminosities (in $L_{\odot}$) for the galaxies in the sample. The luminosities were calculated using the *ISO* total far-infrared fluxes in Table 7 and the distances from Tully (1988) (in Table 2).

4.1.3. *Comparisons between ISO and IRAS Photometry*

For a sanity check of the reduction and calibration procedures we compared 60 and 100 μm flux densities from *ISO* and *IRAS*. Measurements from the *IRAS* FSC seemed the best to compare with our data since the *IRAS* measurements were generally on a spatial scale similar to the ISOPHOT 135″ aperture. There are both *IRAS* and *ISO* data for 64 of the 77 atlas galaxies, and these were used for the following comparisons.

Aside from comparing the *ISO* flux densities with *IRAS* FSC flux densities, we also compared the *ISO* measurements to the results reported in Rice et al. (1988), Soifer et al. (1989), and Helou & Walker (1988). These catalogs all contain flux densities that are integrated over the disks of the galaxies, which can exceed 10′ in diameter. In contrast, our data only cover the inner 2.′25 of the galaxies. Therefore, for galaxies that are very extended, we only measure a fraction of the flux densities reported in these other catalogs. Therefore, we will concentrate on the flux densities reported in the FSC, where the apertures are comparable in size to the *ISO* apertures.

We have found that comparisons at 60 μm demonstrate a different effect than comparisons at 100 μm. Therefore, we will deal with each wave band separately.

4.1.3.1. Comparison of 60 μm Data

Both *IRAS* and *ISO* 100 μm flux densities are available for 65 of the 77 atlas galaxies. The results of the 60 μm comparison group into five categories. These categories are based on the ratio of flux densities detected by *IRAS* to the flux densities detected by *ISO* within the 135″ aperture.

For three galaxies, the *IRAS* flux densities are more than twice as large as those detected by *ISO*. This is easily understood, since all three galaxies (NGC 55, NGC 4236, and

TABLE 8
IRAS FSC Far-Infrared Flux Data

Galaxy	*IRAS* Flux Densities (Jy) 60 μm	100 μm	Total *IRAS* Far-Infrared Flux (W m^{-2})
NGC 55	32.0	78.1	2.03×10^{-12}
NGC 289	4.87	15.7	3.56×10^{-13}
NGC 1512.....	3.14	11.0	2.41×10^{-13}
NGC 1569.....	45.4	47.3	2.07×10^{-12}
NGC 3359.....	4.06	14.7	3.17×10^{-13}
NGC 3556.....	26.2	62.0	1.63×10^{-12}
NGC 3898.....	0.416	2.02	3.89×10^{-14}
NGC 4062.....	2.45	10.3	2.09×10^{-13}
NGC 4088.....	19.9	54.5	1.33×10^{-12}
NGC 4096.....	4.55	21.3	4.16×10^{-13}
NGC 4100.....	8.10	21.7	5.37×10^{-13}
NGC 4136.....	1.40	4.32	9.98×10^{-14}
NGC 4157.....	12.0	45.4	9.63×10^{-13}
NGC 4203.....	0.600	2.03	4.51×10^{-14}
NGC 4236.....	3.98	10.0	2.56×10^{-13}
NGC 4244.....	0.507	<4.79	...
NGC 4274.....	4.35	13.3	3.09×10^{-13}
NGC 4314.....	3.79	7.14	2.13×10^{-13}
NGC 4395.....	2.38	6.34	1.57×10^{-13}
NGC 4414.....	26.8	66.1	1.70×10^{-12}
NGC 4448.....	1.42	5.04	1.10×10^{-13}
NGC 4559.....	6.09	22.1	4.77×10^{-13}
NGC 4605.....	11.5	28.8	7.36×10^{-13}
NGC 4618.....	3.82	11.1	2.64×10^{-13}
NGC 4631.....	57.0	124.	3.41×10^{-12}
NGC 4710.....	5.76	13.1	3.53×10^{-13}
NGC 4725.....	...	...	...
NGC 4826.....	34.4	74.5	2.06×10^{-12}
NGC 4945.....	359.	621.	1.95×10^{-11}
NGC 4976.....	...	...	...
NGC 4984.....	11.0	14.4	5.40×10^{-13}
NGC 5005.....	19.7	54.3	1.32×10^{-12}
NGC 5033.....	13.8	43.9	1.00×10^{-12}
NGC 5054.....	11.6	26.2	7.07×10^{-13}
NGC 5055.....	30.2	103.	2.28×10^{-12}
NGC 5068.....	5.05	21.7	4.38×10^{-13}
NGC 5087.....	1.24	2.81	7.56×10^{-14}
NGC 5101.....	0.891	3.57	7.39×10^{-14}
NGC 5102.....	0.802	2.52	5.78×10^{-14}
NGC 5112.....	1.86	6.05	1.37×10^{-13}
NGC 5161.....	2.18	7.24	1.62×10^{-13}
NGC 5170.....	...	...	...
NGC 5204.....	2.33	5.35	1.43×10^{-13}
NGC 5236.....	110.	236.	6.56×10^{-12}
NGC 5247.....	8.07	29.8	6.38×10^{-13}
NGC 5300.....	0.928	3.89	7.92×10^{-14}
NGC 5334.....	0.756	3.32	6.64×10^{-14}
NGC 5364.....	2.27	12.1	2.26×10^{-13}
NGC 5371.....	3.31	14.8	2.94×10^{-13}
NGC 5457.....	...	...	...
NGC 5474.....	1.33	4.80	1.04×10^{-13}
NGC 5556.....	1.37	4.64	1.03×10^{-13}
NGC 5566.....	...	...	...
NGC 5584.....	2.07	<6.05	...
NGC 5585.....	0.991	3.65	7.82×10^{-14}
NGC 5669.....	1.66	5.19	1.19×10^{-13}
NGC 5676.....	9.64	30.7	7.00×10^{-13}
NGC 5701.....	0.272	1.36	2.60×10^{-14}
NGC 5713.....	19.82	36.2	1.10×10^{-12}
NGC 5746.....	1.33	8.88	1.55×10^{-13}
NGC 5792.....	9.17	19.3	5.41×10^{-13}
NGC 5838.....	0.741	1.47	4.26×10^{-14}
NGC 5846.....	...	...	...
NGC 5850.....	0.819	4.22	7.98×10^{-14}
NGC 5866.....	4.88	16.1	3.62×10^{-13}
NGC 5907.....	7.92	38.5	7.42×10^{-13}
NGC 5985.....	1.05	6.36	1.14×10^{-13}
NGC 6015.....	3.40	13.2	2.77×10^{-13}
NGC 6215.....	...	...	...
NGC 6217.....	10.8	19.3	5.96×10^{-13}
NGC 6221.....	...	...	...
NGC 6300.....	14.7	36.0	9.30×10^{-13}
NGC 6340.....	0.202	1.03	1.95×10^{-14}
NGC 6503.....	7.58	25.9	5.73×10^{-13}
NGC 6643.....	9.38	3.07	6.91×10^{-13}
NGC 6744.....	2.21	<30.42	...
NGC 6753.....	9.43	27.4	6.51×10^{-13}

NGC 4395) are highly extended objects with relatively small nuclear emission at all wavelengths. The $4\farcm75 \times 1\farcm5$ *IRAS* detector could have easily detected emission from bright extended regions outside the 2.25 arcmin^2 area observed by *ISO*.

For 20 galaxies, *IRAS* flux densities were up to 30% larger than those from *ISO*. In another 20 galaxies, the *IRAS* flux densities were as much as 25% smaller than those from *ISO*. Since the errors of the ISOPHOT measurements are 20% and the errors of the *IRAS* measurements are typically 5%–15%, this range of differences is within the errors, particularly when the different aperture sizes are taken into account. In other words, 37 of the 64 galaxies have similar flux densities within the errors.

For 12 galaxies *IRAS* measured 50%–75% of the total 60 μm flux density measured by *ISO*. In these cases, simple measurement errors cannot explain the differences between the *IRAS* and *ISO* measurements. The difference might be an effect of the different aperture shapes that *IRAS* and *ISO* have. *IRAS* had a $4\farcm75 \times 1\farcm5$ detector, whereas the C100 array in ISOPHOT covers a $2\farcm25$ square region. If an object were to be scanned by *IRAS* in a direction roughly perpendicular to its major axis, we would expect the FSC calculations to give a flux of roughly half that of our ISOPHOT measurements. This would be particularly true for extended, edge-on galaxies. However, we used XSCANPI to examine how *IRAS* scanned these galaxies, and we found that some of these 12 galaxies were scanned with the *IRAS* detector aligned along the galaxies' major axes. Another explanation for the difference is needed.

For another 10 galaxies *IRAS* measured less than 50% of the total 60 μm flux densities measured by *ISO*. This can no longer be attributed to aperture effects, since such effects could produce errors of approximately 50% at the most.

Examination of the latter 22 galaxies shows that the ratio of the *IRAS* to *ISO* measurements is related to the central concentration of the fluxes. We measure the degree of central concentration at 60 μm by computing the ratio of the flux density for the central source to the total flux density

TABLE 9
COMPARISON OF *IRAS* FLUX DENSITIES TO *ISO* FLUX DENSITIES AT 60 μm

IRAS Flux Densities (% of *ISO* [135″] Flux Densities)	Number of Galaxies	Mean $R(60\ \mu m)$ from *ISO*
> 130	3	0.18 ± 0.12
130–100	20	0.48 ± 0.05
100–75	20	0.46 ± 0.05
75–50	12	0.36 ± 0.05
<50	10	0.28 ± 0.05

TABLE 10
COMPARISON OF *IRAS* FLUX DENSITIES TO *ISO* FLUX DENSITIES AT 100 μm

IRAS Flux Densities (% of *ISO* [135″] Flux Densities)	Number of Galaxies	Mean $R(100\ \mu m)$ from *ISO*
> 200	3	0.17 ± 0.10
200–130	18	0.25 ± 0.02
130–100	20	0.45 ± 0.04
100–75	15	0.39 ± 0.05
<75	5	0.41 ± 0.09

within the 135″ aperture:

$$R(60\ \mu m) = \frac{f_{c,60}}{f_{e,60} + f_{c,60}}. \quad (14)$$

This spatial distribution indicator will be increasingly larger for more centrally concentrated sources. In Table 9 we compare the *IRAS-ISO* flux ratio with the central concentration ratio. The galaxies for which the *ISO* and *IRAS* measurements agree, within the errors, are generally galaxies in which over half of the total *ISO* 60 μm flux density comes from the galaxies' nuclei. The galaxies that are more diffuse and extended are those for which *IRAS* detected less than half of the 60 μm flux density.

These results can be understood from the methods used to measure the *IRAS* and *ISO* fluxes. The *IRAS* 60 μm detector had an aperture $4\farcm75 \times 1\farcm5$ and scanned the sky in a direction perpendicular to this rectangular aperture, whereas the *ISO* detector was $2\farcm25 \times 2\farcm25$. The algorithm used in the FSC to interpret *IRAS* data used a point-source filter and set a baseline for the background. This works very well for compact sources, but if the object is diffuse and extended, the algorithm may set the baseline at the level of the extended emission. For the *ISO* measurements the background flux was measured from a nearby, off-target field. This gives a more reliable measurement of the total flux from diffuse, extended sources as well as from centralized, pointlike sources. In summary, if the 60 μm emission is centrally concentrated, *ISO* and *IRAS* measure approximately the same flux density; if the emission is less concentrated, the *ISO* aperture measures a larger fraction of the flux density.

4.1.3.2. Comparison of 100 μm Data

Both *IRAS* and *ISO* 100 μm flux densities are available for 61 of the 77 atlas galaxies. As above, the flux densities reported in the *IRAS* FSC were compared with the flux densities detected within the 135″ ISOPHOT aperture.

For 20 galaxies, the *IRAS* flux densities are up to 25% larger than the *ISO* flux densities. For an additional 15 galaxies, the *IRAS* flux densities are up to 25% smaller than the *ISO* measurements. Since the errors of the ISOPHOT measurements are 20% and the errors of the *IRAS* measurements were typically between 5% and 15%, the *ISO* and *IRAS* measurements for these 39 galaxies agree within the errors.

For 21 galaxies, the *IRAS* fluxes were more than 25% larger than the *ISO* fluxes. For three of these 21 objects, *IRAS* detected over twice as much flux as *ISO*. These results can be understood since the *IRAS* 100 μm detector covered a much larger area of the sky ($5' \times 3'$) than the *ISO* C100 array ($2\farcm25 \times 2\farcm25$).

For five galaxies, *IRAS* measured less than 75% of the total flux density measured by *ISO*. This is more difficult to understand, since the *IRAS* aperture is plainly larger than the *ISO* aperture. However, the flux densities for each of these five galaxies were also undermeasured by *IRAS* at 60 μm. This suggests that the algorithm for producing the FSC set too high a background flux baseline in measuring the total fluxes from these galaxies at 100 μm.

Again, we examine these results in terms of the central concentration of flux given by the ratio of the flux density from the central source to that for the 135″ aperture:

$$R(100\ \mu m) = \frac{f_{c,100}}{f_{e,100} + f_{c,100}}. \quad (15)$$

Table 10 shows the trend. Unlike the behavior of the 60 μm flux densities, objects with less centrally concentrated 100 μm emission have larger *IRAS* flux density measurements than the corresponding *ISO* measurements. This is consistent with the larger 100 μm *IRAS* aperture compared to *ISO*. For the more compact galaxies, *IRAS* and *ISO* measure similar fluxes at 100 μm, but for less centrally concentrated galaxies *IRAS* measures larger fluxes. In the five cases in which the *IRAS* 100 μm were lower than those from *ISO* and the emission is centrally concentrated, we suspect poor background subtraction in the *IRAS* processing.

4.1.3.3. Comparison of Total Far-Infrared Fluxes

In this comparison the aim is to take advantage of the wider spectral coverage provided by *ISO* and to compare the resulting fluxes over the 40–220 μm band with the fluxes calculated for the 40–120 μm band using *IRAS* FSC data. The measurements in Tables 7 and 8 show that the *ISO* flux measurements, which are calculated for a 40–220 μm wave band, are approximately 30% higher than the *IRAS* FSC flux measurements that are calculated for a 40–120 μm wave band, although the *ISO* fluxes are sometimes equal to the *IRAS* fluxes and sometimes twice the *IRAS* fluxes. This demonstrates that approximately 30% of the far-infrared flux comes from wavelengths longer than 120 μm. The ratio of the *ISO* to *IRAS* fluxes does vary based on how well the 60 and 100 μm flux measurements match. However, even in cases in which the 60 and 100 μm flux measurements match, the difference is still significant.

This demonstrates the importance of measurements beyond 100 μm for determining the total far-infrared fluxes. In our third paper, we will also discuss the necessity of lon-

ger wavelength measurements in calculating dust temperatures.

4.1.3.4. Implications for the Interpretation of *IRAS* Data

The *IRAS* FSC flux densities have been the principal far-infrared data relied upon for many investigations of the far-infrared properties of galaxies, including calculations of luminosity functions and studies of trends in star formation activity. What does the comparison with the pointed *ISO* measurements show about the reliability of the flux densities extracted from the *IRAS* FSC data?

The first conclusion is that for ~60% of the atlas sample the *IRAS* FSC results agree with the pointed *ISO* measurements. Second, when there are discrepancies, in ~40% of the cases, they tend to occur in galaxies where the infrared flux is more spatially extended; for these *IRAS* does not measure the full emission from the galaxy at 60 μm. This effect will be most pronounced for nearby galaxies, such as this sample of bright galaxies.

A third concern is the effect on calculating dust temperatures from *IRAS* FSC data. The *IRAS* 60 and 100 μm detectors, with their different aperture sizes, produce significantly larger ratios of the 60 to 100 μm fluxes than are measured with ISOPHOT for one fixed aperture at both wavelengths. This suggests that far-infrared colors and dust temperatures based on *IRAS* measurements should be treated with some caution, especially for larger, nearby galaxies.

4.2. *Mid-Infrared Photometry*

4.2.1. *Mid-Infrared Flux Densities*

Table 11 gives the mid-infrared flux densities measured with ISOCAM within three circular apertures of diameter 15″, 45″, and 135″. The 45″ and 135″ apertures correspond to the central pixel diameter and full array diameter for the C100 array in ISOPHOT. The 15″ diameter corresponds to a diameter in an integer number of pixels that is wider than 3 times the FWHM of the point-spread function in the ISOCAM images. The fluxes were calculated after subtraction of a background flux measured from two off-target regions within the images. These off-target areas were selected to be in relatively empty regions on opposite sides of each image. Note that the 135″ aperture extends off the image, where we have no measured flux. We have chosen to measure only the flux in the image; we do not extrapolate off the image to estimate the true flux within the 135″ aperture. Also included in Table 11 are 12 μm fluxes from the FSC.

The uncertainties in the fluxes in Table 11 are chiefly due to two sources. First, we estimate that the calibration of the data is good to within 10% (Cesarsky & Blommaert 2000).[18] Second, we have uncertainties in estimating the background flux density that we subtract from the images. This second error is treated like a systematic error over the entire aperture where the flux measurement is made. Note that the error in background measurement leads to a situation in which some sources are detected in 15″ apertures but not in 135″ apertures; the larger aperture adds noise to the data but may contain no additional signal, leading to the decrease in the signal-to-noise ratio of the measurements.

[18] See http://www.iso.vilspa.esa.es/manuals/CAM/accuracies/CAM_accur.

4.2.2. *Comparison of ISO and IRAS Mid-Infrared Data*

As above, we compared the flux densities within a 135″ aperture to the flux densities reported in the *IRAS* FSC. The FSC reports 12 μm measurements for 47 of the atlas galaxies, as well as upper limits for 20 additional galaxies. Because the circular aperture we used differs from the 4.45×0.76 arcmin^2 *IRAS* aperture, the measurements may not necessarily agree well unless the sources are relatively compact. We also looked at *IRAS* data from catalogs that integrated fluxes over the disks of the galaxies (Rice et al. 1988; Soifer et al. 1989; Helou & Walker 1988). However, as with the 60 and 100 μm flux densities, the 12 μm flux densities from these catalogs were much higher than our measurements. We therefore concentrated on comparing our data with the FSC.

For 25 of the 47 galaxies, the *IRAS* and *ISO* fluxes agree within the errors. For the 20 galaxies in which the FSC lists an upper limit, the *ISO* measurements are either similar to or less than the quoted FSC upper limits.

For nine galaxies, the *IRAS* measurements are larger than the *ISO* measurements. This could be because some of the mid-infrared emission from these galaxies was covered by the *IRAS* aperture but not the ISOCAM array. Most of these galaxies have very large optical diameters, and the mid-infrared emission from some of these galaxies clearly extends beyond the regions in the ISOCAM images (as for NGC 5055 and NGC 5247).

For 13 galaxies, the *IRAS* measurements are smaller than the *ISO* measurements. This could be the result of differences in the aperture sizes. If the rectangular *IRAS* aperture were oriented perpendicularly to the major axis of the galaxy but parallel to the rectangular *ISO* image, more flux would have fallen into the *ISO* image than into the *IRAS* aperture. All 13 of these galaxies have significant emission from regions outside their nuclei that falls mostly within the ISOCAM image, so this explanation is plausible.

Despite the different aperture sizes, there is generally very good agreement in the 12 μm measurements for galaxies that were detected by *IRAS* and *ISO*. The major difference is that *IRAS* reliably detected only about half the sample.

4.3. *JHK Photometry*

The *JHK* photometry is given in Table 12 for all galaxies with a declination north of -50°. The flux densities are tabulated for three apertures of diameter 15″, 45″, and 135″. These apertures were selected to correspond to the apertures where we calculated flux densities from ISOPHOT and ISOCAM.

5. THE MORPHOLOGY OF MID-INFRARED EMISSION

The 12 μm images (Figs. 6–80) show the distribution of hot dust emission and polycyclic aromatic hydrocarbon (PAH) emission from these galaxies. In cases in which the emission is faint, particularly compared to the *K*-band emission, the emission is probably dominated by the PAH lines. In cases in which the emission is strong, the emission is more likely to be dominated by hot dust heated by star formation regions. The morphologies vary radically among the galaxies in this sample, with the most obvious differences seen when comparing early- and late-type galaxies.

TABLE 11

OBSERVED MID-INFRARED FLUX DENSITIES

GALAXY	*ISO* 12 μm FLUX DENSITIES (mJy)			*IRAS* 12 μm FLUX DENSITIES (mJy)
	15″	45″	135″	
NGC 0055.....	4.03 ± 0.49	15.8 ± 3.0	72. ± 19.	575. ± 46.
NGC 0289.....	44.2 ± 4.5	176. ± 20.	329. ± 72.	277. ± 33.
NGC 1512.....	51.4 ± 5.2	114. ± 13.	146. ± 40.	224. ± 20.
NGC 1569.....	224. ± 22.	550. ± 56.	850. ± 120.	794. ± 48.
NGC 3359.....	19.8 ± 2.0	82.9 ± 9.2	213. ± 36.	169. ± 24.
NGC 3556.....	113. ± 11.	525. ± 53.	1140. ± 120.	908. ± 45.
NGC 3898.....	15.1 ± 1.5	41.6 ± 4.4	81. ± 13.	109. ± 20.
NGC 4062.....	13.8 ± 1.4	94.4 ± 9.5	298. ± 30.	304. ± 30.
NGC 4088.....	117. ± 12.	404. ± 41.	1490. ± 150.	884. ± 53.
NGC 4096.....	51.6 ± 5.2	204. ± 20.	547. ± 55.	299. ± 27.
NGC 4100.....	126. ± 13.	275. ± 28.	562. ± 60.	500. ± 30.
NGC 4136.....	2.44 ± 0.43	17.6 ± 3.6	78. ± 24.	<67.
NGC 4157.....	85.7 ± 8.6	416. ± 42.	1180. ± 120.	679. ± 95.
NGC 4203.....	31.1 ± 3.1	55.7 ± 5.7	62. ± 11.	83. ± 28.
NGC 4236.....	0.66 ± 0.27	3.6 ± 2.4	4. ± 17.	110. ± 17.
NGC 4244.....	3.99 ± 0.53	20.7 ± 3.8	59. ± 24.	<117.
NGC 4274.....	72.0 ± 7.2	151. ± 15.	282. ± 28.	312. ± 41.
NGC 4314.....	55.9 ± 5.6	125. ± 13.	161. ± 25.	165. ± 46.
NGC 4395.....	7.58 ± 0.86	17.6 ± 4.1	32. ± 25.	<129.
NGC 4414.....	94.7 ± 9.5	810. ± 81.	1970. ± 200.	1920. ± 150.
NGC 4448.....	21.8 ± 2.2	70.2 ± 7.2	146. ± 19.	<266.
NGC 4559.....	20.3 ± 2.0	113. ± 11.	373. ± 37.	387. ± 31.
NGC 4605.....	22.9 ± 2.3	149. ± 15.	454. ± 47.	501. ± 45.
NGC 4618.....	7.12 ± 0.81	32.8 ± 4.8	133. ± 29.	<139.
NGC 4631.....	226. ± 23.	941. ± 94.	2340 ± 240.	2410. ± 190.
NGC 4710.....	78.7 ± 7.9	165. ± 18.	202. ± 46.	<256.
NGC 4725.....	29.7 ± 3.0	63.5 ± 7.8	73. ± 33.	...
NGC 4826.....	258. ± 26.	992. ± 100.	1520. ± 170.	1910. ± 130.
NGC 4945.....	1190. ± 120.	2910. ± 290.	5440. ± 540.	3950. ± 200.
NGC 4976.....	20.5 ± 2.1	47.5 ± 5.7	58. ± 23.	...
NGC 4984.....	244. ± 24.	400. ± 40.	458. ± 46.	719. ± 58.
NGC 5005.....	148. ± 15.	469. ± 47.	1020. ± 100.	951. ± 57.
NGC 5033.....	128. ± 13.	560. ± 56.	1100. ± 110.	945. ± 47.
NGC 5054.....	178. ± 18.	379. ± 38.	689. ± 79.	755. ± 68.
NGC 5055.....	109. ± 11.	571. ± 60.	1570. ± 210.	1860. ± 150.
NGC 5068.....	7.9 ± 1.1	49.7 ± 8.2	210. ± 51.	222. ± 58.
NGC 5087.....	36.6 ± 3.7	61.8 ± 8.6	75. ± 44.	<128.
NGC 5101.....	23.7 ± 2.4	53.6 ± 5.4	98. ± 10.	115. ± 26.
NGC 5102.....	16.7 ± 1.7	36.2 ± 3.7	42.0 ± 6.9	<154.
NGC 5112.....	6.46 ± 0.65	29.8 ± 3.0	82.5 ± 8.2	<160.
NGC 5161.....	22.1 ± 2.4	92. ± 13.	219. ± 70.	182. ± 35.
NGC 5170.....	10.4 ± 1.1	44.3 ± 6.0	120. ± 32.	...
NGC 5204.....	2.74 ± 0.35	17.4 ± 2.6	48. ± 15.	<88.
NGC 5236.....	1580. ± 160.	3630. ± 360.	5490. ± 560.	4830. ± 390.
NGC 5247.....	71.0 ± 7.1	263. ± 26.	465. ± 51.	541. ± 38.
NGC 5300.....	4.09 ± 0.61	18.4 ± 4.5	75. ± 30.	<164.
NGC 5334.....	1.92 ± 0.42	12.0 ± 3.6	37. ± 25.	<156.
NGC 5364.....	4.44 ± 0.59	30.4 ± 4.7	175. ± 31.	<187.
NGC 5371.....	6.76 ± 0.70	36.4 ± 4.0	219. ± 25.	208. ± 29.
NGC 5457.....	51.0 ± 5.1	116. ± 12.	259. ± 38.	...
NGC 5474.....	2.59 ± 0.31	11.4 ± 1.9	13. ± 11.	<88.
NGC 5556.....	6.49 ± 0.81	39.7 ± 5.9	171. ± 34.	88. ± 26.
NGC 5566.....	26.5 ± 2.8	84. ± 12.	182. ± 59.	...
NGC 5584.....	6.56 ± 0.68	31.3 ± 3.6	135. ± 18.	<182.
NGC 5585.....	3.42 ± 0.36	13.2 ± 1.7	39.2 ± 8.3	<78.
NGC 5669.....	10.6 ± 1.2	45.3 ± 6.1	141. ± 33.	92. ± 26.
NGC 5676.....	53.3 ± 5.3	366. ± 37.	885. ± 89.	713. ± 57.
NGC 5701.....	5.62 ± 0.75	12.8 ± 4.7	20. ± 33.	<84.
NGC 5713.....	225. ± 23.	738. ± 74.	1090. ± 110.	1100. ± 77.
NGC 5746.....	26.4 ± 2.7	107. ± 11.	309. ± 39.	144. ± 27.
NGC 5792.....	136. ± 14.	302. ± 31.	495. ± 62.	828. ± 74.
NGC 5838.....	26.2 ± 2.7	50.3 ± 6.3	75. ± 29.	<191.

TABLE 11—*Continued*

Galaxy	*ISO* 12 μm Flux Densities (mJy)			*IRAS* 12 μm Flux Densities (mJy)
	15″	45″	135″	
NGC 5846.....	11.3 ± 1.2	34.5 ± 4.5	53. ± 22.	...
NGC 5850.....	12.5 ± 1.3	26.9 ± 3.0	53. ± 11.	93. ± 22.
NGC 5866.....	52.9 ± 5.3	162. ± 16.	227. ± 28.	255. ± 18.
NGC 5907.....	68.5 ± 6.9	287. ± 29.	722. ± 72.	<728.
NGC 5985.....	3.30 ± 0.63	23.3 ± 5.4	154. ± 38.	135. ± 19.
NGC 6015.....	16.3 ± 1.7	95. ± 11.	345. ± 53.	250. ± 25.
NGC 6215.....	177. ± 18.	671. ± 67.	1420. ± 140.	...
NGC 6217.....	159. ± 16.	280. ± 28.	521. ± 52.	506. ± 20.
NGC 6221.....	455. ± 45.	929. ± 93.	2160. ± 220.	...
NGC 6300.....	216. ± 22.	362. ± 36.	974. ± 100.	927. ± 56.
NGC 6340.....	8.51 ± 0.86	24.3 ± 2.7	23.5 ± 8.1	<98.
NGC 6503.....	23.9 ± 2.4	208. ± 21.	576. ± 62.	446. ± 22.
NGC 6643.....	53.0 ± 5.3	360. ± 36.	873. ± 89.	806. ± 48.
NGC 6744.....	...	...	...	179. ± 14.
NGC 6753.....	...	...	...	600. ± 36.

5.1. *S0 Galaxies*

Almost all of the mid-infrared emission from S0 galaxies (as well as the elliptical galaxies accidentally included in this sample) comes from the galaxies' nuclei. NGC 4203, NGC 4984, NGC 5087, NGC 5102, and NGC 5838 all have no well-defined mid-infrared structures outside of their nuclei. Similarly, the image of the elliptical galaxy NGC 4976 also shows emission only from the nucleus. Two points of mid-infrared emission are visible in the image of the elliptical NGC 5846; one belongs to the galaxy itself, while the other belongs to a nearby (apparently interacting) elliptical galaxy, NGC 5846A. Only two S0 galaxies, NGC 4710 and NGC 5866, show any major structures outside of their nuclei. Both have extended, edge-on disks. However, since these galaxies are edge-on, they may not have been classified correctly and may be early-type spiral galaxies.

Because S0 and elliptical galaxies are gas-poor, they should neither have much ongoing star formation activity to heat very small grains nor contain many PAHs to produce PAH emission, particularly in the disks. This is clearly what these images show.

5.2. *S0/Sa–Sab Galaxies*

As with the S0 galaxies, most of the mid-infrared emission in S0/Sa, Sa, and Sab galaxies comes from the galaxies' nuclei. In some cases, such as NGC 5101 and NGC 4725, the nucleus is the only source of mid-infrared emission. In all other cases the galaxies show some extended emission. Two galaxies, NGC 6340 and NGC 5701, have small knots of emission outside the nuclei. NGC 3898 has a diffuse disk of mid-infrared emission. NGC 5566 exhibits 12 μm arm fragments. NGC 4826, an unusual galaxy with a counterrotating disk of gas and a leading spiral arm (Braun, Walterbos, & Kennicutt 1992), has a bright arm extending north from the nucleus. Some of these galaxies, however, have ringlike structures. In NGC 1512 and NGC 4314, these ring structures are close to the nucleus, within the inner Lindblad resonances of the galaxies' primary bars. In NGC 4274 and NGC 4448, these rings are located outside the outer Lindblad resonances.

Despite the presence of extended structures in early-type galaxies, the nuclei of early-type spiral galaxies are the dominant sources of infrared emission. This is likely to be the consequence of the central concentration of molecular gas in early-type galaxies. Young et al. (1995) found that the isophotal diameter of molecular gas in early-type galaxies is significantly smaller than the optical diameter, indicating that molecular gas is concentrated near the centers of early-type galaxies. The dust, which follows the gas, will also be centrally concentrated.

We find rings of infrared emission only in early-type galaxies, with NGC 5746, a nearly edge-on Sb galaxy, as the latest type galaxy with a dust ring. The galaxies are barred in all cases in which we find 12 μm rings except NGC 5746, although NGC 5746, which has a peanut-shaped nucleus, may also be a barred galaxy (Kuijken & Merrifield 1995). This suggests that the bars are responsible for producing the rings, which are only stable in early-type spiral galaxies.

5.3. *Sb–Scd Galaxies*

In contrast with early-type spiral galaxies, infrared emission is much more prominent in the disks of late-type galaxies. In many cases, the 12 μm structures follow the spiral structure of the galaxies, which suggests that the spiral arms may be triggering star formation activity that heats the dust. The shapes of the 12 μm structures along the spiral arms can be continuous, fragmentary, or knotted. Galaxies such as NGC 289, NGC 5005, and NGC 5054 exhibit smooth, continuous mid-infrared emission along the spiral arms. Other galaxies, such as NGC 4088, NGC 4096, NGC 4605, and NGC 6015, have very knotted 12 μm structures. Most galaxies, however, have emission structures that are a combination of knots and spiral arm fragments. The major exceptions are NGC 4136 and NGC 5334, where no structure was detected.

The fact that the disks of late-type spiral galaxies are so much more prominent at 12 μm than those of early-type spi-

TABLE 12

OBSERVED *JHK* FLUX DENSITIES

	J BAND (mJy)			*H* BAND (mJy)			*K* BAND (mJy)		
GALAXY	15″	45″	135″	15″	45″	135″	15″	45″	135″
NGC 55	...	...	...	...	...	...	...	...	...
NGC 289	110.	337.	...	121.	309.	...	107.	266.	...
NGC 1512.....	95.0	202.	...	99.5	226.	...	139.	315.	...
NGC 1569.....	123.	479.	...	268.	986.	...	78.0	309.	...
NGC 3359.....	36.0	147.	566.	25.0	95.9	327.	16.3	64.6	239.
NGC 3556.....	38.0	170.	714.	57.7	264.	1140.	44.1	190.	734.
NGC 3898.....	170.	342.	625.	220.	442.	875.	157.	313.	642.
NGC 4062.....	28.2	131.	449.	34.7	156.	506.	25.6	116.	388.
NGC 4088.....	47.0	157.	417.	68.8	226.	638.	78.0	245.	677.
NGC 4096.....	39.8	146.	440.	53.5	194.	622.	39.2	141.	448.
NGC 4100.....	47.7	154.	478.	66.3	205.	635.	49.5	143.	422.
NGC 4136.....	12.3	54.2	210.	13.9	59.4	210.	10.5	52.4	217.
NGC 4157.....	66.5	221.	552.	107.	353.	922.	86.7	283.	718.
NGC 4203.....	191.	381.	729.	254.	501.	1010.	184.	365.	808.
NGC 4236.....	8.32	34.3	203.	9.86	45.4	287.	8.56	38.0	215.
NGC 4244.....	12.7	72.9	273.	13.7	79.4	299.	18.4	105.	389.
NGC 4274.....	114.	329.	822.	151.	416.	1060.	119.	313.	785.
NGC 4314.....	110.	307.	650.	144.	393.	826.	99.2	271.	619.
NGC 4395.....	2.07	12.6	77.3	4.78	29.4	188.	3.99	22.5	137.
NGC 4414.....	180.	507.	1040.	194.	556.	1120.	123.	375.	889.
NGC 4448.....	88.6	260.	552.	91.3	271.	621.	78.3	234.	563.
NGC 4559.....	21.6	111.	421.	28.9	151.	617.	22.3	115.	471.
NGC 4605.....	26.9	155.	517.	34.7	198.	695.	28.5	166.	617.
NGC 4618.....	15.2	75.8	252.	17.3	89.4	299.	12.5	64.9	240.
NGC 4631.....	41.4	218.	832.	77.5	362.	1220.	72.6	310.	981.
NGC 4710.....	87.7	254.	581.	108.	292.	6260.	98.4	256.	576.
NGC 4725.....	186.	403.	694.	198.	429.	748.	118.	258.	479.
NGC 4826.....	382.	1020.	2910.	530.	1390.	3720.	462.	1220.	3340.
NGC 4945.....	82.7	502.	1690.	215.	891.	2500.	320.	922.	2120.
NGC 4976.....	250.	556.	1120.	333.	751.	1700.	263.	582.	1270.
NGC 4984.....	163.	321.	552.	229.	443.	811.	176.	331.	639.
NGC 5005.....	265.	655.	1300.	324.	782.	1630.	234.	549.	1200.
NGC 5033.....	174.	421.	817.	235.	566.	1100.	195.	475.	1000.
NGC 5054.....	80.8	202.	616.	101.	236.	653.	81.0	187.	557.
NGC 5055.....	220.	665.	1860.	296.	880.	2470.	253.	753.	2180.
NGC 5068.....	16.0	83.2	307.	...	...	...	14.1	75.5	309.
NGC 5087.....	197.	373.	566.	272.	508.	841.	206.	378.	644.
NGC 5101.....	161.	401.	793.	274.	693.	1530.	143.	358.	796.
NGC 5102.....	151.	354.	591.	185.	449.	882.	141.	340.	723.
NGC 5112.....	8.47	39.5	164.	9.86	45.8	192.	6.60	29.4	114.
NGC 5161.....	27.9	109.	295.	35.8	145.	465.	25.9	103.	305.
NGC 5170.....	92.6	250.	547.	145.	390.	824.	84.0	229.	511.
NGC 5204.....	8.67	52.2	212.	10.2	63.5	289.	6.80	42.6	193.
NGC 5236.....	424.	1000.	1910.	546.	1310.	2530.	471.	1100.	2090.
NGC 5247.....	35.2	111.	342.	43.7	136.	410.	32.8	102.	318.
NGC 5300.....	9.26	45.6	186.	11.5	56.5	239.	13.4	69.1	320.
NGC 5334.....	6.60	36.0	178.	8.39	50.3	278.	4.92	27.4	125.
NGC 5364.....	24.3	101.	339.	33.9	136.	431.	22.6	96.0	359.
NGC 5371.....	63.5	150.	423.	70.5	165.	483.	59.5	148.	503.
NGC 5457.....	44.3	156.	472.	50.9	177.	573.	40.7	137.	438.
NGC 5474.....	11.6	53.7	198.	12.7	58.8	228.	8.83	44.0	209.
NGC 5556.....	7.19	47.7	187.	10.1	68.2	318.	7.53	49.0	234.
NGC 5566.....	219.	460.	763.	388.	822.	1440.	191.	422.	888.
NGC 5584.....	7.98	38.1	190.	10.1	48.3	240.	8.23	41.8	221.
NGC 5585.....	8.17	42.8	212.	9.31	47.2	224.	6.85	32.9	136.
NGC 5669.....	9.95	39.7	141.	13.6	57.2	247.	10.1	40.7	169.
NGC 5676.....	56.6	196.	507.	97.7	328.	845.	63.8	214.	540.
NGC 5701.....	81.7	207.	375.	101.	258.	488.	70.2	180.	354.
NGC 5713.....	49.7	177.	406.	64.0	214.	453.	49.4	153.	271.
NGC 5746.....	129.	390.	783.	178.	525.	1050.	153.	454.	948.
NGC 5792.....	109.	312.	1910.	200.	530.	3410.	101.	258.	1820.
NGC 5838.....	182.	357.	591.	219.	435.	859.	182.	350.	614.

TABLE 12—*Continued*

Galaxy	*J* Band (mJy)			*H* Band (mJy)			*K* Band (mJy)		
	15″	45″	135″	15″	45″	135″	15″	45″	135″
NGC 5846.....	140.	421.	965.	163.	482.	1160.	142.	421.	1020.
NGC 5850.....	75.8	172.	418.	95.0	212.	478.	74.2	169.	456.
NGC 5866.....	176.	527.	1030.	253.	706.	1400.	272.	720.	1420.
NGC 5907.....	67.0	240.	630.	106.	367.	950.	117.	391.	1030.
NGC 5985.....	31.0	108.	400.	49.8	179.	718.	30.9	110.	413.
NGC 6015.....	21.3	103.	349.	26.2	129.	437.	20.6	104.	410.
NGC 6215.....	...	...	...	...	...	...	...	...	...
NGC 6217.....	48.6	122.	346.	89.6	220.	619.	52.8	125.	364.
NGC 6221.....	...	...	...	...	...	...	...	...	...
NGC 6300.....	...	...	...	...	...	...	...	...	...
NGC 6340.....	90.6	223.	556.	103.	257.	669.	71.2	174.	434.
NGC 6503.....	51.7	263.	778.	96.8	494.	1520.	51.9	261.	766.
NGC 6643.....	31.7	149.	444.	43.6	198.	583.	38.6	177.	560.
NGC 6744.....	...	...	...	...	...	...	...	...	...
NGC 6753.....	...	...	...	...	...	...	...	...	...

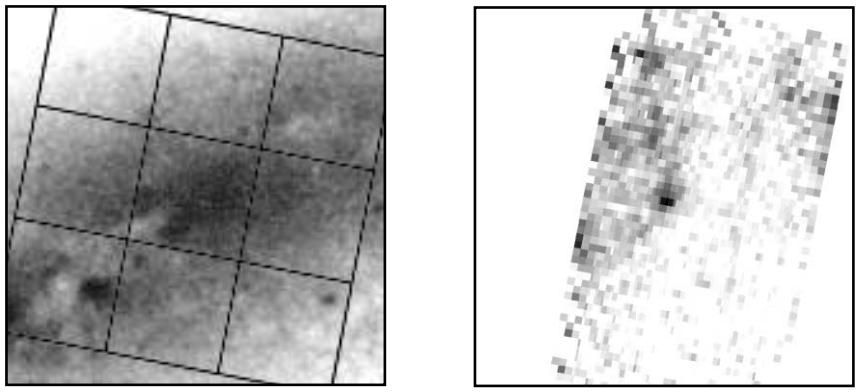

Fig. 6.—NGC 55 [SB(s)m]. The format for Figs. 7–80 follows the format for this image. The left panel is the *K*-band image (except for this galaxy and three others, where no *K*-band data are available and a second-generation red image from the STScI Digitized Sky Survey has been substituted), and the right panel is the 12 μm ISOCAM image. Each box is 150″ × 150″. North is up and east is to the left in each image. In each *K*-band image, the overlay shows the approximate location, orientation, and angular coverage of the ISOPHOT C100 array. The morphological classification in the captions for each image is from RC3.

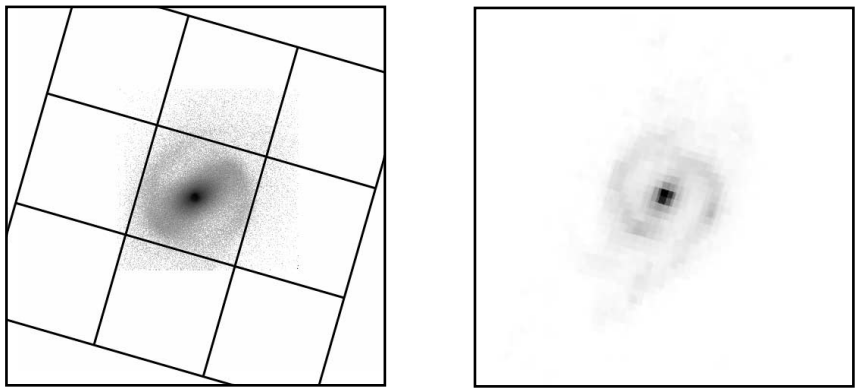

Fig. 7.—NGC 289 [SB(rs)bc]

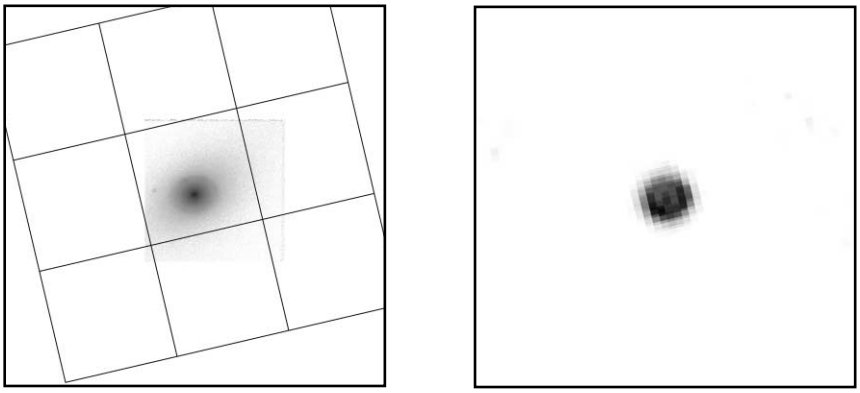

FIG. 8.—NGC 1512 [SB(r)a]

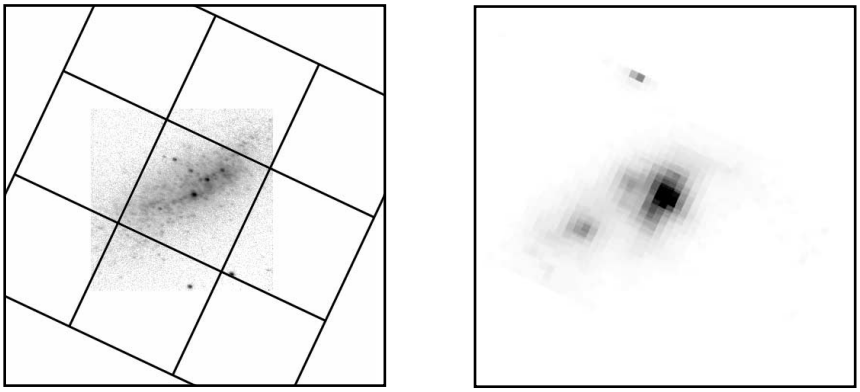

FIG. 9.—NGC 1569 (IBm)

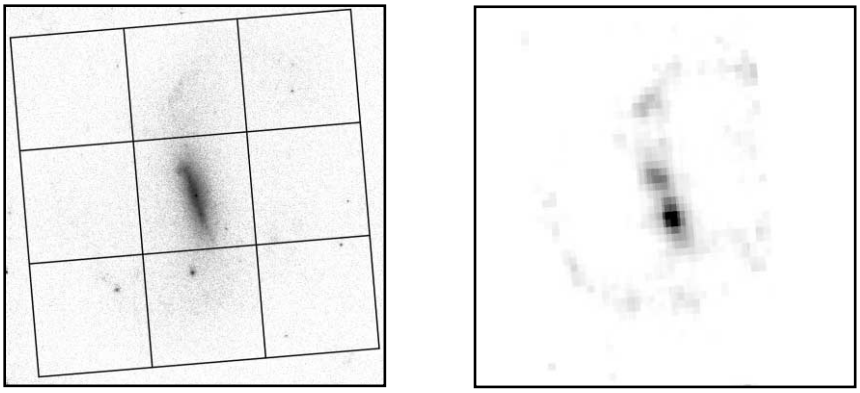

FIG. 10.—NGC 3359 [SB(rs)c]

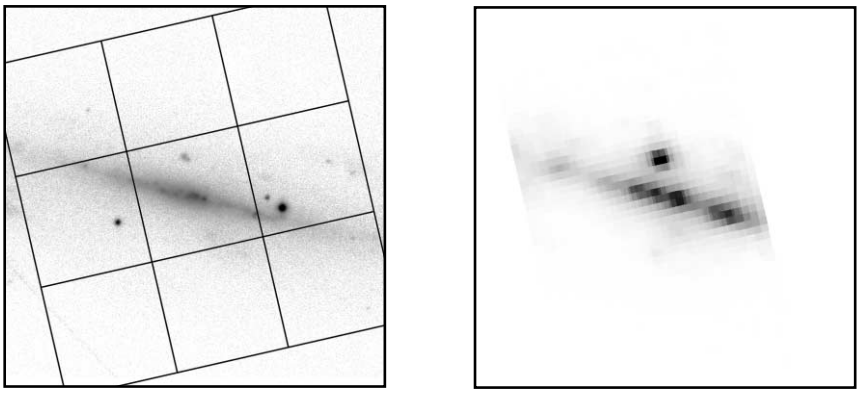

FIG. 11.—NGC 3556 [SB(s)cd]

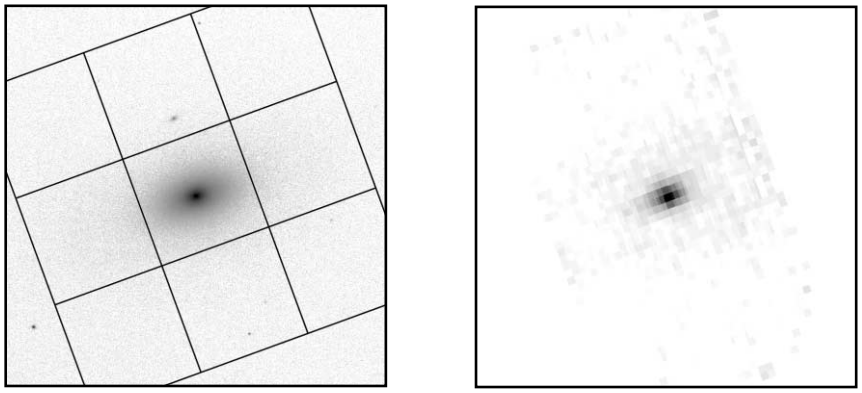

FIG. 12.—NGC 3898 [SA(s)ab]

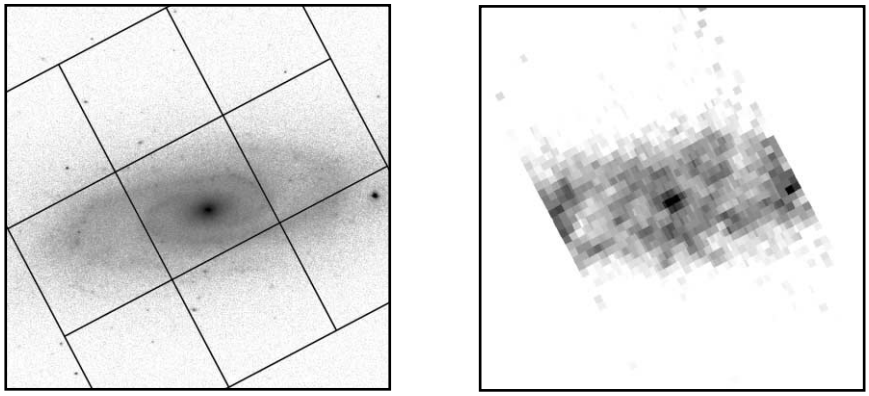

FIG. 13.—NGC 4062 [SA(s)c]

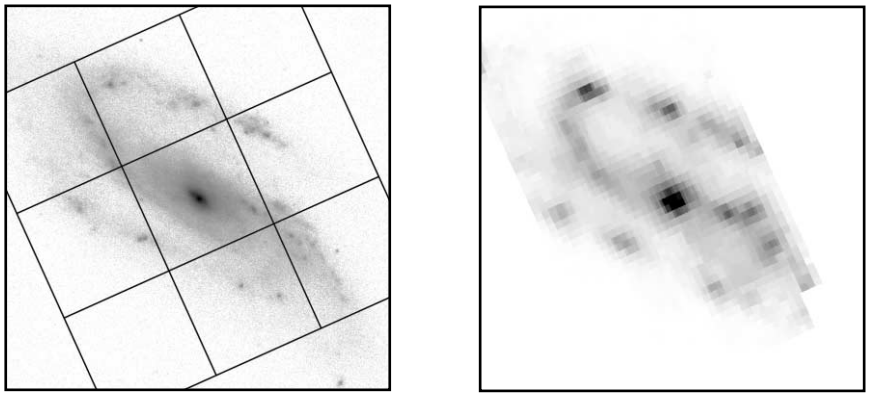

FIG. 14.—NGC 4088 [SAB(rs)bc]

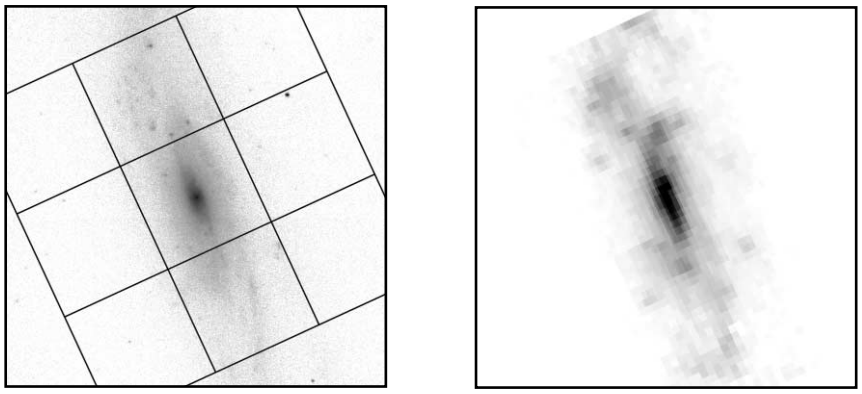

FIG. 15.—NGC 4096 [SAB(rs)c]

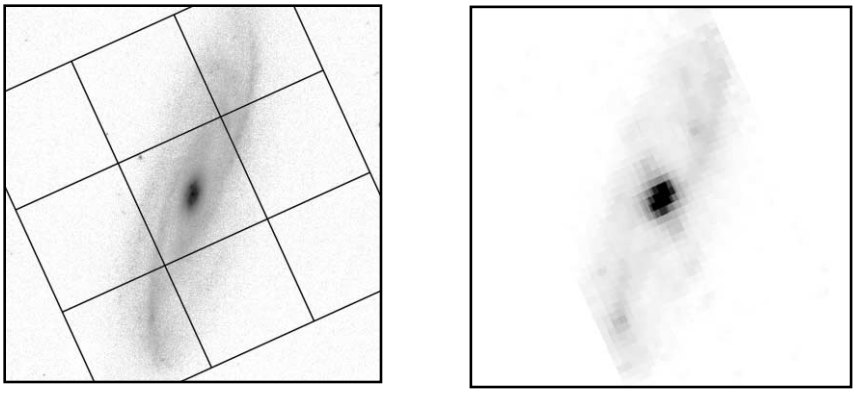

FIG. 16.—NGC 4100 [PSA(rs)bc]

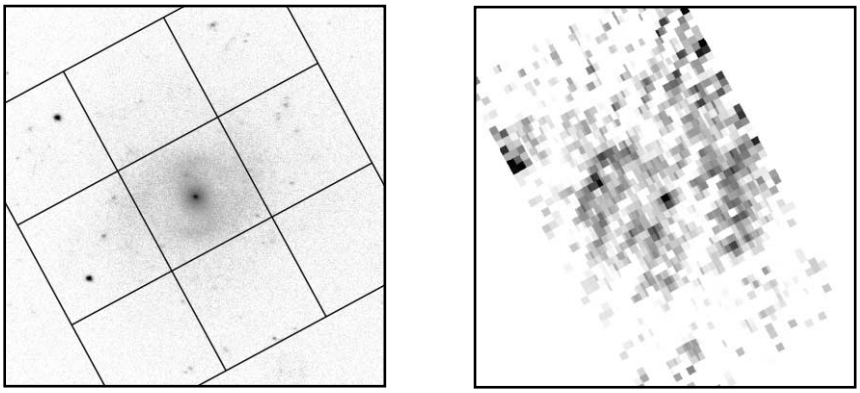

FIG. 17.—NGC 4136 [SAB(r)c]

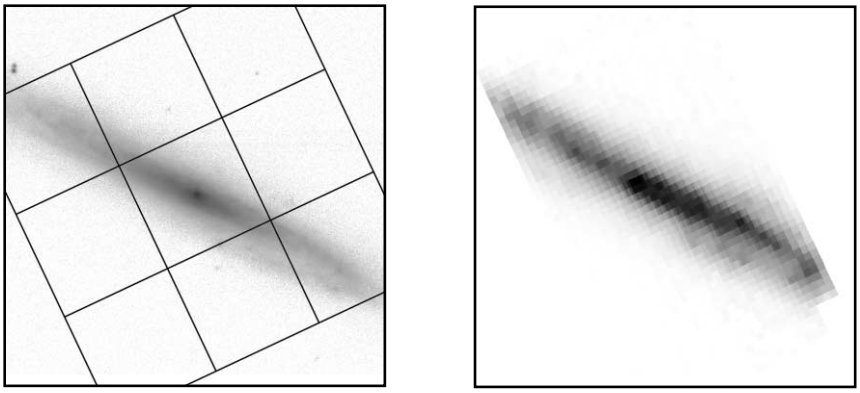

FIG. 18.—NGC 4157 [SAB(s)b]

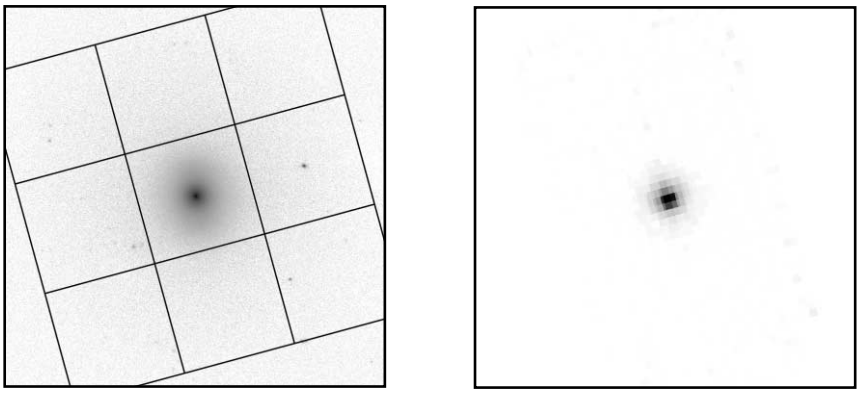

FIG. 19.—NGC 4203 (SAB0)

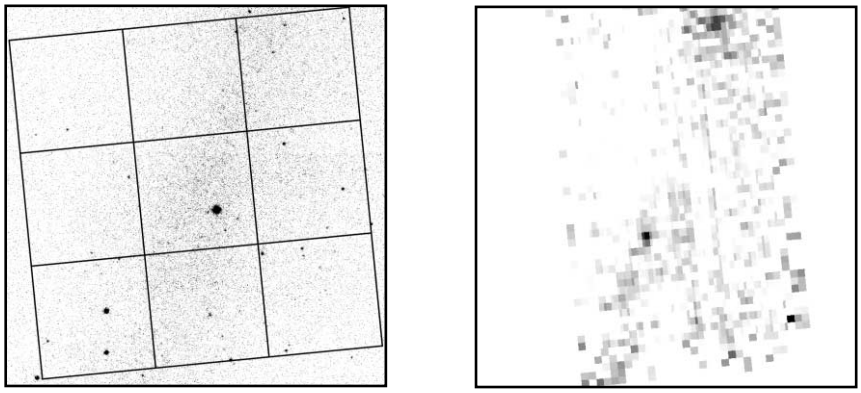

FIG. 20.—NGC 4236 [SB(s)dm]

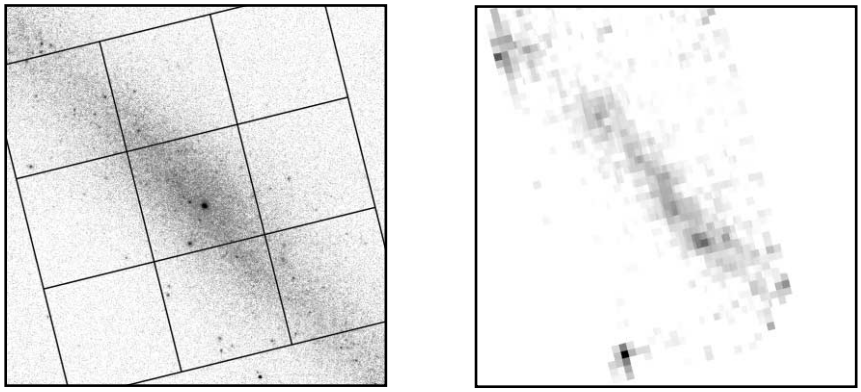

FIG. 21.—NGC 4244 [SA(s)cd]

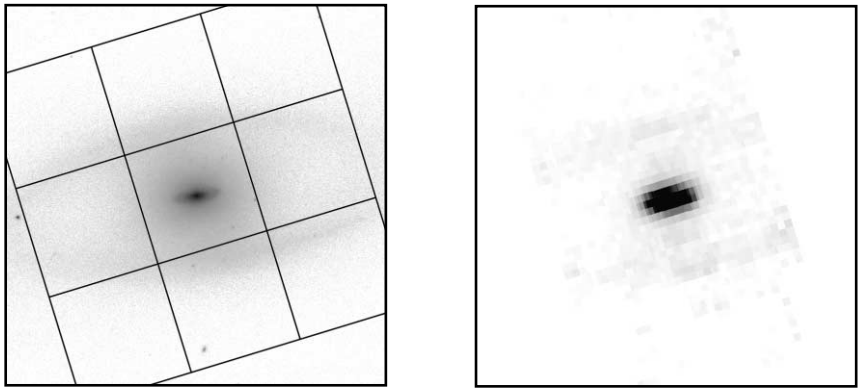

FIG. 22.—NGC 4274 [RSB(r)ab]

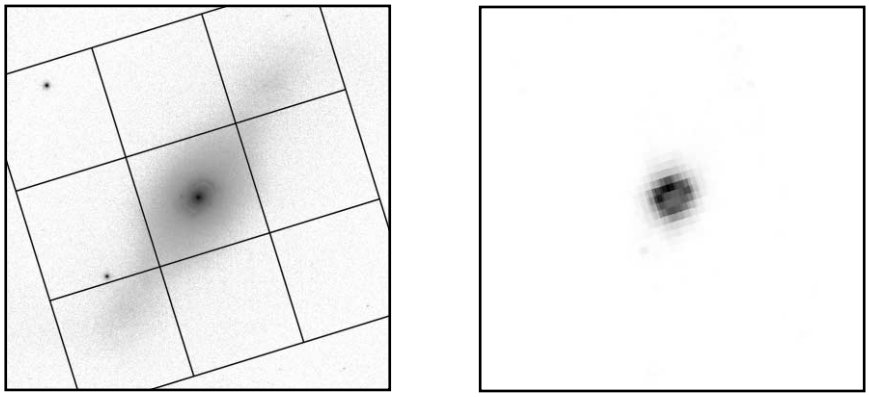

FIG. 23.—NGC 4314 [SB(rs)a]

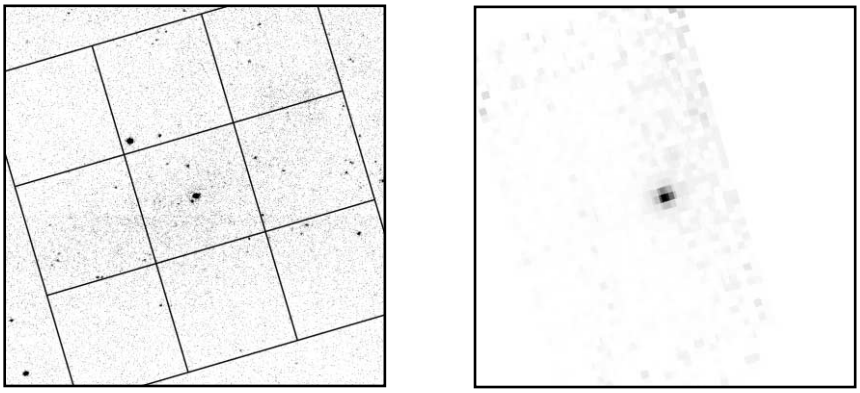

FIG. 24.—NGC 4395 [SA(s)m]

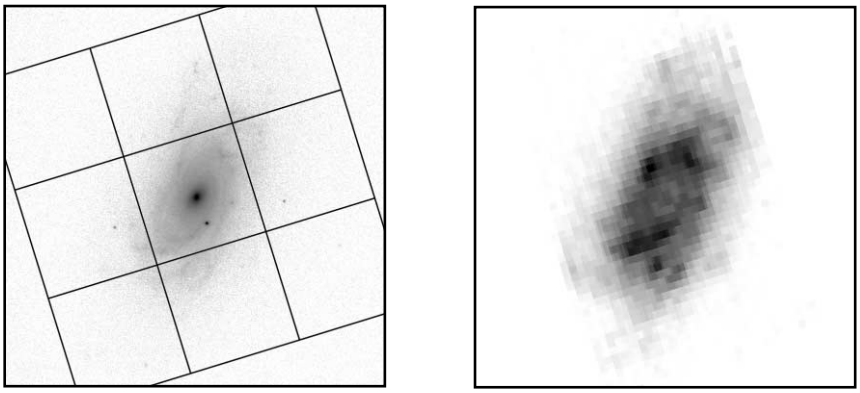

FIG. 25.—NGC 4414 [SA(rs)c]

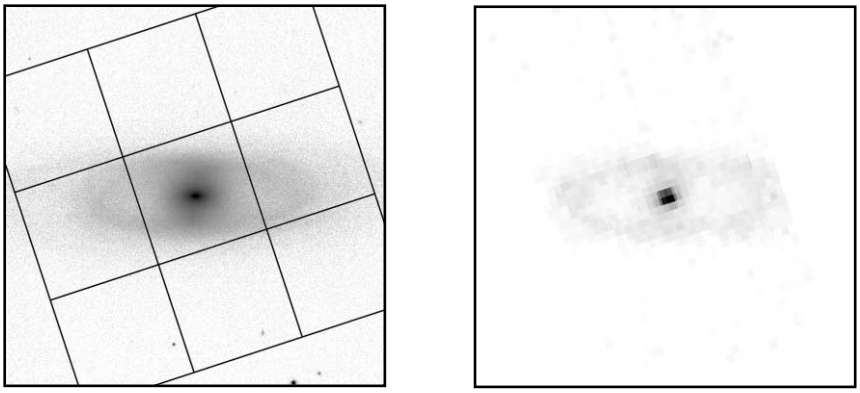

FIG. 26.—NGC 4448 [SB(r)ab]

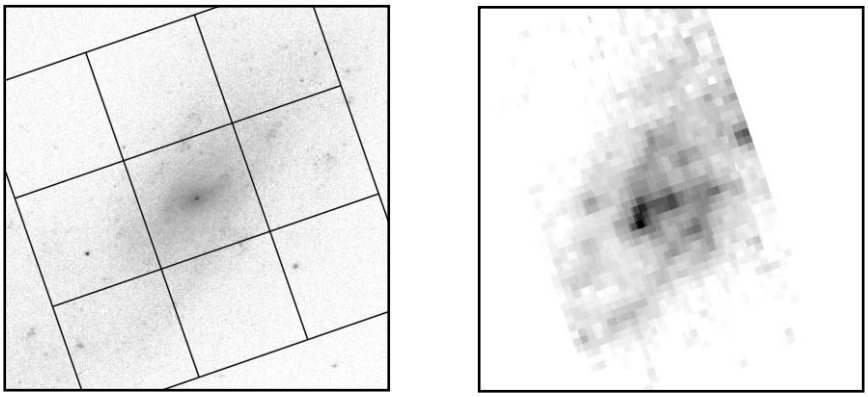

FIG. 27.—NGC 4559 [SAB(rs)cd]

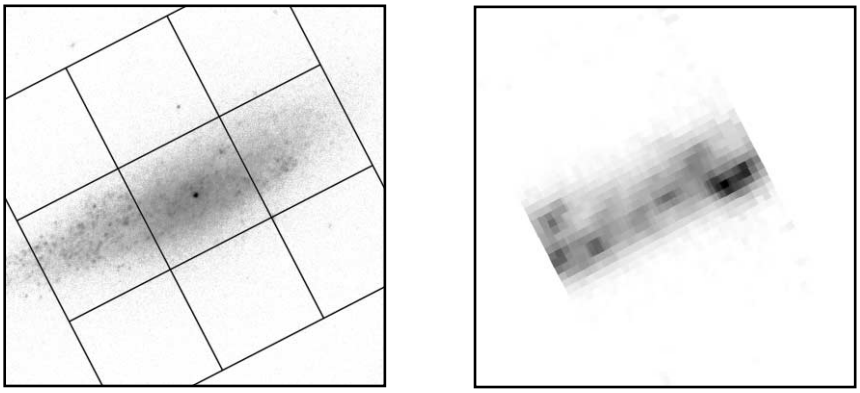

FIG. 28.—NGC 4605 [SB(s)c pec]

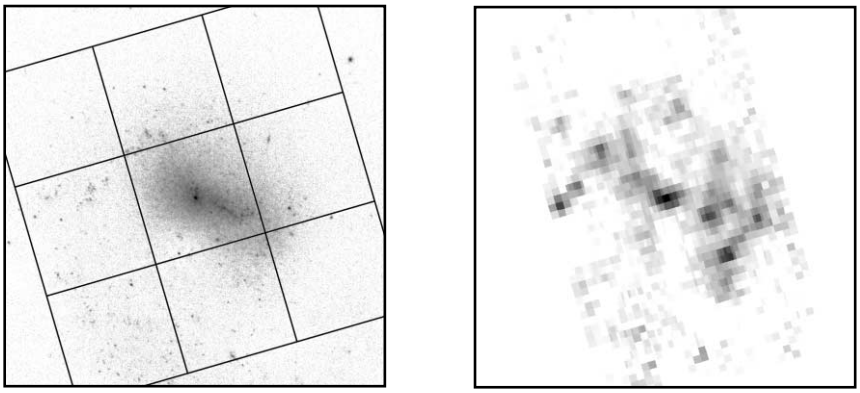

FIG. 29.—NGC 4618 [SB(rs)m]

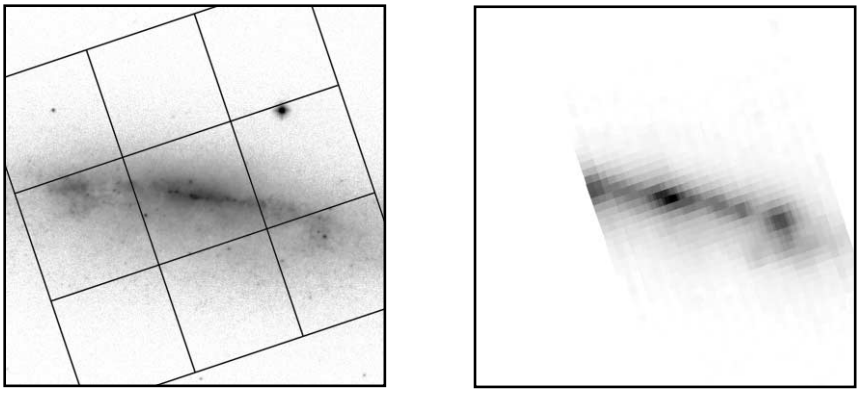

FIG. 30.—NGC 4631 [SB(s)d]

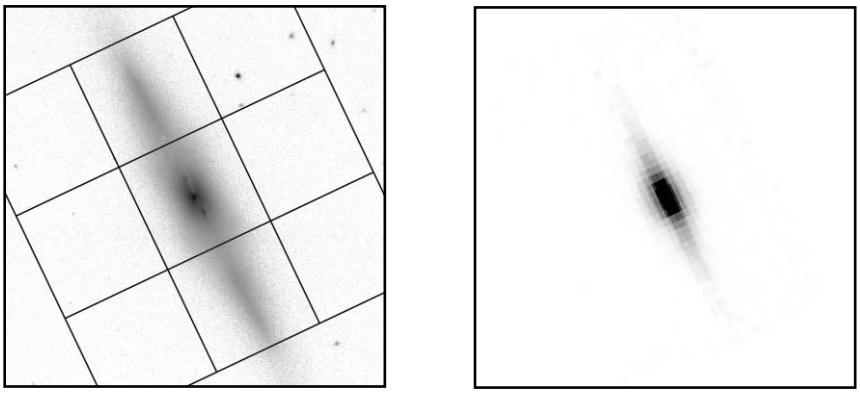

FIG. 31.—NGC 4710 [SA(r)0]

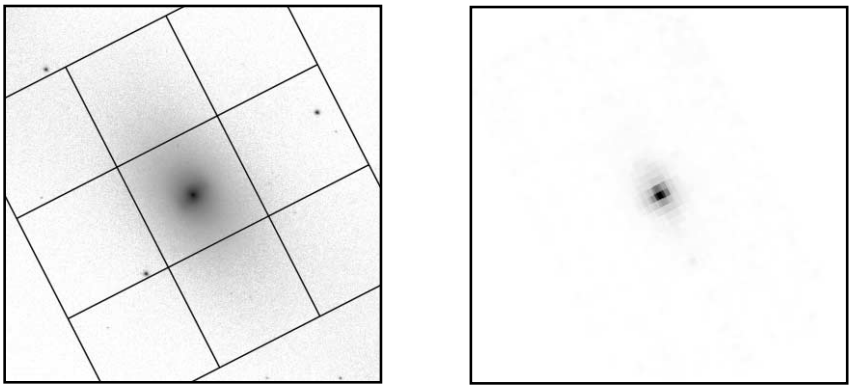

FIG. 32.—NGC 4725 [SAB(r)ab pec]

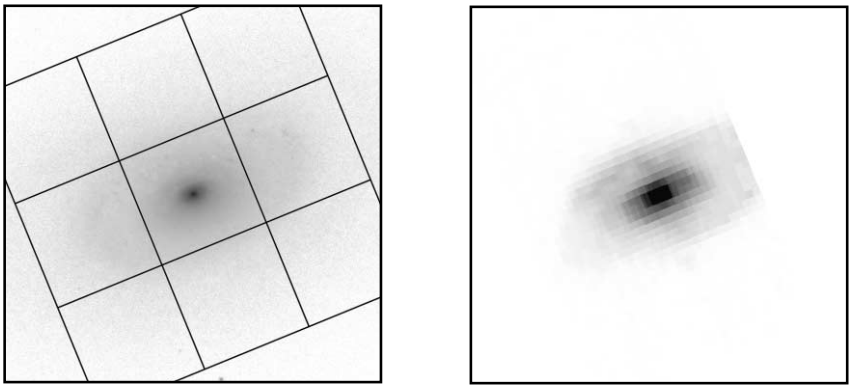

FIG. 33.—NGC 4826 [RSA(rs)ab]

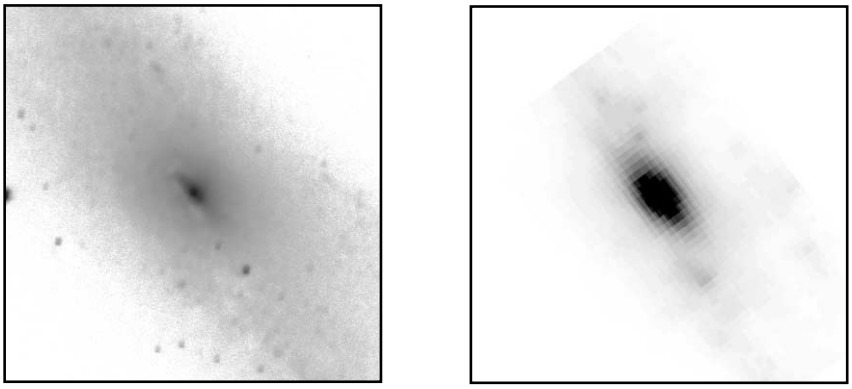

FIG. 34.—NGC 4945 [SB(s)cd]. This target was not successfully observed by ISOPHOT, so no overlay to represent the ISOPHOT C100 array has been placed in the *K*-band image.

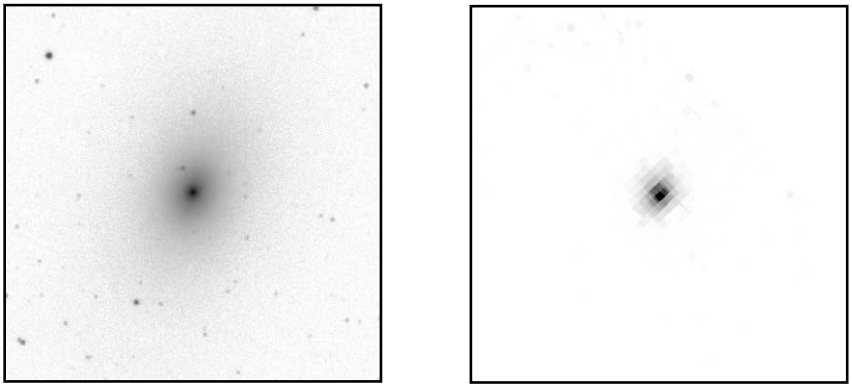

FIG. 35.—NGC 4976 (E4 pec). This target was not successfully observed by ISOPHOT, so no overlay to represent the ISOPHOT C100 array has been placed in the *K*-band image.

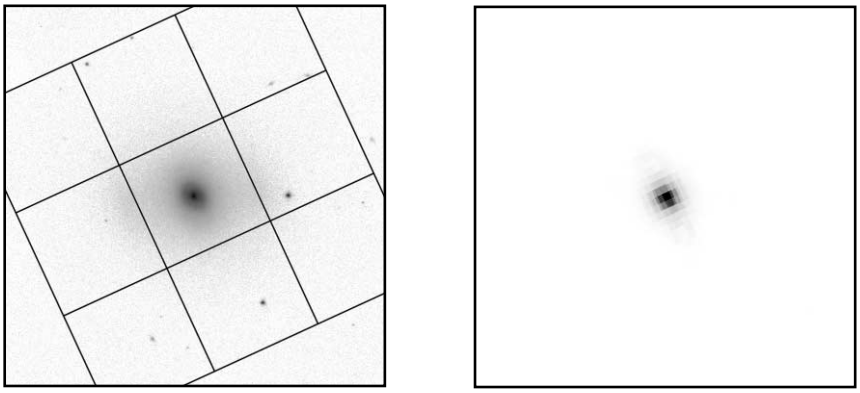

FIG. 36.—NGC 4984 [RSAB(rs)0]

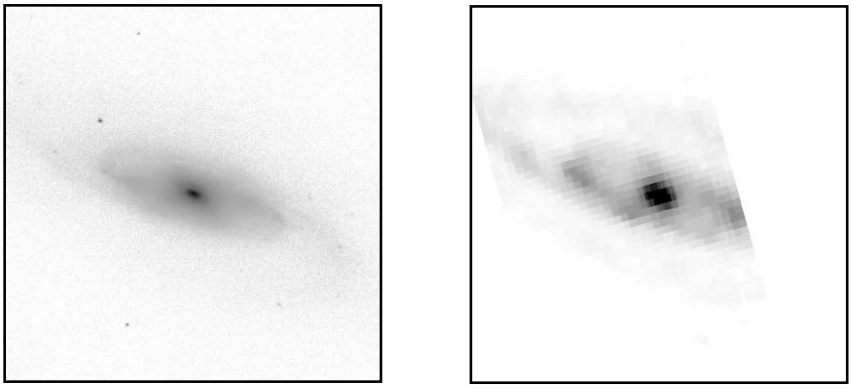

FIG. 37.—NGC 5005 [SAB(rs)bc]. This target was not successfully observed by ISOPHOT, so no overlay to represent the ISOPHOT C100 array has been placed in the *K*-band image.

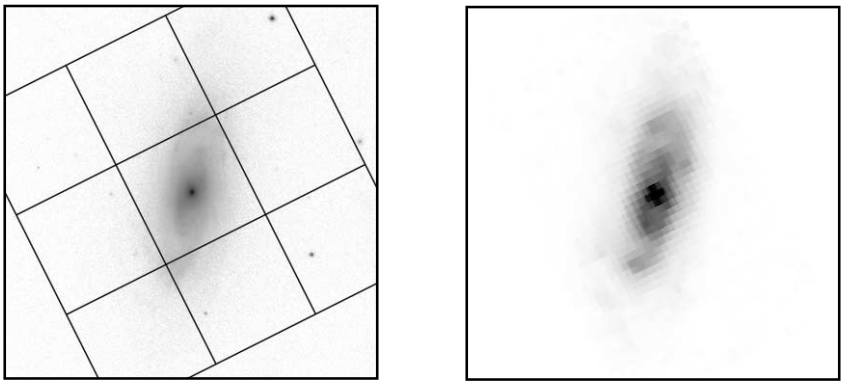

FIG. 38.—NGC 5033 [SA(s)c]

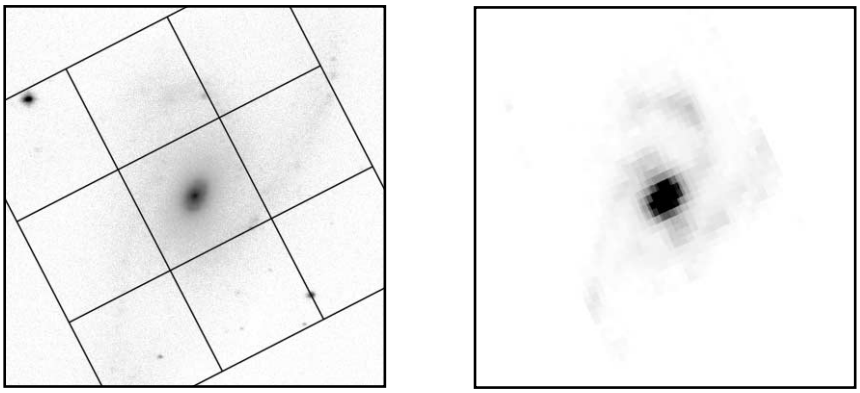

FIG. 39.—NGC 5054 [SA(s)bc]

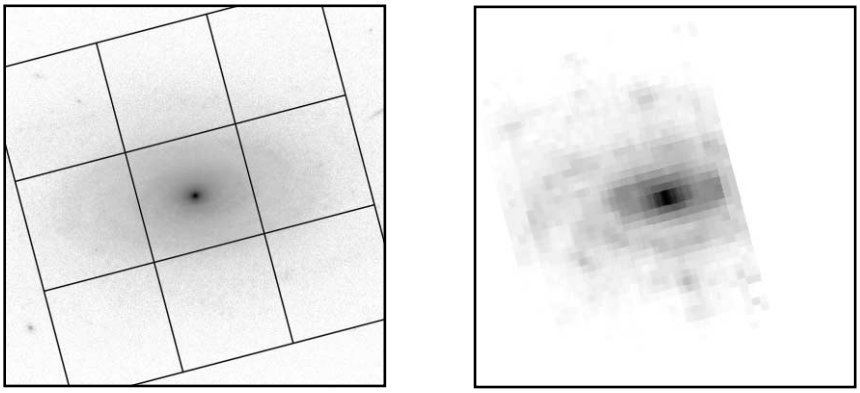

FIG. 40.—NGC 5055 [SA(rs)bc]

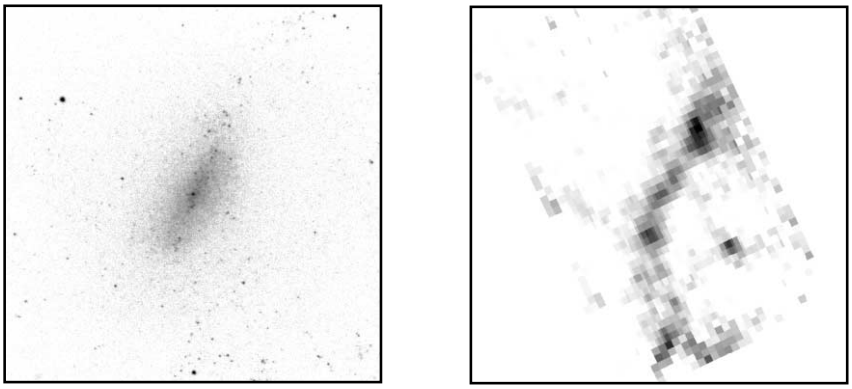

FIG. 41.—NGC 5068 [SAB(rs)cd]. This target was not successfully observed by ISOPHOT, so no overlay to represent the ISOPHOT C100 array has been placed in the *K*-band image.

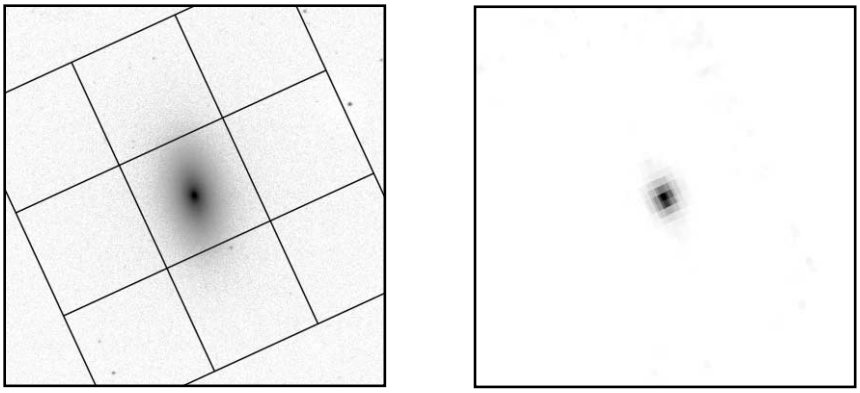

FIG. 42.—NGC 5087 (SA0)

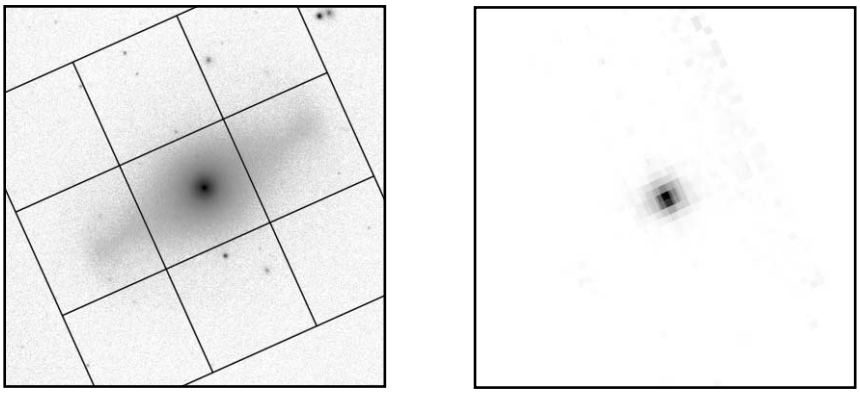

FIG. 43.—NGC 5101 [RSB(rs)0/a]

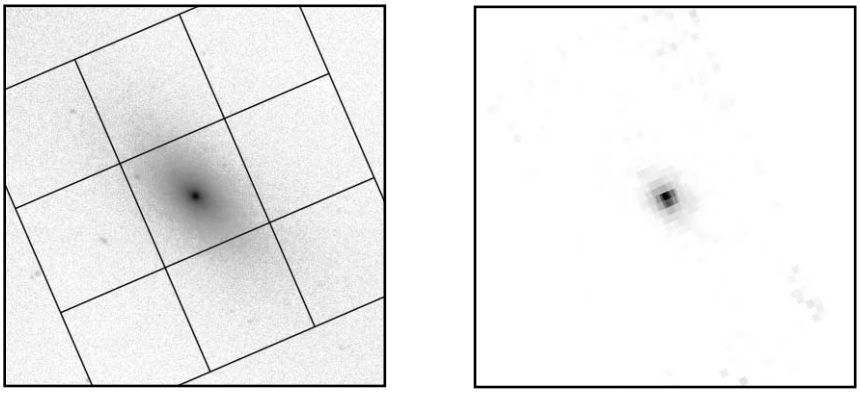

FIG. 44.—NGC 5102 (SA0)

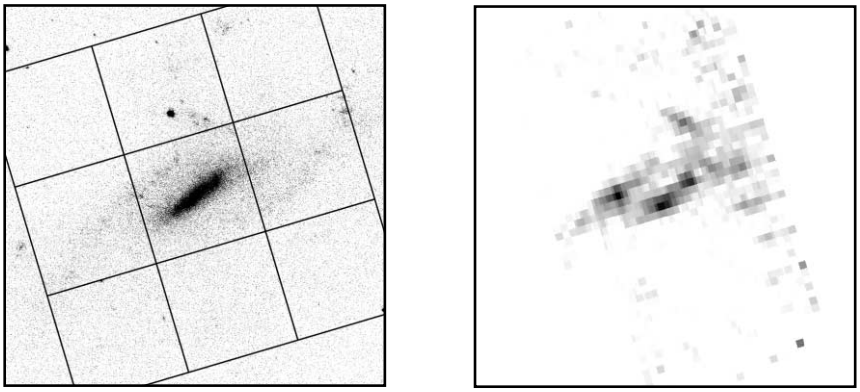

FIG. 45.—NGC 5112 [SB(rs)cd]

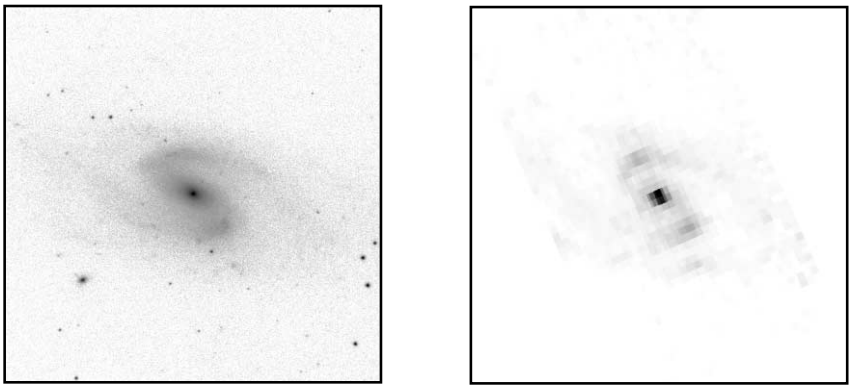

FIG. 46.—NGC 5161 [SA(s)c]. This target was not successfully observed by ISOPHOT, so no overlay to represent the ISOPHOT C100 array has been placed in the *K*-band image.

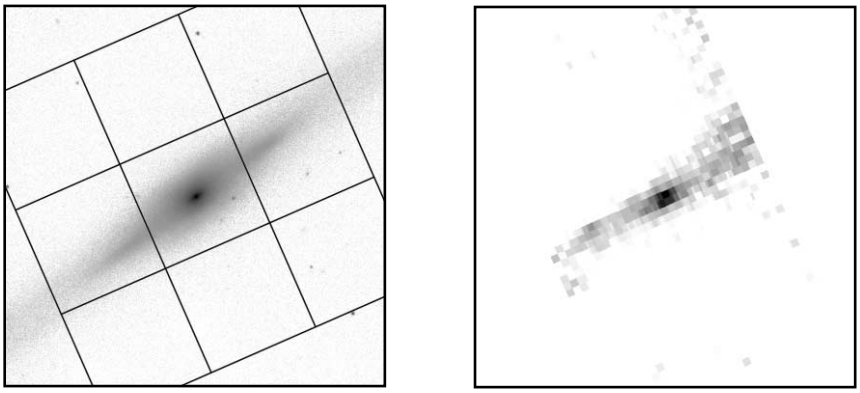

FIG. 47.—NGC 5170 [SA(s)c]

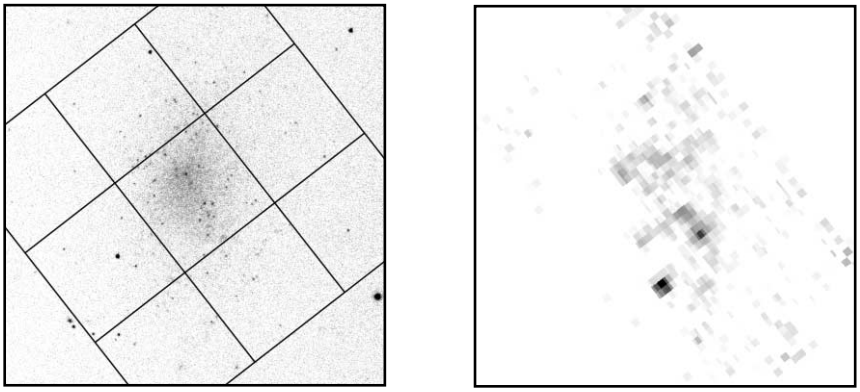

FIG. 48.—NGC 5204 [SA(s)m]

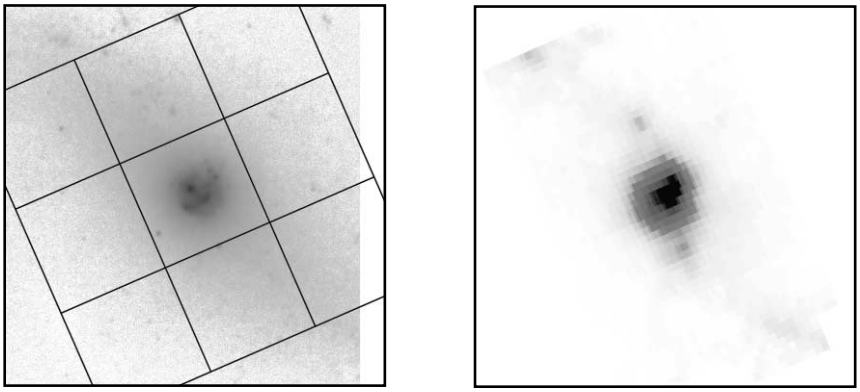

FIG. 49.—NGC 5236 [SAB(s)c]

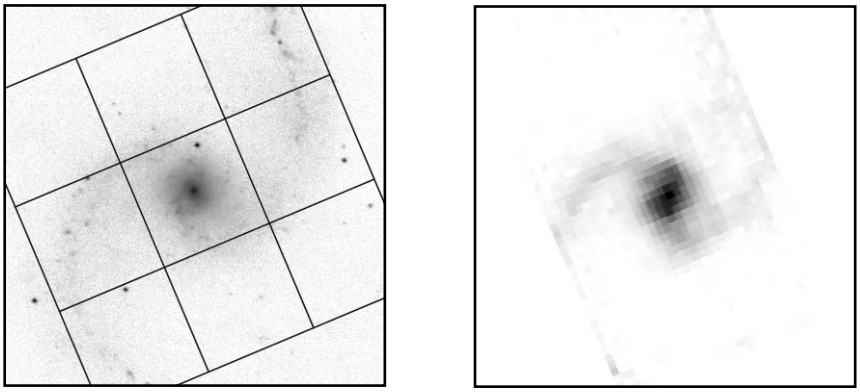

FIG. 50.—NGC 5247 [SA(s)bc]

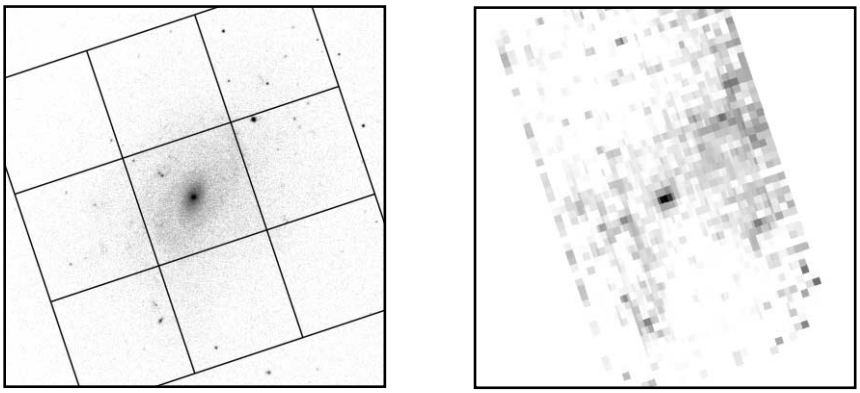

FIG. 51.—NGC 5300 [SAB(r)c]

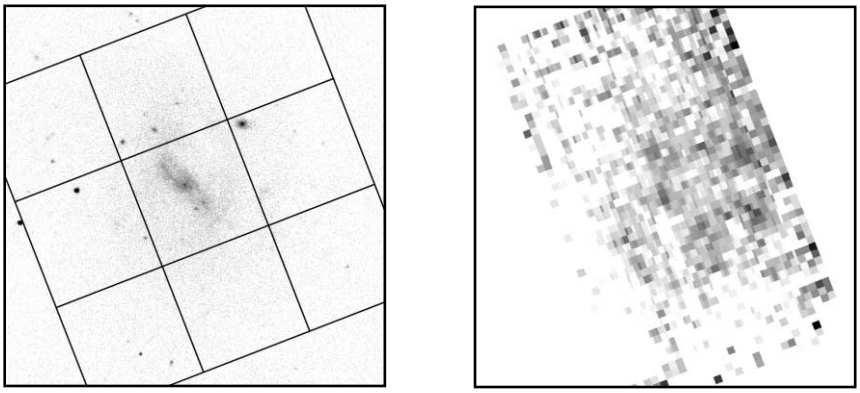

FIG. 52.—NGC 5334 [SB(rs)c]

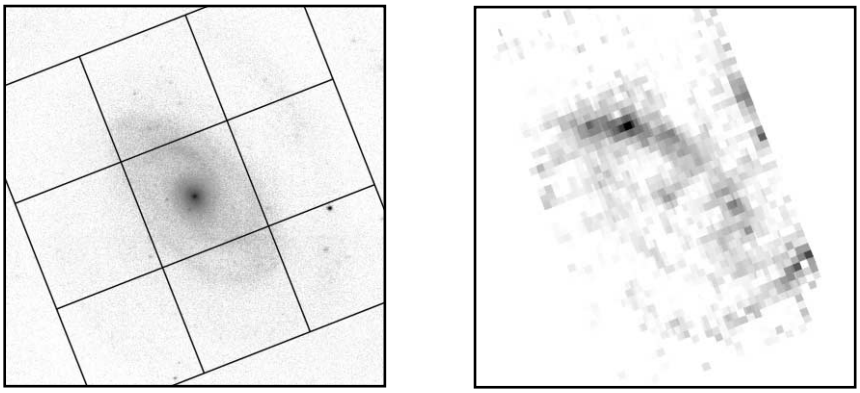

FIG. 53.—NGC 5364 [SA(rs)bc pec]

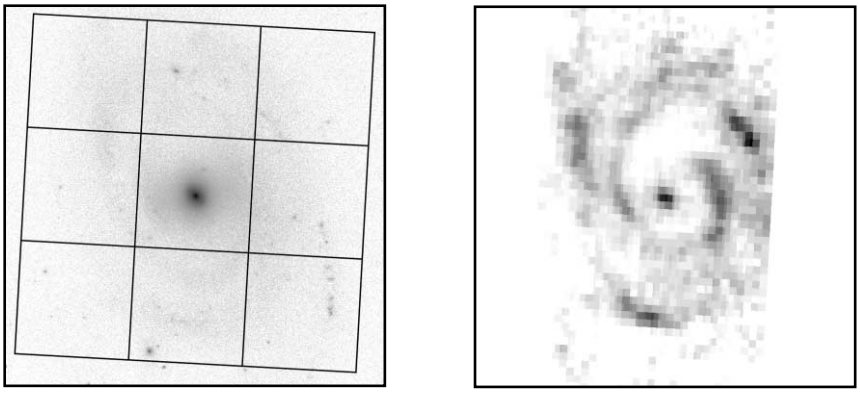

FIG. 54.—NGC 5371 [SAB(rs)bc]

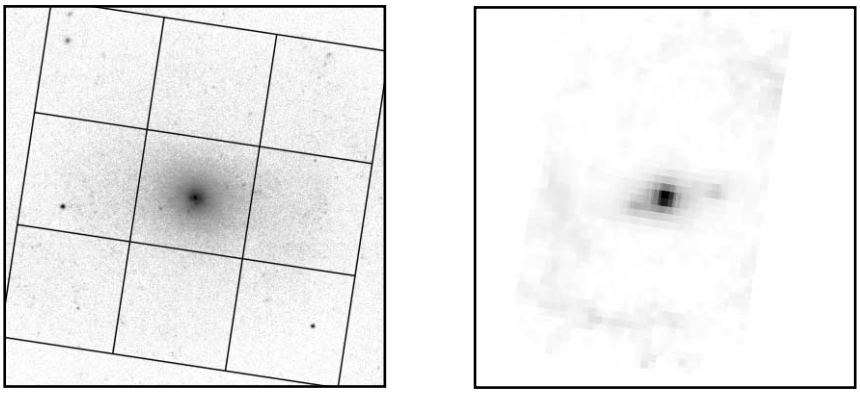

FIG. 55.—NGC 5457 [SAB(rs)cd]

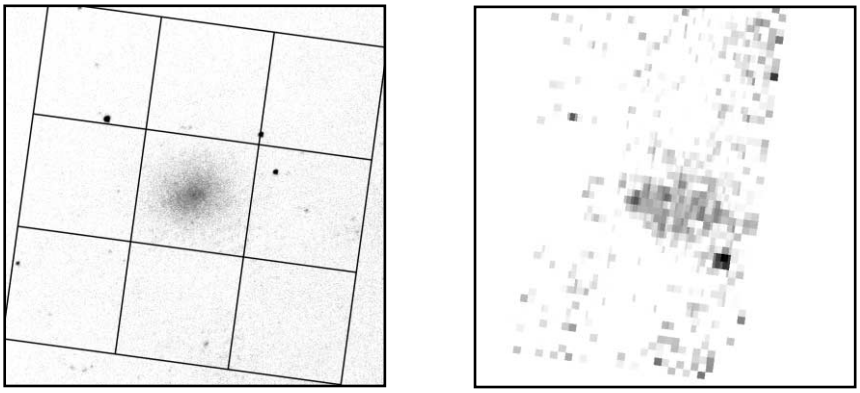

FIG. 56.—NGC 5474 [SA(s)cd]

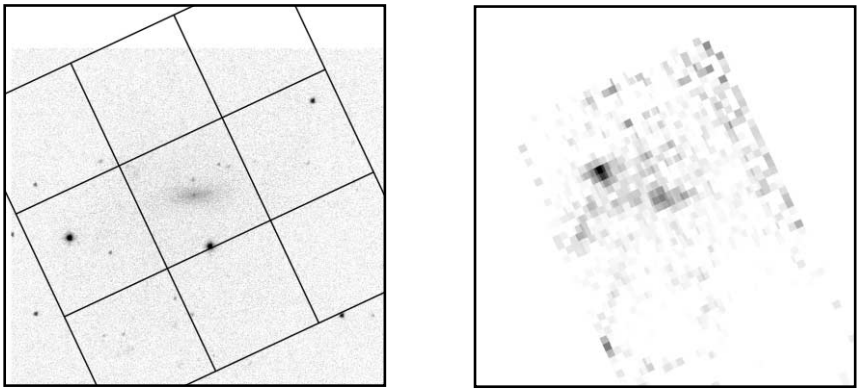

FIG. 57.—NGC 5556 [SAB(rs)d]

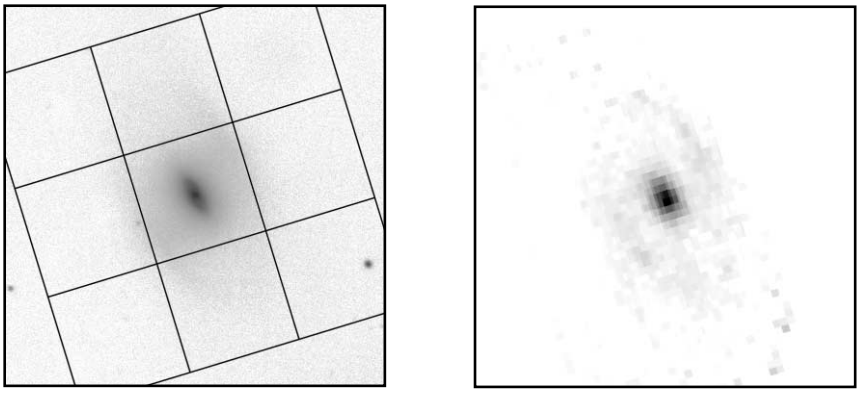

FIG. 58.—NGC 5566 [SB(r)ab]

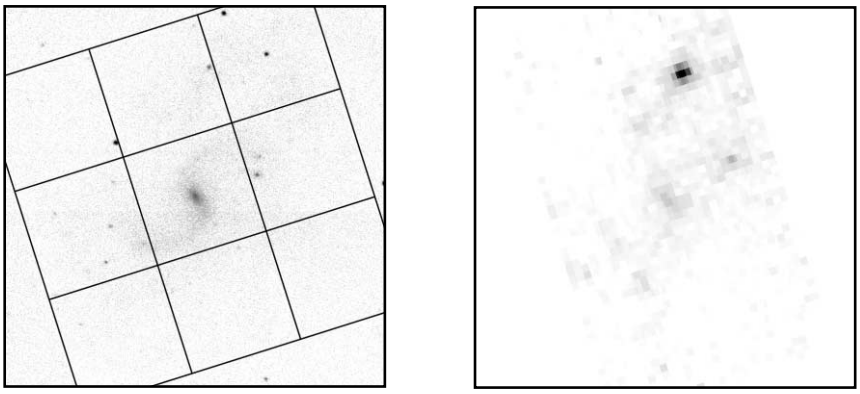

FIG. 59.—NGC 5584 [SAB(rs)cd]

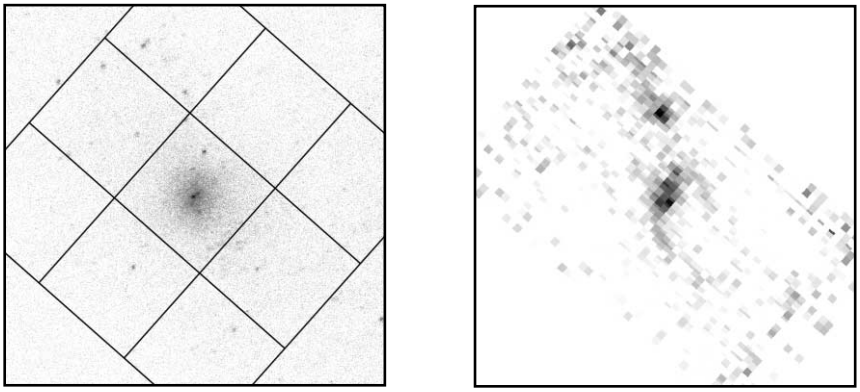

FIG. 60.—NGC 5585 [SAB(s)d]

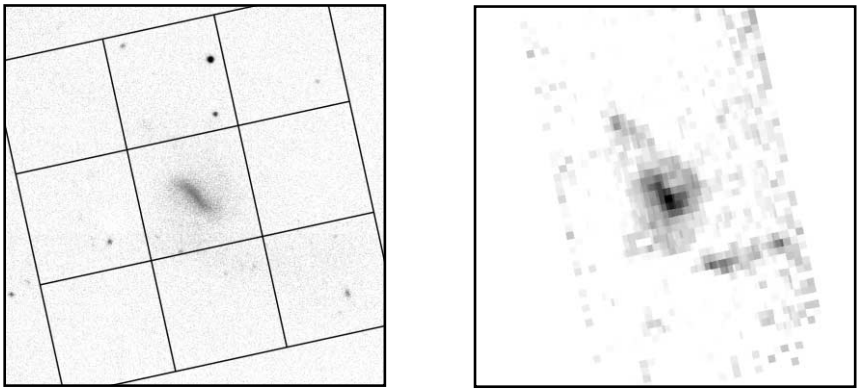

FIG. 61.—NGC 5669 [SAB(rs)cd]

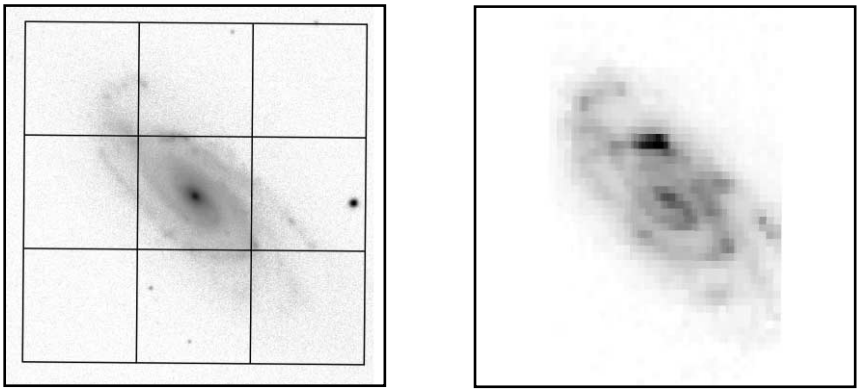

FIG. 62.—NGC 5676 [SA(rs)bc]

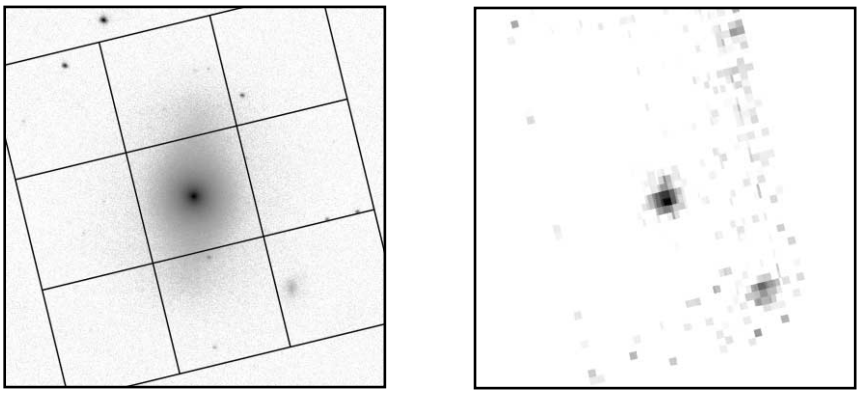

FIG. 63.—NGC 5701 [RSB(rs)0/a]

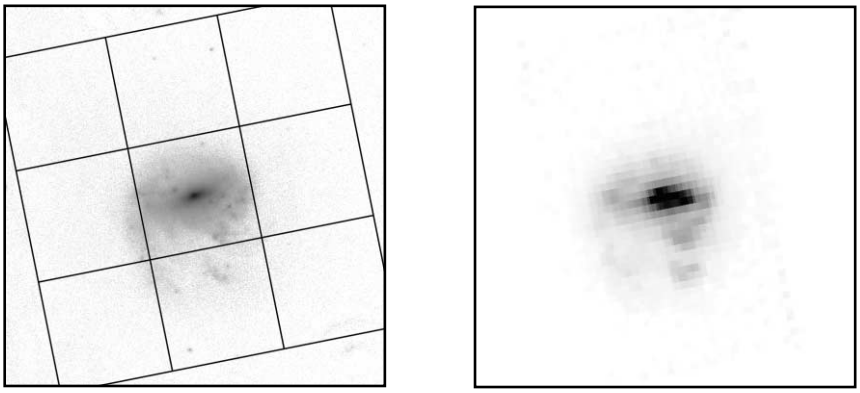

FIG. 64.—NGC 5713 [SAB(rs)bc pec]

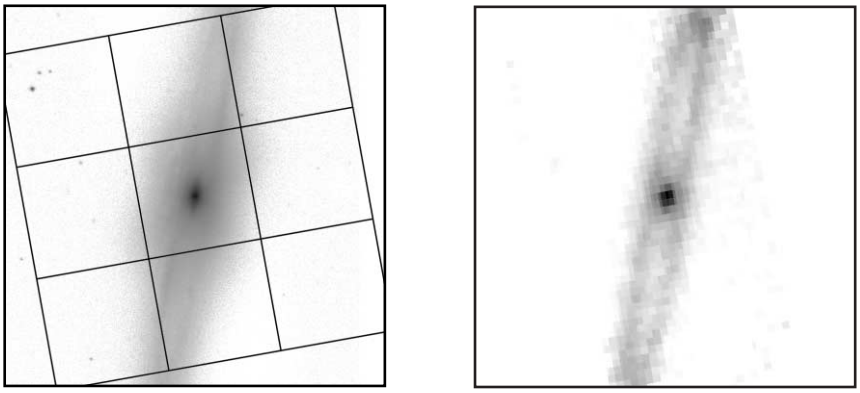

FIG. 65.—NGC 5746 [SAB(rs)b]

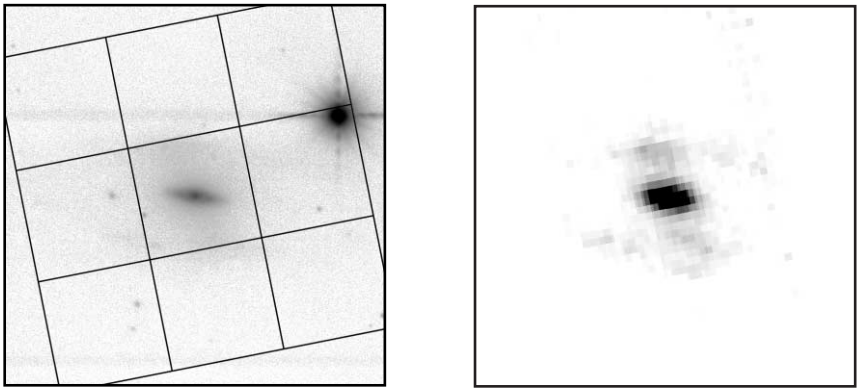

FIG. 66.—NGC 5792 [SB(rs)b]

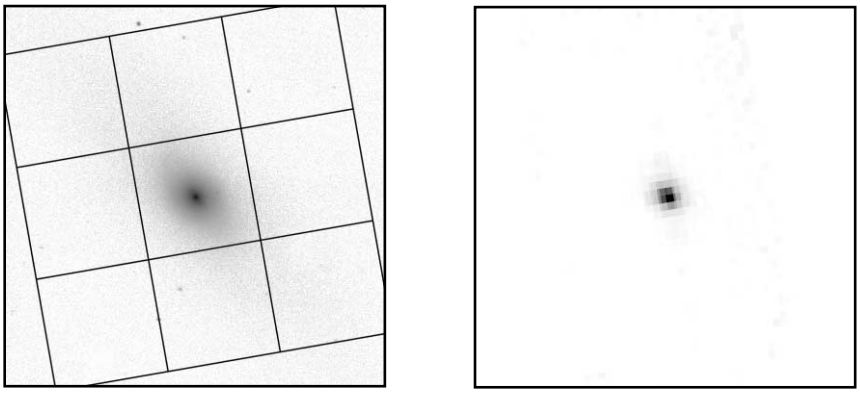

FIG. 67.—NGC 5838 (SA0)

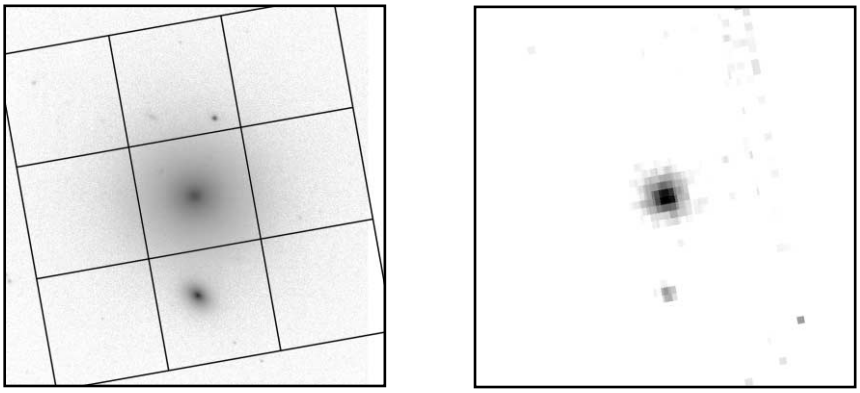

FIG. 68.—NGC 5846 (E0)

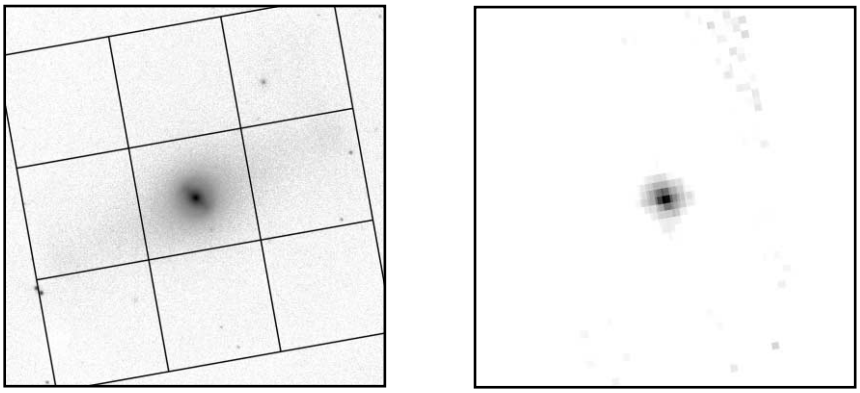

FIG. 69.—NGC 5850 [SB(r)b]

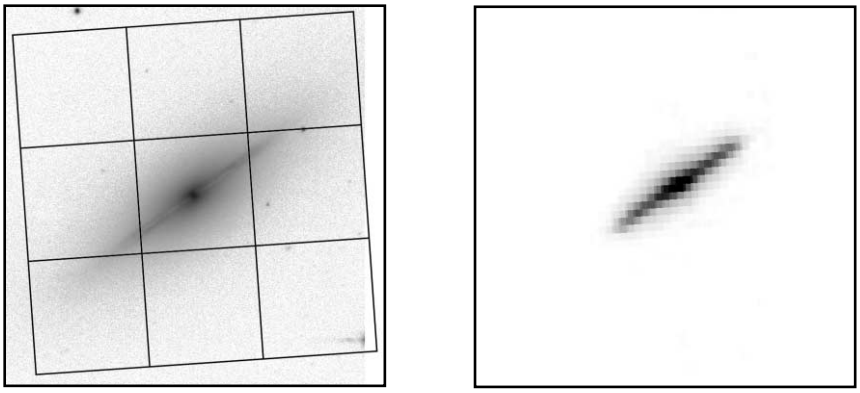

FIG. 70.—NGC 5866 (SA0)

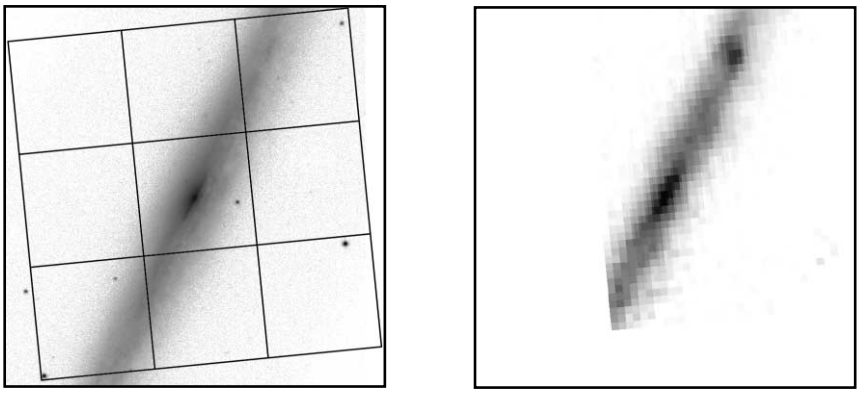

FIG. 71.—NGC 5907 [SA(s)c]

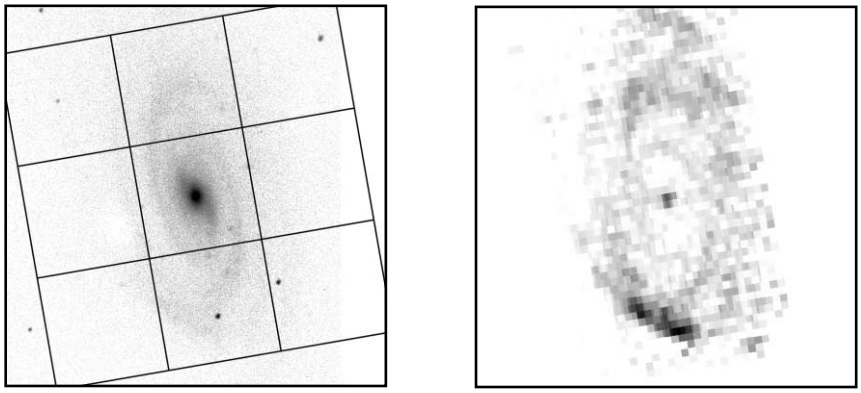

FIG. 72.—NGC 5985 [SAB(r)b]

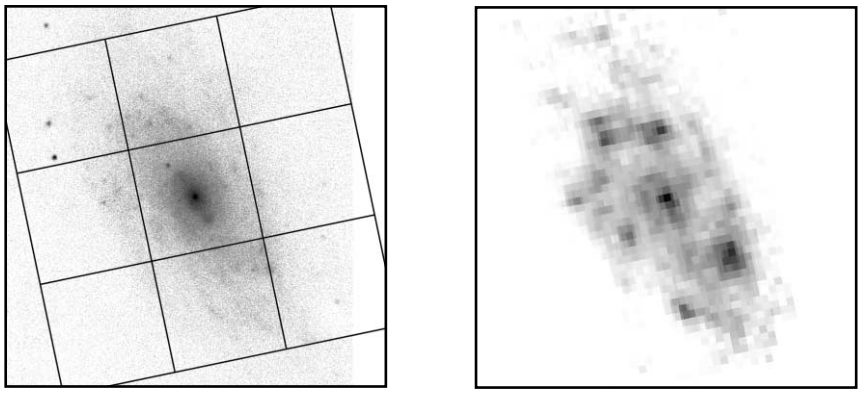

FIG. 73.—NGC 6015 [SA(s)cd]

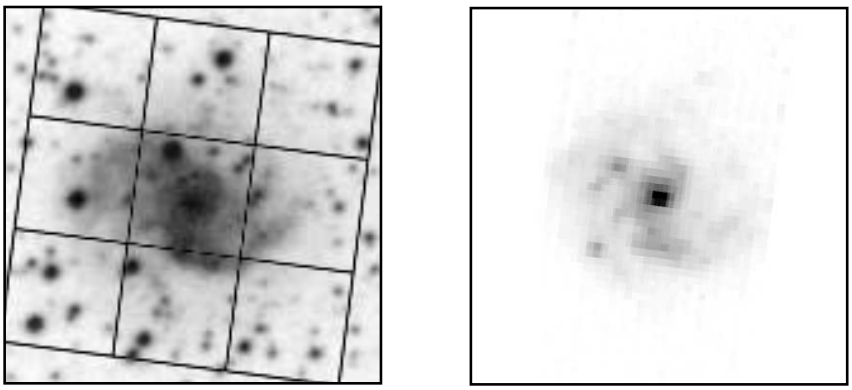

FIG. 74.—NGC 6215 [SA(s)c]. Since no *K*-band data are available, a second-generation red image from the STScI Digitized Sky Survey has been substituted.

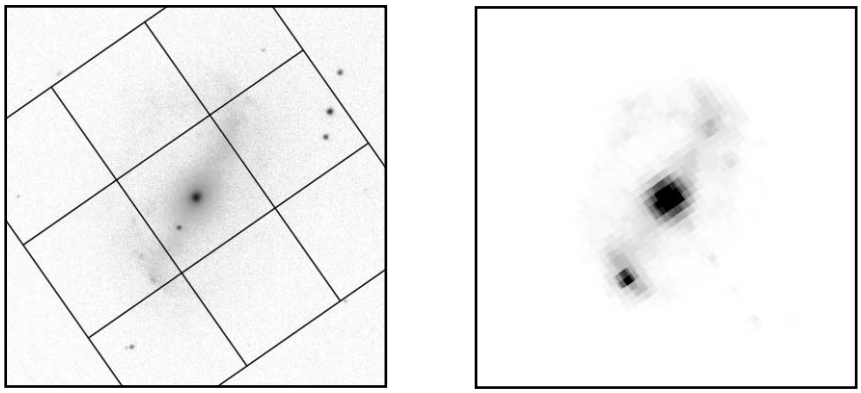

FIG. 75.—NGC 6217 [RSB(rs)bc]

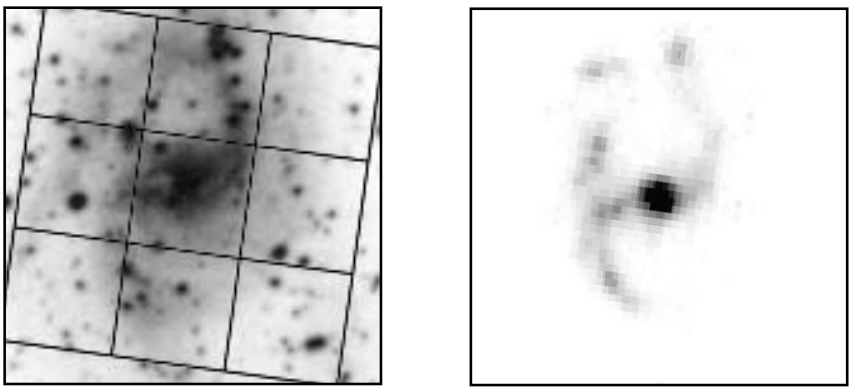

FIG. 76.—NGC 6221 [SB(s)c]. Since no *K*-band data are available, a second-generation red image from the STScI Digitized Sky Survey has been substituted.

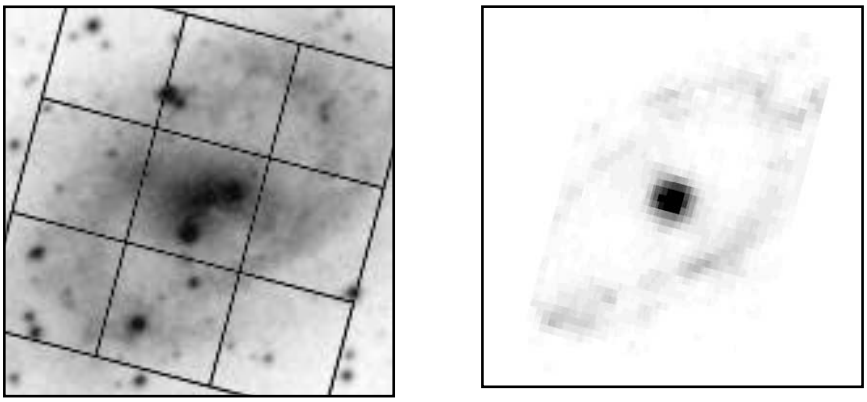

FIG. 77.—NGC 6300 [SB(rs)b]. Since no *K*-band data are available, a second-generation red image from the STScI Digitized Sky Survey has been substituted.

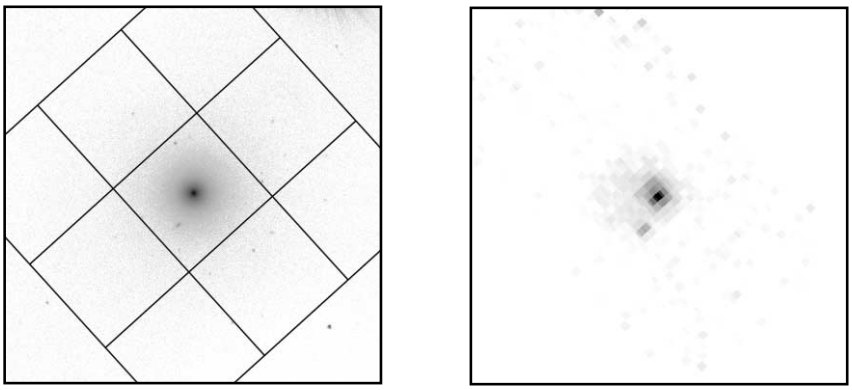

FIG. 78.—NGC 6340 [SA(s)0/a]

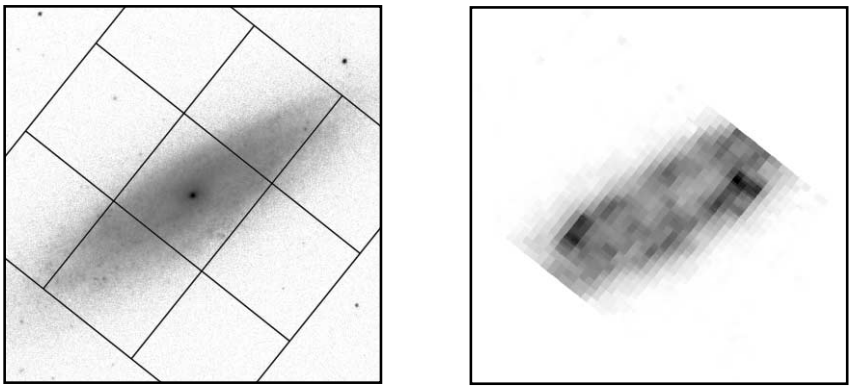

FIG. 79.—NGC 6503 [SA(s)cd]

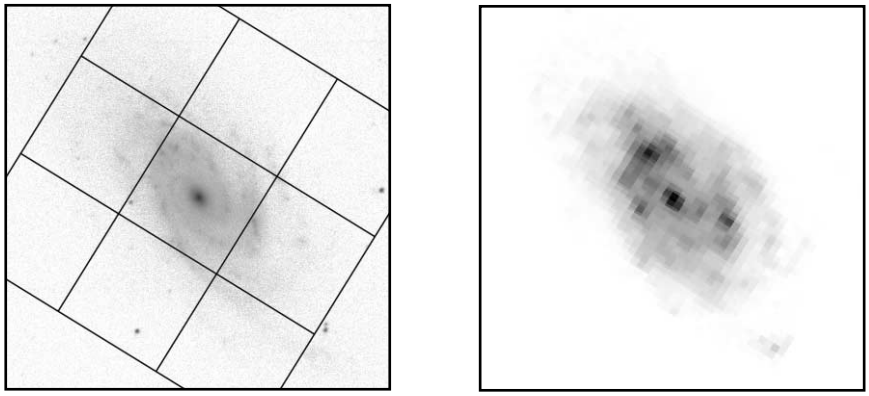

FIG. 80.—NGC 6643 [SA(rs)c]

ral galaxies may be related to the spatial distribution of the molecular gas. Young et al. (1995) found that, in contrast to early-type spiral galaxies, the isophotal diameters of molecular gas in late-type spiral galaxies were comparable to the galaxies' optical diameter. Furthermore, Young & Knezek (1989) found that the overall surface density of late-type spiral galaxies is higher than for early-type spiral galaxies. This means that the disks of late-type galaxies contain relatively more gas. Dust, which is associated with molecular gas, will therefore follow similar trends with morphology. Furthermore, because star formation is related to gas density (Kennicutt 1989), the increased density in molecular gas allows for star formation to occur more strongly in the disks of late-type spiral galaxies, which leads to enhanced mid-infrared emission.

Even though the disks of late-type spiral galaxies produce significant mid-infrared emission, the nuclei are still the strongest sources of mid-infrared emission in most of these galaxies. However, in a few cases, nuclear mid-infrared activity is suppressed relative to the disk's activity. NGC 4414, NGC 4605, NGC 5364, NGC 5371, NGC 5985, and NGC 6503 all have weak nuclear mid-infrared activity but strong mid-infrared activity in the disk. In these cases, several possible mechanisms could be inhibiting nuclear star formation activity. For example, there may be no dynamical mechanism, such as an interaction or a bar, for funneling gas and dust to the nucleus. Such an exigency would be plausible for galaxies that are known to be isolated SA galaxies such as NGC 6503 (Karachentsev & Sharina 1997). It is also possible that a previous burst of nuclear star formation activity could have either consumed or blown out the interstellar medium from the nucleus. This would be consistent with the holelike appearance of the 12 μm emission and the CO millimeter line emission in NGC 4414 (Sakamoto 1996).

Aside from cases in which nuclear activity is suppressed, some late-type spiral galaxies not only have nuclear mid-infrared sources but also display sources of emission outside their nuclei with 12 μm brightnesses equal to or brighter than those of their nuclei. The best examples of this are NGC 3556 and NGC 5676. In NGC 3556, a string of 12 μm sources lies along a line through the galaxy's center, but a knot to the north of the galaxy's center produces the brightest mid-infrared emission. In NGC 5676, a series of knots north of the galaxy's nucleus produces the brightest mid-infrared emission in the galaxy. These regions are clearly locations where star formation has been enhanced.

Strong bars in late-type spiral galaxies naturally affect the distribution of star formation structures. In several galaxies, the mid-infrared emission is enhanced at one or both ends of the bar, as in NGC 5792, NGC 6217, and NGC 6221. This is caused by the bar torquing material out to the ends of the bar, where the gas density is dramatically increased and star formation is enhanced. In other cases, however, the mid-infrared structures look like a string of knots along the bar, as in NGC 3359 and NGC 3556. None of the weakly barred galaxies have strong lobes at the ends of their bars, so it is possible that the bars in galaxies with lobes exert stronger forces on the interstellar medium than the bars without lobes. This would allow for the formation of a stellar bar structure without forcing gas either inward to the nucleus or outward to the ends of the bar.

Even though many of these galaxies have well-defined spiral structures, a few of these galaxies look amorphous and chaotic. NGC 4559, NGC 5112, NGC 5364, NGC 5474, and NGC 5713 all have particularly amorphous, antisymmetric appearances compared to other galaxies with similar Hubble types.

5.4. *Sd–Sm Galaxies*

For very late-type galaxies, the 12 μm structures become very diffuse and disorganized. The nucleus is still the strongest site of mid-infrared emission in some galaxies, as in NGC 1569 (which is actually an irregular galaxy), NGC 4395, NGC 4618, NGC 4631, and NGC 5585. However, even in these galaxies, nuclear mid-infrared emission is only a minor fraction of the total mid-infrared flux. The mid-infrared sources appear to be distributed randomly, although they tend to be clustered around the galaxies' nuclei. The 12 μm regions themselves look knotted instead of filamentary. NGC 4631, an edge-on spiral galaxy, is an exception. It has a very bright, relatively uniform 12 μm disk and a possible toroid structure. NGC 55, NGC 4236, and NGC 4395 are all much larger than 10′, so in the 12 μm maps we only see faint, diffuse structures near the centers of these galaxies.

Given that these galaxies have poorly organized dynamics and stellar structures, the irregularity in the appearance of mid-infrared emission is not surprising. A few of these objects, such as NGC 1569, NGC 4618, and NGC 4631, even appear to have been gravitationally disturbed. Apparently, gravitational interaction not only leads to distortion of stellar structures within galaxies but can also trigger simultaneous cloud collapse and star formation throughout the galaxies' disks.

6. SPATIAL DISTRIBUTION OF INFRARED FLUX

After a qualitative description of the spatial distribution of mid-infrared flux, we now examine quantitatively the ratio of nuclear to total infrared emission in the atlas galaxies. We compare the two flux ratios

$$R(12\ \mu\mathrm{m}) = \frac{f_{12}(15'')}{f_{12}(135'')} \tag{16}$$

and $R(60\ \mu\mathrm{m})$ (eq. [14]). Since these ratios are dependent on the angular sizes of the galaxies, we limit the analysis to galaxies with $1.5 < \log D_{25} < 1.9$.

Figures 81 and 82 show the distributions of $\log R(12\ \mu\mathrm{m})$ and $\log R(60\ \mu\mathrm{m})$ for the atlas galaxies that fall within this size range and that were detected at the respective wavelength within 135″. [Objects where the central source was detected but where the 135″ measurement was dominated by noise were excluded from the analysis of the $R(12\ \mu\mathrm{m})$ parameter.] Table 13 summarizes Gaussian statistics for these data as a function of Hubble type. A trend with Hubble type is clear for both the 12 and 60 μm emission. At both wavelengths the integrated disk emission dominates the total emission for all morphological types, and the disk emission becomes increasingly dominant going from earlier to later types. This trend is statistically more significant at 12 μm than at 60 μm, probably because the 15″ aperture at 12 μm is more effective at isolating nuclear emission. These data demonstrate that disk emission becomes increasingly dominant going from earlier to later Hubble types.

7. CONCLUSIONS

We have presented an atlas of infrared images and photometry for an optically selected, magnitude-limited sample of spiral galaxies. The infrared data span the spectral region from 1.25 to 180 μm.

A comparison of the *ISO* pointed observations with *IRAS* data showed that, for *ISO* apertures of 135″, the *ISO* and *IRAS* FSC measurements agree for 50%–60% of the galaxies. *IRAS* sometimes undersamples large galaxies at 60 μm, and there can be incomplete background subtraction for small galaxies at 100 μm, so that FSC flux densities and flux ratios can have systematic errors for nearby galaxies. However, for the majority of these galaxies the *ISO* and *IRAS* FSC data agree.

A review of the 12 μm morphological features revealed that in early-type galaxies the nuclei are almost always the strongest sites of mid-infrared emission. The disks of early-type spirals generally did not contain any major 12 μm structures, with the exception of uniform rings formed at either the inner Lindblad resonance or the ends of the primary bars in some of the barred galaxies. Late-type spirals, however, almost always contain extended mid-infrared emission in addition to strong emission from the nuclei. Structures in the form of either knots or arm fragments follow the spiral arms. In a few exceptional late-type spirals nuclear activity appeared to be suppressed, and the disk contained the strongest 12 μm sources in the galaxy.

Quantitatively, the disk emission dominates nuclear emission in the atlas galaxies at 12 μm and contributes a

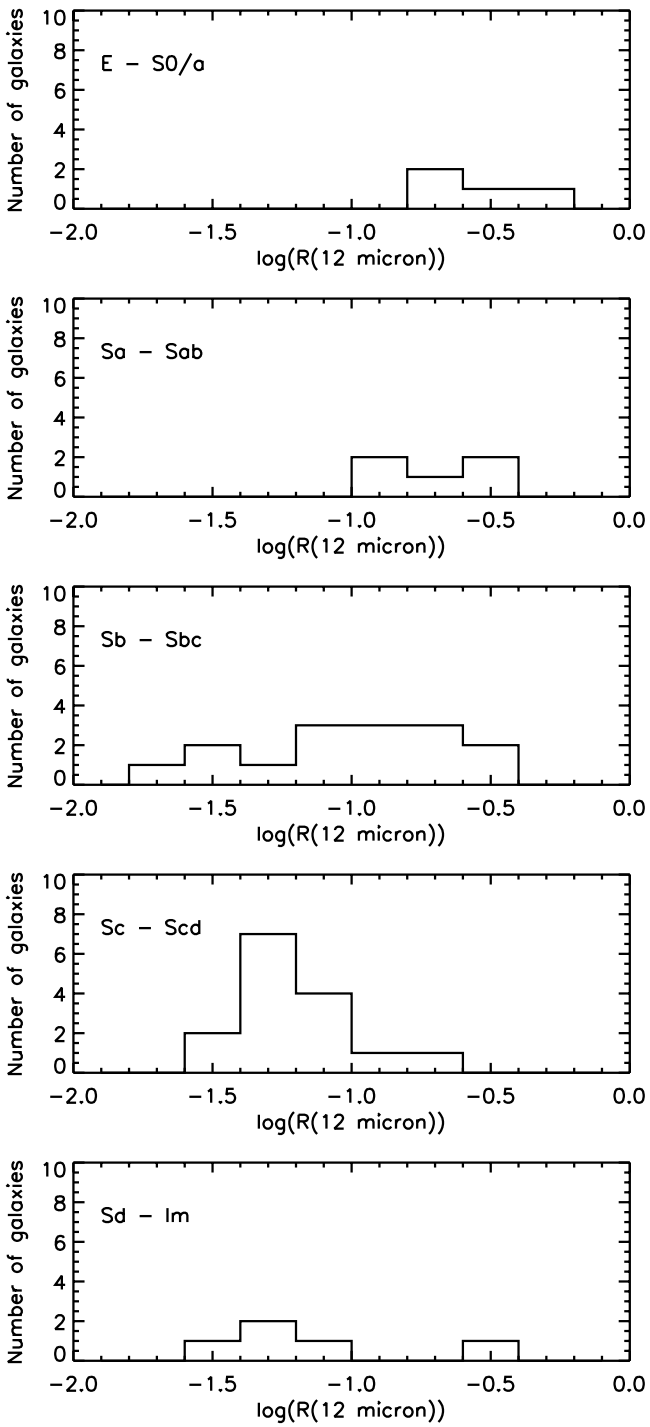

FIG. 81.—Plot of the mid-infrared spatial extent indicator $\log R(12\ \mu\mathrm{m})$ for various subgroups of galaxies where $1.5 < \log D_{25} < 1.9$. A large R indicates more centrally concentrated mid-infrared emission, and a small value indicates more extended mid-infrared emission. Note that the general trend shows that the regions producing mid-infrared emission in late-type galaxies are more extended than in early-type galaxies.

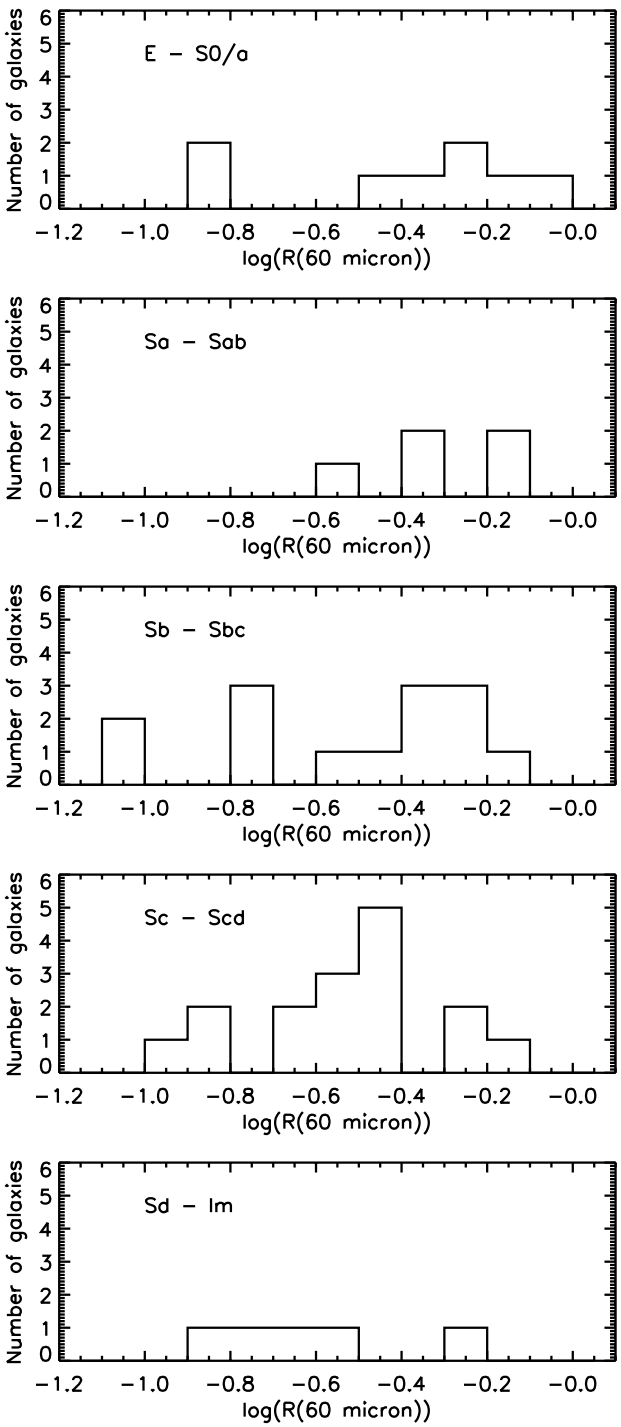

FIG. 82.—Plot of the mid-infrared spatial extent indicator $\log R(60\ \mu\mathrm{m})$ for various subgroups of galaxies where $1.5 < \log D_{25} < 1.9$. A large R indicates more centrally concentrated far-infrared emission, and a small value indicates more extended far-infrared emission. Note that the general trend shows that the regions producing far-infrared emission in late-type galaxies are more extended than in early-type galaxies, although the trend is not as clear as it is at 12 μm.

TABLE 13
SPATIAL EXTENT INDICATORS FOR DIFFERENT HUBBLE TYPES

	$R(12\ \mu\mathrm{m})$		$R(60\ \mu\mathrm{m})$	
TYPE	Number of Galaxies	Mean Value	Number of Galaxies	Mean Value
E–S0/a	4	0.34 ± 0.06	8	0.49 ± 0.10
Sa–Sab.....	5	0.22 ± 0.04	5	0.54 ± 0.09
Sb–Sbc.....	15	0.13 ± 0.02	14	0.37 ± 0.06
Sc–Scd	15	0.071 ± 0.012	16	0.32 ± 0.04
Sd–Im	5	0.10 ± 0.04	5	0.29 ± 0.07
All.....	44	0.137 ± 0.017	48	0.38 ± 0.03

significant amount of flux at 60 μm. Furthermore, the disk emission becomes increasingly dominant going from earlier to later Hubble types.

There are many people without whom *ISO* would not have happened. However, as one of the contributors to the initial *ISO* proposal, R. D. J. wishes to acknowledge the exceptional vision of Reinder van Duinen, who conceived the project, and Roger Emery and Claude Burgio, who executed the superb Phase A study that provided a compelling scientific and technical case for *ISO*. G. J. B. would like to thank Stephan Ott and the other staff members who produced the ISOCAM Data Reduction Workshop in 1998. G. J. B. would also like to thank Herve Aussel for help with CIR. The ISOPHOT data presented in this paper were reduced using PIA, which is a joint development by the ESA Astrophysics Division and the ISOPHOT Consortium with the collaboration of the Infrared Processing and Analysis Center (IPAC). Contributing ISOPHOT Consortium institutes are DIAS, RAL, AIP, MPIK, and MPIA. The ISOCAM data presented in this paper were analyzed using CIA, a joint development by the ESA Astrophysics Division and the ISOCAM Consortium. The ISOCAM Consortium is led by the ISOCAM PI, C. Cesarsky. This research has made use of the NASA/IPAC Extragalactic Database (NED), which is operated by the Jet Propulsion Laboratory, California Institute of Technology, under contract with the National Aeronautics and Space Administration. The Digitized Sky Surveys were produced at the Space Telescope Science Institute under US Government grant NAG W-2166. The images of these surveys are based on photographic data obtained using the Oschin Schmidt Telescope on Palomar Mountain and the UK Schmidt Telescope. The plates were processed into the present compressed digital form with the permission of these institutions. This research has been supported by NASA grants NAG 5-3370 and JPL 961566.

REFERENCES

Arp, H. 1966, Atlas of Peculiar Galaxies (Pasadena: Caltech)
———. 1981, ApJS, 46, 75
Benedict, G. F., et al. 1993, AJ, 105, 1369
Binggeli, B., Sandage, A., & Tammann, G. A. 1985, AJ, 90, 1681
Blommaert, J., Siebenmorgen, R., Coulais, A., Okumura, K., Ott, S., Sauvage, M., & Starck, J.-L. 2001, The *ISO* Handbook Volume 3: PHT—The *ISO* Camera, Version 1.2
Braun, R., Walterbos, R. A. M., & Kennicutt, R. C. 1992, Nature, 360, 442
Cesarsky, C. J., et al. 1996, A&A, 315, L32
Cesarsky, D., & Blommaert, J. 2000, ISOCAM Calibration Accuracies Document
Coulais, A., & Abergel, A. 2000, A&AS, 141, 533
Dale, D. A., et al. 2000, AJ, 120, 583
Davies, R. D., Davidson, G. P., & Johnson, S. C. 1980, MNRAS, 191, 253

de Jong, T., Clegg, P. E., Soifer, B. T., Rowan-Robinson, M., Habing, H. J., Houck, J. R., Aumann, H. H., & Raimond, E. 1984, ApJ, 278, L67
de Vaucouleurs, G., de Vaucouleurs, A., Corwin, H. G., Buta, R. J., Paturel, G., & Fouque, P. 1991, Third Reference Catalogue of Bright Galaxies (Berlin: Springer)
Elmegreen, D. M., & Elmegreen, B. G. 1987, ApJ, 314, 3
Friedli, D., Wozniak, H., Rieke, M., Martinet, L., & Bratschi, P. 1996, A&AS, 118, 461
Fullmer, L., & Lonsdale, C. 1989, Cataloged Galaxies and Quasars Observed in the *IRAS* Survey, Version 2 (Pasadena: Jet Propulsion Laboratory)
Gabriel, C., Acosta-Pulido, J., Heinrichsen, I., Morris, H., & Tai, W.-M. 1997, in ASP Conf. Ser. 125, Astronomical Data Analysis Software and Systems (ADASS) VI, ed. G. Hunt & H. E. Payne (San Francisco: ASP), 108
Hawarden, T. G., Leggett, S. K., Letawsky, M. B., Ballantyne, D. R., & Casali, M. M. 2001, MNRAS, 325, 563
Hawarden, T. G., van Woerden, H., Mebold, U., Goss, W. M., & Peterson, B. A. 1979, A&A, 76, 230
Haynes, M. P. 1979, AJ, 84, 1830
Helou, G. H., Salpeter, E. E., & Terzian, Y. 1982, AJ, 87, 1443
Helou, G., & Walker, D. W. 1988, Infrared Astronomical Satellite (*IRAS*) Catalogs and Atlases, Volume 7 (Washington: NASA)
Ho, L. C., Filippenko, A. V., & Sargent, W. L. W. 1997, ApJS, 112, 315
Joseph, R. D., Meikle, W. P. S., Robertson, N. A., & Wright, G. S. 1984, MNRAS, 209, 111
Karachentsev, I. D., & Sharina, M. E. 1997, A&A, 324, 457
Kennicutt, R. C. 1989, ApJ, 344, 685
Kessler, M. F., et al. 1996, A&A, 315, L27
Klaas, U., Laureijs, R. J., Radovich, M., Schulz, B., & Wilke, K. 2000, ISOPHOT Calibration Accuracies
Kuijken, K., & Merrifield, M. R. 1995, ApJ, 443, L13
Laureijs, R. J. 1999, Point Spread Function Fractions Related to the ISOPHOT C100 and C200 Arrays, Version 1.0
Laureijs, R. J., Klaas, U., Richards, P. J., Schulz, B., & Ábrahám, P. 2000, The *ISO* Handbook Volume 5: PHT—The Imaging Photo-Polarimeter, Version 1.1
Lemke, D., et al. 1996, A&A, 315, L64
Moshir, M., et al. 1990, *IRAS* Catalogs, The Faint Source Catalog, Version 2.0 (Pasadena: Jet Propulsion Laboratory)
Ott, S., et al. 1997, in ASP Conf. Ser. 125, Astronomical Data Analysis Software and Systems (ADASS) VI, ed. G. Hunt & H. E. Payne (San Francisco: ASP), 34
Pence, W. D., & Blackman, C. P. 1984, MNRAS, 207, 9
Prieto, M., Gottesman, S. T., Aguerri, J.-A. L., & Varela, A.-M. 1997, AJ, 114, 1413
Radovich, M., Klaas, U., Acosta-Pulido, J., & Lemke, D. 1999, A&A, 348, 705
Rice, W., Lonsdale, C. J., Soifer, B. T., Neugebauer, G., Kopan, E. L., Lloyd, L. A., de Jong, T., & Habing, H. J. 1988, ApJS, 68, 91
Rieke, G. H., & Lebofsky, M. J. 1978, ApJ, 220, L37
Roussel, H., et al. 2001, A&A, 369, 473
Sakamoto, K. 1996, ApJ, 471, 173
Sandage, A., & Bedke, J. 1994, Canegie Atlas of Galaxies (Washington: Carnegie Institution)
Sandage, A., & Tammann, G. A. 1987, A Revised Shapley-Ames Catalog of Bright Galaxies (2d ed.; Washington: Carnegie Institution)
Scoville, N. Z., Becklin, E. E., Young, J. S., & Capps, R. W. 1983, ApJ, 271, 512
Soifer, B. T., Boehmer, L., Neugebauer, G., & Sanders, D. B. 1989, AJ, 98, 766
Starck, J. L., et al. 1999, A&AS, 134, 135
Tuffs, R. J., Popescu, C. C., Pierini, D., Voelk, H. J., Hippelein, H., Metcalfe, L., Heinrichsen, I., & Xu, C. 2002, ApJS, 139, 37
Tully, R. B. 1988, Nearby Galaxies Catalog (Cambridge: Cambridge Univ. Press)
van Driel, W., & Buta, R. 1993, PASJ, 45, L47
van Moorsel, G. A. 1983a, A&AS, 53, 271
———. 1983b, A&AS, 54, 19
Young, J. S., et al. 1995, ApJS, 98, 219
Young, J. S., & Knezek, P. M. 1989, ApJ, 347, L55